

FLORIDA STATE UNIVERSITY
COLLEGE OF ARTS AND SCIENCES

MEASUREMENT OF J/ψ PRODUCTION NEAR THRESHOLD IN $J/\psi \rightarrow \mu^+\mu^-$

By

DONAVAN EBERSOLE

A Dissertation submitted to the
Department of Physics
in partial fulfillment of the
requirements for the degree of
Doctor of Philosophy

2024

Copyright © 2024 Donovan Ebersole. All Rights Reserved.

Donavan Ebersole defended this dissertation on November 5, 2024.

The members of the supervisory committee were:

Sean Dobbs
Professor Directing Dissertation

Martin Bauer
University Representative

Volker Crede
Committee Member

Todd Adams
Committee Member

Kevin Fosse
Committee Member

The Graduate School has verified and approved the above-named committee members, and certifies that the dissertation has been approved in accordance with university requirements.

To my incredible wife, Madelynn, whose love has been my guiding light and who has inspired me to reach for the stars.

ACKNOWLEDGMENTS

First and foremost, I would like to express my sincere gratitude to my advisor, Sean Dobbs, for his invaluable guidance, support, and mentorship throughout this journey. His expertise and encouragement have been instrumental in my academic growth.

I would also like to express my sincere gratitude to the GlueX Collaboration for their support and contributions to this research. The collaborative environment and shared expertise have been invaluable. I am particularly grateful to Lubomir Pentchev and Alex Austregesilo for their guidance.

I am also deeply indebted to my committee members, Volker Crede, Todd Adams, Kevin Fosse, and Martin Bauer, for their insightful feedback, constructive criticism, and unwavering support. Their contributions have significantly enhanced the quality of my research.

I would like to extend my heartfelt thanks to the Physics Department faculty and staff for their assistance and dedication. Their support and resources have been essential to my success.

A special thanks to my colleagues and fellow graduate students, who have provided camaraderie, encouragement, and valuable discussions. Their friendship and support have made this experience truly memorable.

Finally, I would like to express my eternal gratitude to my family and friends. Their unwavering love, support, and belief in me have been the driving force behind my accomplishments.

TABLE OF CONTENTS

List of Tables	viii
List of Figures	ix
Abstract	xiii
1 Introduction	1
1.1 The Standard Model of Particle Physics	1
1.2 Quantum Chromodynamics	1
1.3 The Constituent Quark Model	4
1.4 The Proton and Its Structure	6
1.5 Models of J/ψ Photoproduction	12
1.5.1 Gluonic Exchange	13
1.5.2 Open-Charm Exchange	17
1.5.3 Pentaquarks	20
1.5.4 J/ψ and The GlueX Experiment	22
2 Previous Measurements	25
2.1 SLAC	25
2.2 Cornell	27
2.3 GlueX Collaboration	28
2.3.1 Initial $J/\psi \rightarrow e^+e^-$ Publication	28
2.3.2 Updated GlueX Results	30
2.4 J/ψ -007 Experiment	31
3 The GlueX Experiment	36
3.1 The Photon Beam	36
3.1.1 Producing a Tagged Photon Beam	37
3.1.2 Beam Polarization and Flux	39
3.2 GlueX Spectrometer	42
3.2.1 Target	43
3.2.2 Solenoid Magnet	43
3.2.3 Charged Particle Reconstruction	43

3.2.4	Neutral Particle Reconstruction	46
3.2.5	Particle Identification	48
3.2.6	The DIRC Detector	50
3.2.7	Trigger and Data Acquisition	51
4	Data Analysis	53
4.1	Overview	53
4.1.1	Datasets	54
4.1.2	Simulation	55
4.2	Event Kinematics and Calorimeter Motivation	56
4.2.1	Kinematic Distributions of J/ψ Photoproduction Events	56
4.2.2	Calorimeter Energy Distributions	57
4.3	Event Selections	58
4.3.1	Accidental Subtraction	59
4.3.2	Kinematic Fitting	59
4.3.3	Muon/Pion Separation: FCAL Energy Deposition	61
4.3.4	Muon/Pion Separation: BCAL Energy Deposition	63
4.3.5	Muon/Pion Separation: Baryon Rejection	64
4.4	Modeling of Calorimeter Energy Deposition	65
4.4.1	FCAL Energy Deposition	66
4.4.2	BCAL Energy Deposition	74
4.5	Summary of Event Selections	79
4.6	The Mass Spectra and Cross Section of $J/\psi \rightarrow \mu^+\mu^-$	81
4.6.1	High Mandelstam- t events	84
4.7	Estimating Systematic Uncertainties	84
4.7.1	Event Selections	84
4.7.2	Yield Systematics	90
4.7.3	Other Systematic Uncertainties	90
4.8	Final Results	92
5	Summary and Conclusion	95

Appendix

A Mass Distributions	97
References	98
Biographical Sketch	103

LIST OF TABLES

4.1	Summary of datasets used for this analysis	54
4.2	Summary of simulation samples used for this analysis.	54
4.3	Summary of loose timing cuts.	55
4.4	A list of the event selections we used, their relative efficiencies, and the cumulative signal to background ratio when that selection and above is applied.	79
4.5	A list of systematic errors in each energy bin due to event selections.	90
4.6	A list of systematic errors in each energy bin due to yield extraction.	92
4.7	Final total cross section after all event selections, total statistical uncertainty calculated using MINUIT, total systematic uncertainty calculated by adding all systematic uncertainties in quadrature, and total uncertainty by adding statistical and systematic uncertainties in quadrature.	92

LIST OF FIGURES

1.1	(Left) An illustration of The Standard Model of Particle Physics.	2
1.2	Depiction of different hadrons.	3
1.3	Pseudoscalar (0^{-+}) meson nonet.	5
1.4	(Left) The $J = \frac{3}{2}$ baryon ground-state decuplet, and (right) the $J = \frac{1}{2}$ baryon ground-state octet.	6
1.5	Depiction of the complexity inside the proton.	7
1.6	(Left) QCD factorization of the DVCS amplitude.	10
1.7	(Left) The decomposition of the proton average momentum fraction $\langle x \rangle$ by Alexandrou <i>et al.</i> in the lattice QCD framework.	11
1.8	The protons GFFs as a function of t calculated in the lattice QCD framework by Hackett <i>et al.</i>	12
1.9	Possible vector-meson dominance (VMD) model mechanisms for the near threshold J/ψ photoproduction, with 2-gluon exchange (left) and 3-gluon exchange (right).	13
1.10	Fits by Brodsky <i>et al.</i> on the data collected by Camerini <i>et al.</i> at SLAC and Gittelmann <i>et al.</i> at Cornell.	14
1.11	Fit by Kharzeev on the differential cross section at beam energy $E_\gamma = 10.72$ GeV collected by GlueX.	15
1.12	Proton GFFs calculated by Pentchev and Chudakov using GlueX data.	16
1.13	Feynman diagram for the proposed CC mechanism.	18
1.14	Comparison of the J/ψ photoproduction through open-charm loops, such as that shown in Figure 1.13, by Du <i>et al.</i> with the first GlueX published cross section.	19
1.15	Fit results by JPAC of the integrated cross section of all four models compared to GlueX data.	20
1.16	Fit results by JPAC of the differential cross section of all four models compared to GlueX data.	21
1.17	(Left) Distribution of $m(J\psi p)$ for $\Lambda_0^b \rightarrow J/\psi p K^-$ candidates.	22
1.18	Model of pentaquarks produced in the s -channel of J/ψ photoproduction.	22
1.19	JPAC prediction of the expected total J/ψ photoproduction cross section in the $P_c(4450)$ resonance region, as a function of the lab-frame photon energy E_γ	23

1.20	Strakovsky <i>et al.</i> results for new GlueX total cross sections for the reaction $\gamma p \rightarrow J/\psi p$ (blue filled circles).	24
2.1	(Left) Camerini <i>et al.</i> measurement of the invariant mass spectrum of electron-positron pairs at SLAC.	25
2.2	(Top) Camerini <i>et al.</i> cross section extrapolated to $t=0$ for J/ψ as a function of beam energy.	26
2.3	(Left) Gittelman <i>et al.</i> measured two-particle invariant mass squared spectrum.	27
2.4	(Left) The measured invariant mass spectrum of electron-positron pairs by GlueX.	29
2.5	(Left) The updated GlueX measured invariant mass spectrum of electron-positron pairs, fit with 2 Gaussian's and a linear background.	30
2.6	The updated total cross section versus beam energy measured at GlueX compared to the Cornell results and two open-charm calculations.	31
2.7	Comparison of the GlueX differential cross sections for the three energy slices to the closest in energy measurements done by Duran <i>et al.</i>	33
2.8	Layout of the J/ψ -007 experiment in Hall C.	34
2.9	Duran <i>et al.</i> differential cross sections versus t in 10 different beam energy bins.	35
3.1	Schematic of CEBAF and the four halls housed at JLab.	37
3.2	Schematic of the Hall D photon production beamline.	38
3.3	Schematic of the tagger system.	38
3.4	(Top) Photon flux as a function of beam energy for PARA ($0/90^\circ$) and PERP ($-45/45^\circ$) diamond orientations and for the aluminum radiator.	40
3.5	Schematic of the Pair Spectrometer.	41
3.6	Schematic of the GlueX beamline and spectrometer.	42
3.7	Liquid hydrogen target cell (dimensions are in mm).	43
3.8	(Left) Picture of CDC during construction.	44
3.9	(Left) Picture of the fully assembled FDC.	45
3.10	Three dimensional rendition of the BCAL.	47
3.11	(Left) Picture of the FCAL inside Hall D.	48
3.12	Start Counter and target.	49
3.13	(Left) Picture of TOF being lifted into place.	50

3.14	(Left) Picture of the installed DIRC detector.	51
3.15	Schematic data acquisition system for GlueX.	52
4.1	Momentum (p) versus polar angle (θ) distributions for positively charged muons (μ^+)	57
4.2	The 2D total energy distributions across both calorimeters for Monte Carlo (MC) simulation. Calorimeter trigger thresholds are represented by the red lines.	58
4.3	Difference between the measured time of the beam photon and RF time.	60
4.4	(Left) χ^2/NDF in Data and Monte Carlo.	61
4.5	(Left) Energy in the FCAL distribution in Data and Monte Carlo.	62
4.6	(Left) Energy divided by path length in the BCAL distribution in Data and Monte Carlo.	63
4.7	The Dalitz plots of the muon-proton ($\mu^\pm p$) mass vs the J/ψ ($\mu^\pm \mu^\mp$) mass.	64
4.8	The μ^- polar angle versus the μ^+ polar angle for both data in the J/ψ mass region (left) and Monte Carlo (right).	64
4.9	(Left) Lower θ of the μ^\pm significance distribution.	66
4.10	FCAL Shower Energy matched to muon track in the $J/\psi \rightarrow \mu^+ \mu^-$ channel.	67
4.11	David Lawrence and a undergraduate student of his looked at the projected track distance (cm) from center of nearest block (DOCA- Distance of closest approach) versus the energy (GeV) deposited in that nearest block.	68
4.12	(Left) The XY track projection to the back of the FCAL block where the hit was registered, with only events in the lower energy peak.	68
4.13	Expanded view of a single FCAL module.	69
4.14	The projected track distance from center of nearest FCAL block (DOCA- Distance of closest approach) versus the FCAL energy deposited in that shower.	70
4.15	The projected track distance from center of nearest FCAL block (DOCA- Distance of closest approach) versus the FCAL energy deposited in that shower.	71
4.16	FCAL Shower Energy matched to track.	72
4.17	Fit of the FCAL Shower Energy matched to tracks using two Gaussians to find the two peak locations.	73
4.18	FCAL Shower Energy matched to muon track in the CPP data.	74
4.19	The linear fits of light guide peak location versus the correction factor and the light guide correction factor matched to data for each particle.	75

4.20	FCAL Shower Energy matched to track.	76
4.21	(Left) BCAL shower energy deposited by muons divided by the path length in the BCAL for the $J/\psi \rightarrow \mu^+\mu^-$ data and original Monte Carlo.	77
4.22	XY projection (top) and YZ projection (bottom) of an accepted cosmic event.	78
4.23	BCAL shower energy deposited by muons divided by the path length in the BCAL for the cosmic data and original MC.	78
4.24	The $\mu^+\mu^-$ mass spectra after all selections are applied.	80
4.25	The filled blue points show the measured total cross sections obtained from Eq. 4.4 in fine photon energy bins.	81
4.26	The filled blue points show the J/ψ yields obtained from the mass fits shown in appendix A.	82
4.27	The distribution of events data in the E_γ - t plane.	83
4.28	Comparison of the differential cross sections for the three energy regions from this work to the measurements of the published $J/\psi \rightarrow e^+e^-$ GlueX results.	85
4.29	(left) The $\mu^+\mu^-$ mass spectra only for events with $-t > 1.5 \text{ GeV}^2$	86
4.30	(left) Total cross section measurement for variations of the χ^2/NDF selection.	87
4.31	(left) Total cross section measurement for variations of the Energy/Path Length in BCAL of μ^\pm selection.	87
4.32	(left) Total cross section measurement for variations of the Energy in FCAL of μ^\pm selection.	88
4.33	(left) Total cross section measurement for variations of the lower $\theta(\mu^\pm)$ selection.	89
4.34	(left) Total cross section measurement for variations of the upper $\theta(\mu^\pm)$ selection.	89
4.35	(Top left) Total cross section measurement for different background functions.	91
4.36	The filled blue points show the measured total cross sections obtained from Eq. 4.4 in fine photon energy bins.	93
5.1	(Left) The filled blue points show the measured total cross sections obtained from Eq. 4.4 in fine photon energy bins.	96
A.1	Mass distributions and fits for final cross section.	97

ABSTRACT

This dissertation presents a detailed analysis of J/ψ photoproduction near the kinematic threshold in the $J/\psi \rightarrow \mu^+\mu^-$ decay channel, based on data collected by the GlueX experiment at Jefferson Lab. The study aims to probe the structure of the proton and the underlying mechanisms of heavy vector quarkonium photoproduction, contributing to a deeper understanding of Quantum Chromodynamics (QCD) in the non-perturbative regime.

The measurement focuses on the total and differential cross-sections of J/ψ photoproduction and explores various theoretical models, including two-gluon and three-gluon exchange, open-charm contributions, and potential pentaquark states. The experimental setup, featuring a high-precision tagged photon beam and advanced particle identification techniques, allowed for the separation of J/ψ events from background processes.

The analysis of the $J/\psi \rightarrow \mu^+\mu^-$ channel yields cross-sections that complement previous measurements in the $J/\psi \rightarrow e^+e^-$ decay mode, providing new insights into gluon dynamics at low momentum transfer. This work also examines the systematic uncertainties and provides a comprehensive comparison of results with theoretical predictions, highlighting the role of gluon exchange mechanisms in the photoproduction process.

The results presented in this dissertation help refine our understanding of proton structure and QCD dynamics, offering a robust dataset for future theoretical and experimental studies in hadronic physics.

CHAPTER 1

INTRODUCTION

1.1 The Standard Model of Particle Physics

The current understanding of particle physics must begin with the Standard Model. The Standard Model, illustrated in the left plot of figure 1.1, is a theory that describes how the 12 elementary spin-half particles called fermions interact via three of the four fundamental forces (electromagnetic, weak and strong interactions – excluding gravity) through five force-carrying integer spin particles called gauge bosons. The 12 fermions are classified on how they interact and the charges they carry. All fermions interact via the weak nuclear force through the exchange of the Z^0 and W^\pm bosons, the only massive spin-1 particles in the Standard Model. The fermions which carry an electric charge (the quarks and charged leptons) interact via the electromagnetic force through an exchange of photons, the massless spin-1 particles. The fermions which carry color charge (only the quarks) interact via the strong nuclear force through an exchange of gluons. Gluons, like the photon, are massless spin-1 particles and carry no electric charge. However, they do carry a color charge and thus can interact with other gluons. This is described in the theory of the strong force called Quantum Chromodynamics, a subset of the Standard Model. Fermions are organized into three generations, each containing two quarks and two leptons. These generations are primarily distinguished by their mass, with the first generation being the lightest and the third the heaviest. The Higgs boson is the only spin-0 gauge boson and gives rise to the masses of the other particles in the Standard Model.

1.2 Quantum Chromodynamics

Quantum Chromodynamics (QCD) is the theory that describes the strong force that governs the interactions between quarks and gluons. QCD is a non-abelian gauge theory, a type of quantum field theory with symmetry group $SU(3)$. Quarks and gluons interact via the strong force determined by their color charge, a property similar to electric charge but with three types called, for example: red, green, and blue. Quarks come in one of these color charges, whereas antiquarks have the corresponding anticolor (antired, antigreen, or antiblue). Unlike photons that carry no

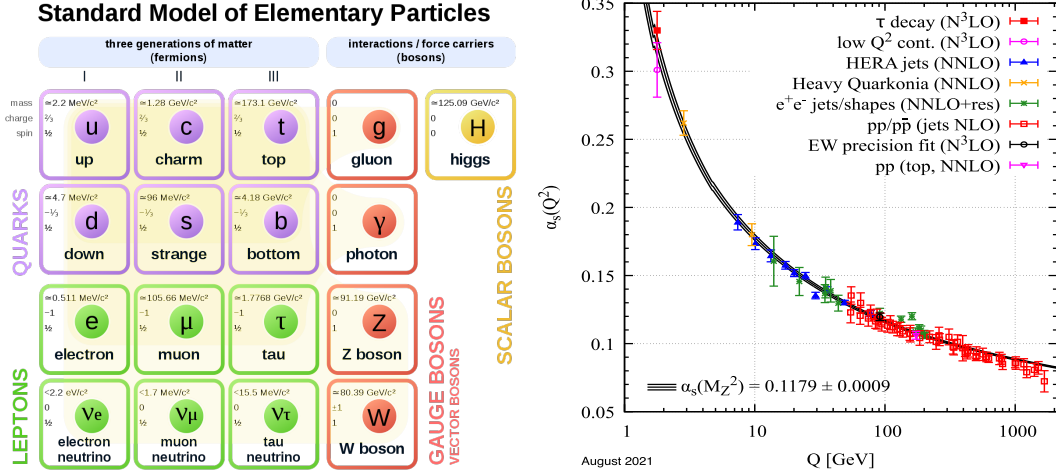


Figure 1.1: (Left) An illustration of The Standard Model of Particle Physics. The bottom left (green) boxes contain the leptons, and the top left (purple) boxes contain the quarks. The vertical column (red) displays all of the gauge bosons, responsible for mediating the fundamental forces. The far right (yellow) box contains the Higgs Boson. (Right) Several measurements of α_s as a function of the energy scale Q [1].

electric charge, gluons also carry a color charge, allowing for self-interactions. QCD exhibits three distinctive properties: (1) chiral symmetry breaking, (2) asymptotic freedom, and (3) color confinement. The first property of QCD, chiral symmetry breaking, is a consequence of the quark masses. Massless fermions conserve chirality (left-handedness and right-handedness), which is approximately true for the light-flavor quarks: up, down, and strange quarks. Spontaneous breaking of chiral symmetry gives rise to the large difference in masses of the hadrons that are formed by the quarks. It is this spontaneous chiral symmetry breaking that accounts for more than 98% of visible matter in the Universe [2]. However, since these light-flavor quarks do have mass, this symmetry is explicitly broken, giving rise to chiral perturbation theory. The last two, asymptotic freedom and color confinement, are consequences of the running of the strong coupling constant in QCD, $\alpha_S(Q^2)$ [3]. The fundamental physical constant that defines the strength of the strong force, α_S , varies considerably over the energy scales used in particle physics, shown in the right plot of Figure 1.1. As the energy scale Q increase and the length scales decrease, $\alpha_S(Q^2)$ becomes much smaller. Depending on which regime an interaction lies in determines whether perturbations on α_S can be done. High energy experiments, with $Q > 100$ GeV and $\alpha_S < 0.1$, have sufficiently small coupling constant to use perturbation theory to make calculations at this energy. This phenomenon is known as asymptotic freedom, allowing high energy experiments ($Q > 100$ GeV) to treat quarks

as quasi-free particles rather than being strongly bound. However, lower energy experiments are in the non-perturbative zone, where the quarks are strongly bound together. This is explained by the hypothesis of color confinement, which states that quarks and gluons are always confined to color-singlet states (states with overall zero color charge) called hadrons and no free particle can have a non-zero color charge. This places a restriction on the possible structure of hadrons, only allowing combinations of quarks, antiquarks and gluons that form color-singlet states. Therefore, predictions made in this spectrum of hadrons are direct tests of our understanding of this confinement mechanism of QCD at lower energies [4].

The vast majority of discovered hadrons can be classified in two groups: baryons, made of 3 valence quarks, and mesons, made of a quark and antiquark pair. However, QCD allows for other bound states, such as tetraquarks and pentaquarks, that are still colorless, but very few candidates of these exotic hadrons have been found. Since gluons also carry color charge, they can contribute to the quantum numbers of the hadron and can form exotic hadrons such as hybrid mesons, which add one or more valence gluons to the valence quark-antiquark pair, and glueballs, which consist of only valence gluons and no valence quarks. All of these are depicted in Figure 1.2. The field of study that studies these hadrons is called hadronic physics, to which this dissertation contributes. Because of the non-perturbative nature in this regime, multiple models have been devised to understand hadronic interactions. These different models and how this analysis can contribute will be discussed later in this chapter.

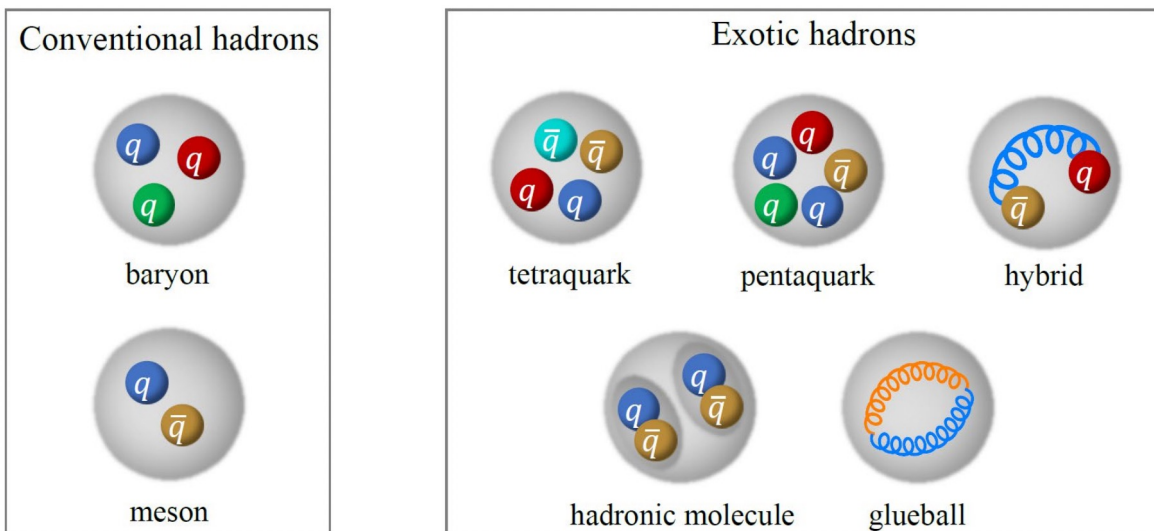


Figure 1.2: Depiction of different hadrons.

1.3 The Constituent Quark Model

In 1964, Murray Gell-Mann [5] and George Zweig [6] independently proposed a structure that explains the boom of particle discovery that started in the 1950's called the "particle zoo". They each proposed that these particles are actually composite particles made of three flavors of smaller particles that Gell-Mann called quarks, a framework later coined "The Constituent Quark Model". These flavors of quarks (up (u), down (d), and strange (s)) form a $SU_{\text{flavor}}(3)$ symmetry, assuming they all have the same mass. We now know this is not a perfect symmetry since the quarks do have different masses; however, this framework was able to predict a few future discoveries and provide a way to classify mesons and baryons [7].

The constituent quark model describes mesons as bound states of a quark-antiquark ($q\bar{q}$) pair and baryons as bound states of 3 quarks (qqq). Since the quarks are fermions (spin-1/2 particles), the total spin, \mathbf{S} , of a meson must be either 0 or 1 while the total spin of a baryon must be either 1/2 or 3/2. When you combine this with the relative orbital momentum, \mathbf{L} , between the quarks, we see that a hadron's total angular momentum is thus $\mathbf{J} = \mathbf{S} \oplus \mathbf{L}$. For any given \mathbf{S} and \mathbf{L} , the total angular momentum \mathbf{J} can be the values $\mathbf{J} = |\mathbf{L} - \mathbf{S}|, |\mathbf{L} - \mathbf{S} + \mathbf{1}|, \dots, |\mathbf{L} + \mathbf{S}|$. There are two quantum numbers (parity (\mathbf{P}), and charge conjugation (\mathbf{C})) that are conserved in strong interactions and are related to the \mathbf{S} and \mathbf{L} through the relations:

$$P = (-1)^{L+1} \quad C = (-1)^{S+L}. \quad (1.1)$$

Rather than classifying mesons in terms of their \mathbf{S} and \mathbf{L} , the usual convention is to use their \mathbf{J}^{PC} . From the eq. 1.1, the allowed \mathbf{J}^{PC} values for mesons are

$$0^{-+}, 0^{++}, 1^{-+}, 1^{+-}, 1^{--}, 2^{-+}, 2^{-+}, 2^{++}, 3^{-+}, 3^{+-}, 3^{--}, \dots$$

while the following are forbidden by the quark model

$$0^{--}, 0^{+-}, 1^{-+}, 2^{+-}, 3^{-+}, \dots$$

Mesons with these forbidden \mathbf{J}^{PC} values are called exotic mesons.

Since baryons are fermions, charge conjugation is not a useful quantum number. Instead, another symmetry of the strong force is used called isospin (\mathbf{I}), which is a symmetry of the u and d quarks. This is not a perfect symmetry, but in the case of strong interactions, it is nearly conserved because $m_d - m_u \ll \Lambda_{QCD}$ [8]. Because of the closeness in mass of u and d quarks, hadrons made

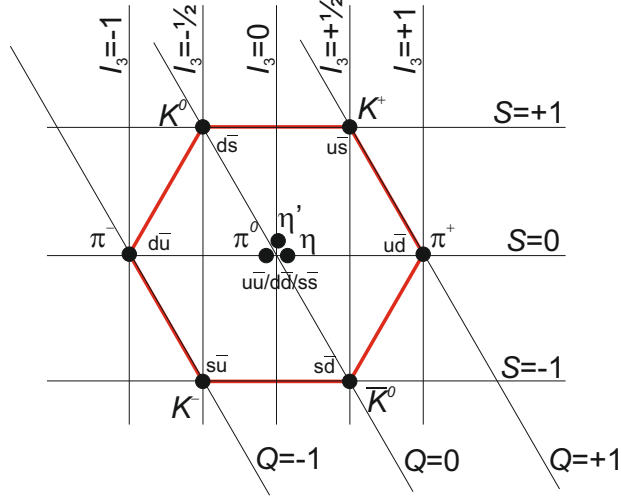


Figure 1.3: Pseudoscalar (0^{-+}) meson nonet. Vertical lines indicate the isospin projection, diagonal lines indicate the charge, and horizontal lines indicate the strangeness. Figure taken from Ref [9].

of the same number of u and d quarks have similar mass. However, the exact number of u and d quarks determines the hadrons charge since the $Q_u = \frac{2}{3}$ and $Q_d = -\frac{1}{3}$. This difference in charges gives rise to the isospin projection, I_3 . Both the u and d quarks have total isospin $\mathbf{I} = \frac{1}{2}$ (while all other quarks have $\mathbf{I} = 0$), but have different projections with $I_3(u) = \frac{1}{2}$ and $I_3(d) = -\frac{1}{2}$. This gives rise to hadrons with similar mass but different charges and isospins. For instance, the Δ baryon has $\mathbf{I} = \frac{3}{2}$. Its "charged states" $\Delta^{++}(uuu)$, $\Delta^+(uud)$, $\Delta^0(udd)$, and $\Delta^-(ddd)$ all have similar mass (≈ 1.232 GeV) but have corresponding isospin projections $I_3 = +\frac{3}{2}, +\frac{1}{2}, -\frac{1}{2},$ and $-\frac{3}{2}$, respectively. The isospin projection can be calculated using

$$I_3 = \frac{1}{2}((n_u - n_{\bar{u}}) - (n_d - n_{\bar{d}})) \quad (1.2)$$

This can also be a useful quantum number for mesons, specifically those with no $u\bar{u}$ or $d\bar{d}$ quark content.

Using these quantum numbers, Murray Gell-Man and Yuval Ne'eman independently and simultaneously proposed "The Eightfold Way", an organizational scheme for hadrons that led to the quark model. It organized mesons into octets plus a singlet (often referred to as a nonet) based on spin, strangeness (the number of strange quarks a hadron has), and charge. This nonet arises because we can form nine mesons with the same J^{PC} , since the mesons are pairs of $q\bar{q}$ and we had (at the time) 3 flavors of quarks. With this $SU_{\text{flavor}}(3)$ symmetry group, we can build the nine mesons

$$\mathbf{3} \otimes \bar{\mathbf{3}} = \mathbf{1} \oplus \mathbf{8},$$

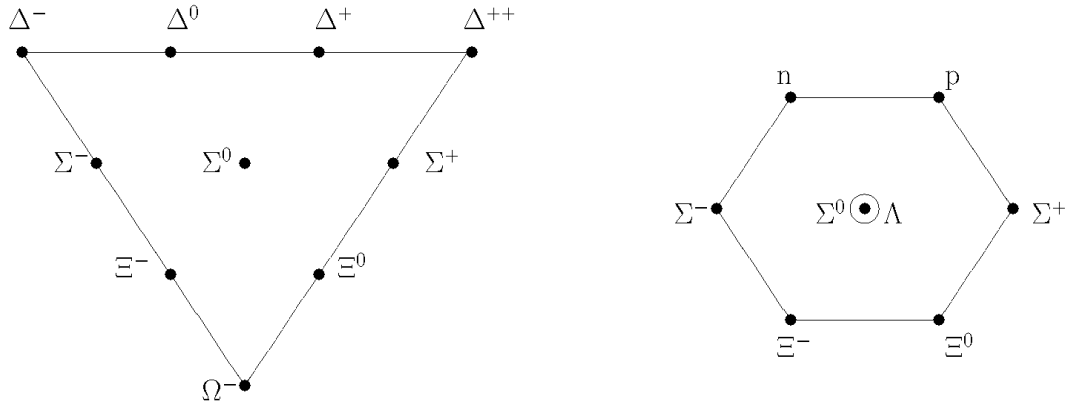


Figure 1.4: (Left) The $J = \frac{3}{2}$ baryon ground-state decuplet, and (right) the $J = \frac{1}{2}$ baryon ground-state octet. Figure taken from Ref [10].

forming a nonet. An example of the spin-0 and negative parity ($J^{PC} = 0^{-+}$) meson nonet can be seen in Figure 1.3. Here, the vertical lines indicate the isospin projection, the diagonal lines indicate the charge, and the horizontal lines indicate the strangeness. Since baryons have 3 quarks, we get 27 baryons with the same J^{PC} . Using the $SU_{\text{flavor}}(3)$ symmetry group, we get

$$\mathbf{3} \otimes \mathbf{3} \otimes \mathbf{3} = \mathbf{1} \oplus \mathbf{8} \oplus \mathbf{8} \oplus \mathbf{10}.$$

This gives a singlet, two octets, and a decuplet. Due to degeneracies ($uds = dus$), this decreases depending on the total angular momentum, J , of the baryon. The $J = \frac{3}{2}$ baryon decuplet and $J = \frac{1}{2}$ baryon octet are shown in Figure 1.4.

1.4 The Proton and Its Structure

The proton, discovered by Rutherford in 1919 [11], is the building block of all matter that we see, and understanding it is one of the keys to understanding the universe. The proton is a baryon made of 3 valence quarks: two up quarks and one down quark. It has a mass of $938.27208816 \pm$

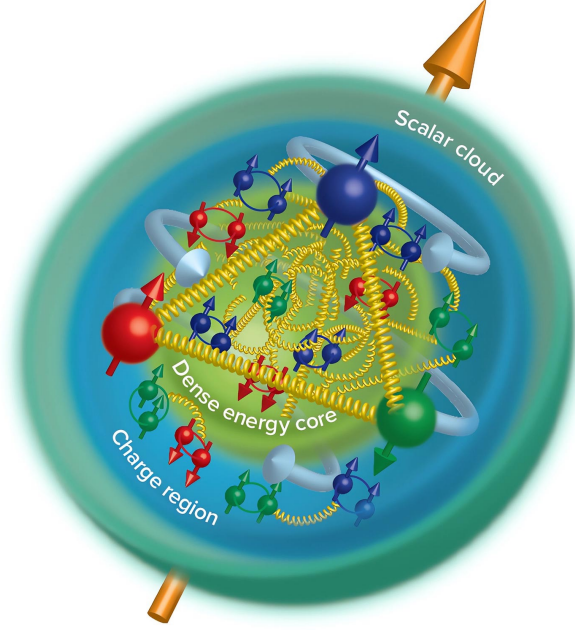


Figure 1.5: Depiction of the complexity inside the proton. The red, blue and green spheres represent the quarks, with the large spheres representing the valence quarks (two ups and one down quark). The gluons are represented as yellow, spring-like lines connecting the quarks. Image by Argonne National Laboratory.

0.00000029 GeV and a positive electric charge of $+1e$ [1]. Soon after the discovery of the neutron by Chadwick in 1932 [12], the proton and neutron were experimentally found to be non-pointlike fermions. In 1933, Frisch and Stern found that the proton had a magnetic moment $\mu_p \approx 2.5\mu_N$. The nuclear magneton, $\mu_N = \frac{e\hbar}{2M_N}$, is the value predicted by the Dirac equation for the proton if it were a point-like particle. This discovery by Frisch and Stern, and the later discovery of the non-zero neutron magnetic moment by Alvarez and Bloch in 1940, gave birth to a new subfield of particle physics, nucleon structure. It became a primary goal of particle physics to understand the structure of the proton, specifically where does this mass and electric charge come from and how are they distributed throughout the proton.

Experimentally, we began to understand the charge distribution of the proton through electron-proton scattering experiments. These experiments consist of colliding high-energy electrons with protons and analyzing the scattered electrons. When an electron collides with a proton, the interaction is only determined by the electromagnetic force, since the electron is a lepton. Because of this, the scattered electron data provides clues about the distribution of electric charge and magnetic moment within the proton. To understand the deviations from the point-like structure, we can use

this data to study the electromagnetic form factors (FFs) of the proton. The electromagnetic form factors are defined by the matrix elements of the electromagnetic current operator, j^μ , given by the equation [13]:

$$\langle p' | j^\mu(0) | p \rangle = F_1(q^2) \gamma^{mu} + \kappa F_2(q^2) \frac{i \sigma^{\mu\nu} q_\nu}{2m_p}, \quad (1.3)$$

where F_1 and F_2 are the electromagnetic form factors for the proton, m_p is the mass of the proton, and κ is the anomalous part of the magnetic moment. F_1 and F_2 , which are constant when the fermion is pointlike, can be related to the Fourier transform of the charge and current distributions in the proton, as shown in equation 1.4:

$$F_1(Q_2) = \int \rho(\vec{x}) e^{i\vec{q}\cdot\vec{x}} d^3x \quad \text{and} \quad F_2(Q_2) = \int \vec{j}(\vec{x}) \times d^3\vec{x} e^{i\vec{q}\cdot\vec{x}} \quad (1.4)$$

As $Q^2 \rightarrow 0$, F_1 and F_2 correspond to the electric charge and anomalous magnetic moment, respectively [14].

To relate these FFs to observable, we can use the Rosenbluth Formula [15]:

$$\frac{d\sigma}{d\Omega}|_{lab} = \left(\frac{\alpha^2}{4E^2 \sin^4(\theta/2)} \right) \frac{E'}{E} \left\{ \left(F_1^2 - \frac{\kappa^2 q^2}{4M^2} F_2^2 \right) \cos^2(\theta/2) - \frac{q^2}{2M^2} (F_1 + \kappa F_2)^2 \sin^2(\theta/2) \right\}, \quad (1.5)$$

where θ is the scattering angle of the electron and q^2 is the momentum transfer between the incident electron and the proton. In 1956, McAllister and Hofstadter used this q^2 dependence of F_1 and F_2 in electron-proton scattering to make the first measurement of the charge radius of the proton, which they found to be 0.74 ± 0.24 fm [16]. Since this measurement by McAllister and Hofstadter, many more electron-proton scattering experiments have been performed to calculate the proton's charge radius with even greater precision, the most recent of which by Xiong *et al.* in 2019 gives a value of $0.831 \pm 0.007 \pm 0.012$ fm [17]. However, two other methods have been developed to find the charge radius of the proton using the lamb shift of electronic hydrogen (proton orbited by a single electron) and muonic hydrogen (proton orbited by a single muon). The most recent electronic hydrogen measurement by Bezginov *et al.* in 2019 found $r_p = 0.833 \pm 0.010$ fm [18], while the most recent muonic hydrogen measurement (and the most precise of all the measurements) by Antognini *et al.* in 2013 found $r_p = 0.84087 \pm 0.00026 \pm 0.00029$ fm [19]. Before the more recent measurements by Xiong *et al.* and Bezginov *et al.* in 2019, the majority of measurements using the electron-proton scattering and the electronic hydrogen methods found values closer to 2014 recommendation by the Committee on Data of the International Science Council (CODATA) of 0.8751 ± 0.0061 fm [1]. This 5.6σ difference from the muonic hydrogen measurement by Antognini

et al. was coined the "proton charge radius puzzle." However, after the recent measurements and new recommendation by CODATA in 2018 of $r_p = 0.8414 \pm 0.00019$ fm [20], this puzzle appears to be resolved, with the Antognini *et al.* measurement cited as the current value [1].

Though these scattering experiments can tell us a lot about the charge and magnetic moment distributions in the proton, they cannot provide any information about the mass or spin distribution of the proton. Because the protons mass and spin primarily comes from the quarks and gluons in the proton, we need strong interactions to probe the mass and spin distribution of the proton. Similar to how we gain information about the charge distribution in the proton through the matrix elements of the electromagnetic current operator, we can gain mass and spin information of the proton by studying the matrix elements of the energy-momentum tensor (EMT) operator $\langle p', \vec{s}' | T_a^{\mu\nu} | p, \vec{s} \rangle$ of the quarks and gluons, where $|p, \vec{s}\rangle$ is the initial state of the quark or gluon with momentum p polarized along the \vec{s} direction, $T_a^{\mu\nu}$ is the EMT operator, and $\langle p', \vec{s}' |$ is the final state of that quark or gluon. Using Poincaré symmetry, we can write these matrix elements as [21],

$$\begin{aligned} \langle p', \vec{s}' | T_a^{\mu\nu}(0) | p, \vec{s} \rangle = \bar{u}(p', \vec{s}') \left[A_a(t) \frac{P^\mu P^\nu}{M_N} + J_a(t) \frac{P^{\{\mu} i \sigma^{\nu\} \lambda} \Delta_\lambda}{M_N} + D_a(t) \frac{\Delta^\mu \Delta^\nu - g^{\mu\nu} \Delta^2}{4M_N} \right. \\ \left. - S_a(t) \frac{P^{[\mu} i \sigma^{\nu] \lambda} \Delta_\lambda}{M_N} + \bar{C}_a(t) M_N g^{\mu\nu} \right] u(p, \vec{s}), \end{aligned} \quad (1.6)$$

where the kinematic variables are defined as $P = \frac{1}{2}(p' + p)$, $\Delta = p' - p$, $t = \Delta^2$. The t -dependent coefficients $A_a(t)$, $D_a(t)$, $\bar{C}_a(t)$, $J_a(t)$, and $S_a(t)$ are the EMT analogues to the electromagnetic form factors mentioned above and are labeled gravitational form factors (GFFs). However, unlike electromagnetic form factors, GFFs cannot be measured directly since they require measurement of the graviton-proton interaction [14]. Instead, many methods have been developed to indirectly measure GFFs through various exclusive processes. The first and most explored process that gives access to the GFFs is deeply virtual Compton scattering (DVCS), exemplified on the left in Figure 1.6. DVCS is the scattering of high-energy electrons off protons by exchanging a deeply virtual photon, producing a real photon in the final state [14]. In the high-energy limit, we can factorize this interaction into an upper, "hard" part that can be perturbatively calculable using QCD and a lower, "soft" part that is described by generalized parton distributions (GPDs), which represent the probability density for finding a parton with longitudinal momentum fraction x in the target [22]. These GPDs can be directly related to the gravitational form factors discussed above, two of which are as follows

$$\int_{-1}^1 dx x H_q(x, \xi, t) = A_q(t) + \xi^2 D_q(t) \quad \text{and} \quad \int_{-1}^1 dx x E_q(x, \xi, t) = 2J_q(t) - A_q(t) - \xi^2 D_q(t) \quad (1.7)$$

where ξ , called skewness, represents the longitudinal momentum transfer to the struck quark from the initial to final state shown in figure 1.6. However, the actual observables in DCVS are Compton form factors (CFFs) that are related to measurable quantities such as different cross sections and polarization asymmetries. These CFFs are expressed, using factorization formulae, in terms of complex-valued convolution integrals of the GPDs [14]. To go from the CFFs to the GPDs, these convolution integrals must be inverted, a process that is model-dependent. This, along with the fact that DVCS cross sections are very small, makes it difficult to extract model-independent gravitational form factors from DVCS.

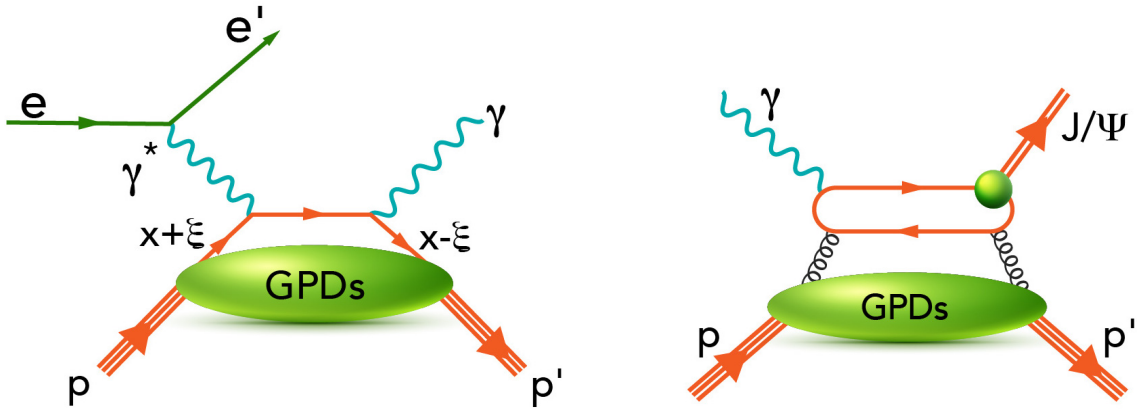


Figure 1.6: (Left) QCD factorization of the DVCS amplitude. The perturbatively calculable “hard part” is shown to lowest order in the strong coupling. The nonperturbative “soft part” is described by the universal quark GPDs. (Right) Possible model of threshold J/ψ photoproduction on the proton. [14].

The other process that has been proposed to indirectly measure the gravitational form factors of the proton is heavy vector quarkonium photoproduction, the primary discussion of this disertation. Shown on the right in Figure 1.6, we see a model of J/ψ photoproduction on the proton that could lead to extractions of the gluon GFFs. This model, along with others models of J/ψ photoproduction, will be the discussion of the next section.

To compliment these insights from indirect measurements, lattice QCD (LQCD) calculations have given us direct predictions for this non-perturbative regime of QCD. These calculations discretize the QCD Lagrangian onto a Euclidean space-time lattice with some finite lattice spacing. Monte-Carlo integration is then performed on the high-dimensional discretized path-integrals, and in doing so, computes the matrix elements of local operators, such as the quark and gluon com-

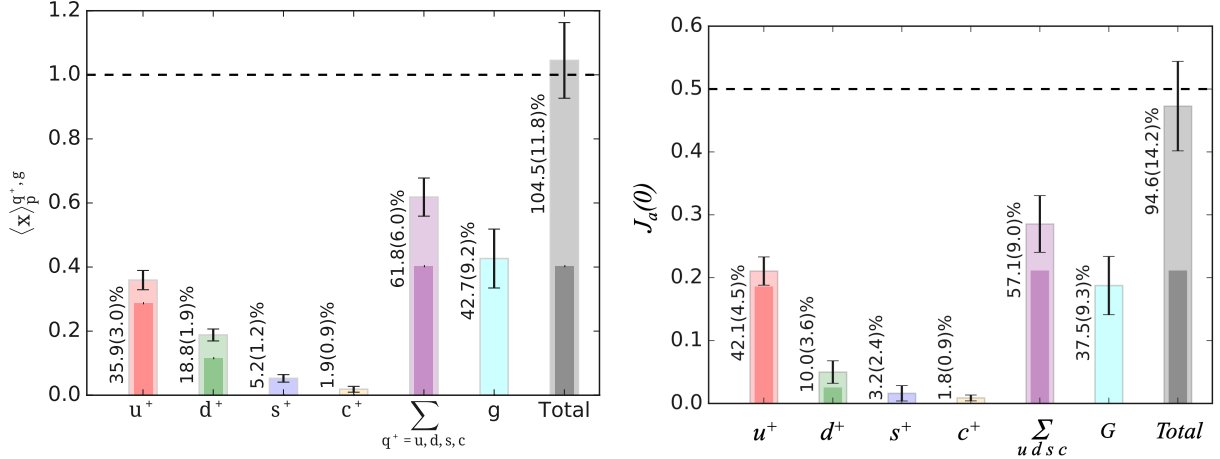


Figure 1.7: (Left) The decomposition of the proton average momentum fraction $\langle x \rangle$ by Alexandrou *et al.* in the lattice QCD framework. They show the contribution of the up (red bar), down (green bar), strange (blue bar), charm (orange bar), quarks and their sum (purple bar), the gluon (cyan bar) and the total sum (grey bar). Each component includes the contribution of both the quarks and antiquarks ($q^+ = q + \bar{q}$); outer/light (inner/dark) shaded bars denote the total (purely connected) contributions. The error bars for the former are omitted while for the latter are shown explicitly on the bars. The percentages written in the figure are for the total contribution. (Right) Proton spin decomposition ($J_a(t)$ GFF at $t = 0$) computed in lattice QCD by Alexandrou *et al.* [23].

ponents of the EMT in the proton. By computing these matrix elements, one can decompose the protons GFFs into individual quark and gluon contributions. In Figure 1.7, we see the work done by Alexandrou *et al.* in 2020 where they compute the percentage contribution of quarks and gluons to the protons average momentum fraction $\langle x \rangle$, which is directly related to the GFFs $A_a(t = 0)$, and the protons spin $J_a(t = 0)$ [23]. Taken a step further, Hackett *et al.* calculated, for the first time, the t -dependence ($|t| < 2 \text{ GeV}^2$) of the protons GFFs and the contributions from quarks and gluons, shown in Figure 1.8. Hackett *et al.* used these results to calculate the mass radius of the proton and how quarks and gluons individually contribute to it. They found that though quarks and gluons equally contribute to each of the GFFs, the gluons extend the radial size of the proton compared to the quarks [24]. Much effort has gone into calculating the GPDs of the proton using lattice calculations. This is particularly difficult because GPD calculations cannot be done using the Euclidean lattice formulation of QCD, but some initial results by Alexandrou *et al.* in 2020 can be found here [25].

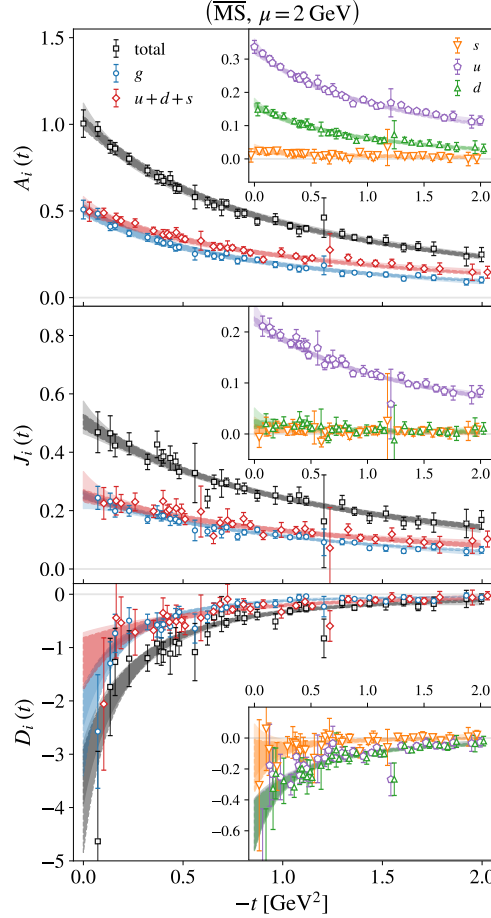


Figure 1.8: The protons GFFs as a function of t calculated in the lattice QCD framework by Hackett *et al.* They decompose them into the quark and gluonic contributions, with the inset figures showing the specific up, down, and strange quark contributions [24].

1.5 Models of J/ψ Photoproduction

As mentioned previously, J/ψ photoproduction at threshold has been suggested as a tool to gain insight into the structure of the proton. This section will cover the different models of J/ψ photoproduction at threshold, starting with those similar to the one on the right in Figure 1.6 that describes the interactions via gluonic exchange. We will then discuss other models that could contribute to the cross section, specifically these "open-charm exchange" models and possible s-channel contributions from pentaquarks.

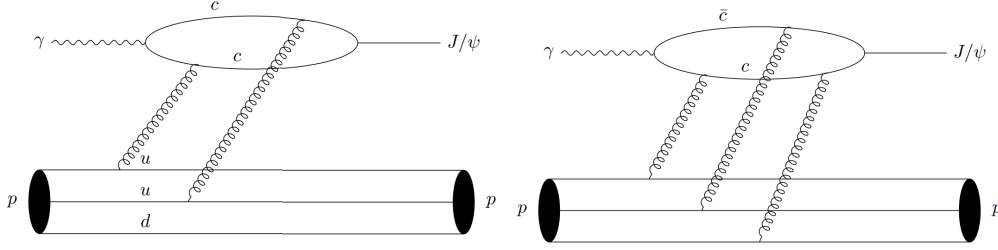


Figure 1.9: Possible vector-meson dominance (VMD) model mechanisms for the near threshold J/ψ photoproduction, with 2-gluon exchange (left) and 3-gluon exchange (right) [26].

1.5.1 Gluonic Exchange

Deeply virtual meson production (DVMP) is another process sensitive to the GPDs of the proton, assuming factorization holds. As shown in the right plot of Figure 1.6, DVMP involves the production of a meson (e.g., a J/ψ) in the final state through the interaction with a proton. Collins *et al.* [27] demonstrated that charmonium photoproduction should factorize in the heavy quark limit, making it a particularly promising probe of GPDs. They suggest charmonium photoproduction should be dominated by gluonic exchange mechanisms because of this factorization. In 1999, Kharzeev *et al.* published a paper [28] that calculated the J/ψ photoproduction cross section in terms of the gluon distribution function of the proton. They begin by assuming Vector Meson Dominance (VMD), the common approach to understanding photoproduction interactions where the incoming photon oscillates into a vector meson with the same J^{PC} as the photon of 1^{--} such as the ρ , ω , ϕ or J/ψ . Using the VMD approach, they can relate the differential cross section of the reaction $\gamma P \rightarrow J/\psi P$ to the reaction $J/\psi P \rightarrow J/\psi P$ using the equation:

$$\frac{d\sigma_{\gamma P \rightarrow J/\psi P}}{dt}(s, t=0) = \frac{3\Gamma(J/\psi \rightarrow e^+e^-)}{\alpha m_{J/\psi}} \left(\frac{k_{J/\psi P}}{k_{\gamma P}} \right)^2 \frac{d\sigma_{J/\psi P \rightarrow J/\psi P}}{dt}(s, t=0), \quad (1.8)$$

where $k_{ab}^2 = [s - (m_a + m_b)^2][s - (m_a - m_b)^2]/4s$ and Γ is the branching ratio of $J/\psi \rightarrow e^+e^-$. The differential cross section of $J/\psi P \rightarrow J/\psi P$ is then related to the $J/\psi P$ scattering amplitude, giving a relation of the differential cross section of the reaction $\gamma P \rightarrow J/\psi P$ in terms of the $J/\psi P$ scattering amplitude. Kharzeev *et al.* then proceeds to relate, by the use of operator product expansion (OPE), the $J/\psi P$ scattering amplitude in terms of the proton's gluonic distribution, $g(x, \epsilon_0^2)$. He argues, similar to what is done for DCVS, that the scattering amplitude factorizes into a short distance part describing the interaction of the $c\bar{c}$ pair that forms the J/ψ and the gluonic interaction of the $c\bar{c}$ with the proton, shown in the right plot of Figure 1.6. After some

simplification and using the optical theorem, they derive a new sum rule for the $J/\psi P$ cross section:

$$\sigma_{J/\psi P}^{(0)} = \frac{8\pi}{9} \left(\frac{32}{3}\right)^2 \frac{1}{\alpha_S m_c^2} \int_{\epsilon_0/\lambda}^1 dx \frac{((x\lambda/\epsilon_0) - 1)^{3/2} g(x, M_q^2)}{(x\lambda/\epsilon_0)^5 x}, \quad (1.9)$$

where m_c is the J/ψ mass and $\epsilon_0 = m_c \left(\frac{3\alpha_s}{4}\right)^2$ is the Rydberg energy of the J/ψ [28].

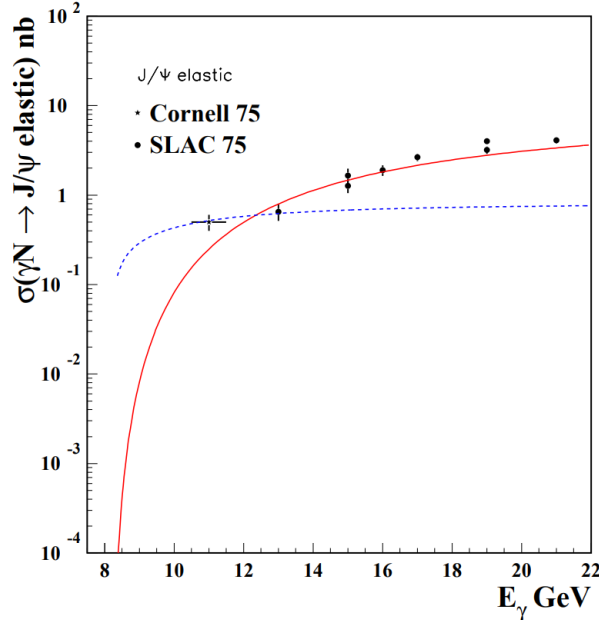


Figure 1.10: Fits by Brodsky *et al.* [29] on the data collected by Camerini *et al.* at SLAC [30] and Gittelmann *et al.* at Cornell [31]. Solid line is using two gluon exchange and the dashed line is using three gluon exchange.

The next year, in October of 2000, Brodsky *et al.* published a paper [29] where they looked at J/ψ photoproduction in terms of hard scattering processes that scale with beam energy. They argue that at the J/ψ photoproduction threshold, the valence quarks of the proton must interact coherently within the small interaction volume of the charm quark production. As a consequence, the J/ψ photoproduction at threshold is sensitive to short-range correlations between the valence quarks of the proton. Thus, unlike at higher energies where single-gluon exchange subprocesses dominate, they argue at threshold multi-gluon exchange reactions, such as those shown in Figure 1.9, contribute greatly to J/ψ photoproduction. Using these 2 and 3 gluon exchange diagrams, they derive the following forms of the differential cross section of the $\gamma P \rightarrow J/\psi P$ reaction in terms of the form factors, F_{2g} and F_{3g} , of the proton:

$$\frac{d\sigma}{dt} = N_{2g} v \frac{(1-x)^2}{R^2 m_{J/\psi}^2} F_{2g}^2(t) (s - m_p^2)^2 \quad \text{and} \quad \frac{d\sigma}{dt} = N_{3g} v \frac{(1-x)^0}{R^4 m_{J/\psi}^4} F_{3g}^2(t) (s - m_p^2)^2, \quad (1.10)$$

where N is a normalization coefficient, R is the proton radius, $v = 1/16\pi(s - m_p^2)^2$ is the phase space factor, and x is the fraction of proton momentum that the valence quarks carries. They use these expressions to fit the only available J/ψ photoproduction data near threshold collected in 1975 by Camerini *et al.* at SLAC [30] and Gittelman *et al.* at Cornell [31], which will be discussed in chapter 2. The fits are shown in figure 1.10.

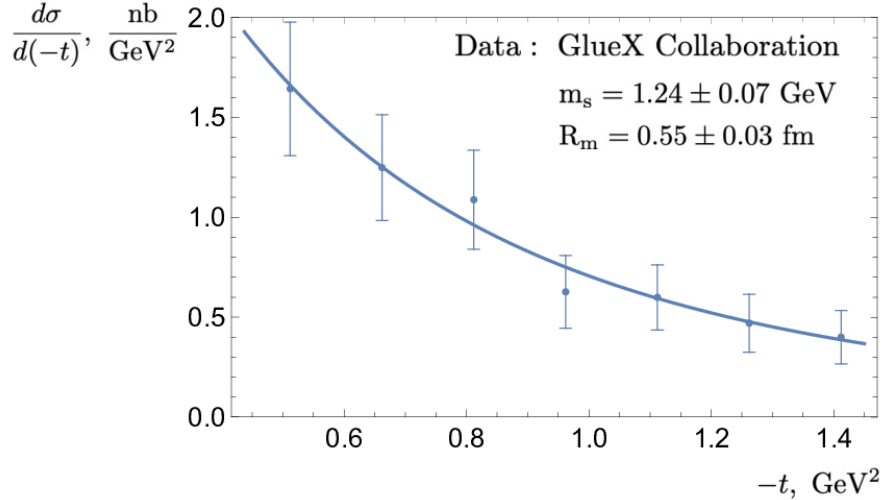


Figure 1.11: Fit by Kharzeev [32] on the differential cross section at beam energy $E_\gamma = 10.72$ GeV collected by GlueX [33]. Theory curve corresponds to the dipole form of the scalar gravitational form factor with parameter $m_s = 1.24 \pm 0.07$ GeV, which corresponds to a proton mass radius $R_m = 0.55 \pm 0.03$ fm.

In 2019, GlueX published its first measurement of J/ψ photoproduction near threshold using the decay of $J/\psi \rightarrow e^+e^-$ [34], which will be discussed in detail in chapter 2. This sparked renewed interest from the hadronic theory community. In February 2021, Kharzeev published a follow-up [32] to the 1999 publication [28]. Using the same arguments discussed in the 1999 publication, Kharzeev derives the differential cross section in terms of the gravitational form factors of the proton.

He takes it a step further and derives the protons mass radius from the dipole form of the scalar gravitational form factor of the proton. Similar to how the charge radius is defined through the derivative of the electromagnetic form factor [35], he defines the mass radius using the equation:

$$\langle R_m^2 \rangle = \frac{6}{m_p} \frac{dA}{dt} \Big|_{t=0}, \quad (1.11)$$

where A is the scalar gravitational form factor. Using the data collected by GlueX, Kharzeev fits the differential cross section to find the proton mass radius to be $R_m = 0.55 \pm 0.03$ fm, shown in Figure 1.11. In this paper, Kharzeev also mentions that because of the large mass of J/ψ , there is a large minimal momentum transfer, $t_{min} \approx -1.5$ GeV². This large t_{min} brings into question the validity of the VMD model, where t_{min} needs to be much smaller than $4m_{quark}^2$. In this case, $4m_{charm}^2 \approx 6.25$ GeV², which is greater than t_{min} . He argues this is a large enough difference to still believe that the VMD model is valid.

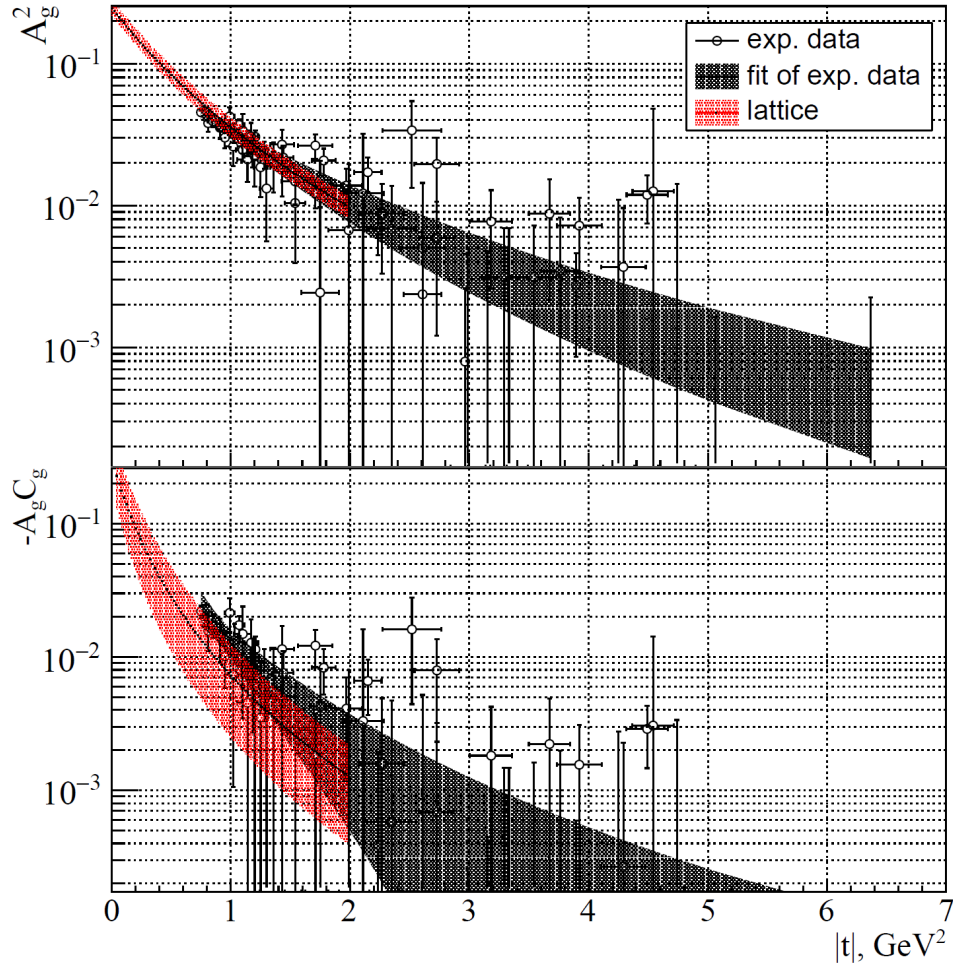


Figure 1.12: Proton GFFs calculated by Pentchev and Chudakov using GlueX data [36]. A_g form factor squared (top), and the product of the two form factors with negative sign $A_g C_g$ (bottom), extracted from the GlueX data within the leading-moment approximation using Guo *et al.* formalism [37], fitted with dipole functions (one-sigma error band shown) and compared to the lattice results by Hackett *et al.* [24]

Soon after, many others used similar methods and arguments to look at other aspects of the

proton, including the effect on the protons gravitational form factors [38] and the protons GPD's [39, 37]. Sun *et al.* [39] looked specifically at the effect at large momentum transfer, where they argue that QCD factorization is more valid. Since the derivation of the protons GFF's and GPD's are largely dependent on the validity of QCD factorization, they focus solely on the high- t regime. In 2024, Guo *et al.* [37] looked at J/ψ photoproduction in terms of the skewness, ξ , of the reaction, specifically large ξ and its affect on the GFF's. Guo *et al.* argues that because of the large changes in t_{min} with beam energy, it is better to look at high ξ to validate the factorization assumption, because ξ is dependent on both momentum transfer and beam energy. Pentchev and Chudakov [36] used GlueX data and the formalism by Guo *et al.* [37] to extract the gravitational form factors directly from the data and use fits to data, similar to that used by Sun *et al.*, to compare with lattice calculations discussed above [24]. The results can be seen in figure 1.12. With relative agreement between lattice calculations, dipole fits to data, and extractions directly from the data, Pentchev and Chudakov conclude that the ξ -scaling arguments by Guo *et al.* [37] seem to hold for $\xi > 0.4$, at least within errors.

1.5.2 Open-Charm Exchange

One interesting feature of the 2019 GlueX published cross section [33], shown in figure 1.14, was that it featured a dip around 9.1 GeV. The dip in the cross section, if it is not just statistical fluctuations, is of particular interest because it cannot be explained by the gluonic exchange models described in the previous section. This feature, along with the discovery by LHCb of the pentaquark states in the $J/\psi p$ spectrum [41, 42, 43] discussed in the next section, led Du *et al.* [40] to look at the effect of open-charm exchange models, such as that shown in figure 1.13, contribute to the $J/\psi p$ cross section. If these open-charm exchange models do contribute, this would be significant since these models violate factorization and Vector Meson Dominance, which are crucial assumptions in the gluonic exchange models.

With the $\Lambda_c^+ \bar{D}^0$ and $\Lambda_c^+ \bar{D}^{*0}$ thresholds just 116 MeV and 258 MeV above the J/ψ threshold, respectively, they argue that these rescattering mechanisms could contribute sizable. Interestingly, these proposed open-charm mechanism thresholds sandwich the dip that was seen in the GlueX data, shown in figure 1.14. They suggest that these $\Lambda_c \bar{D}^{(*)}$ thresholds would appear as cusps in the J/ψ photoproduction cross section, shown in Figure 1.14. These cusps align well with the dip in the cross section seen by GlueX.

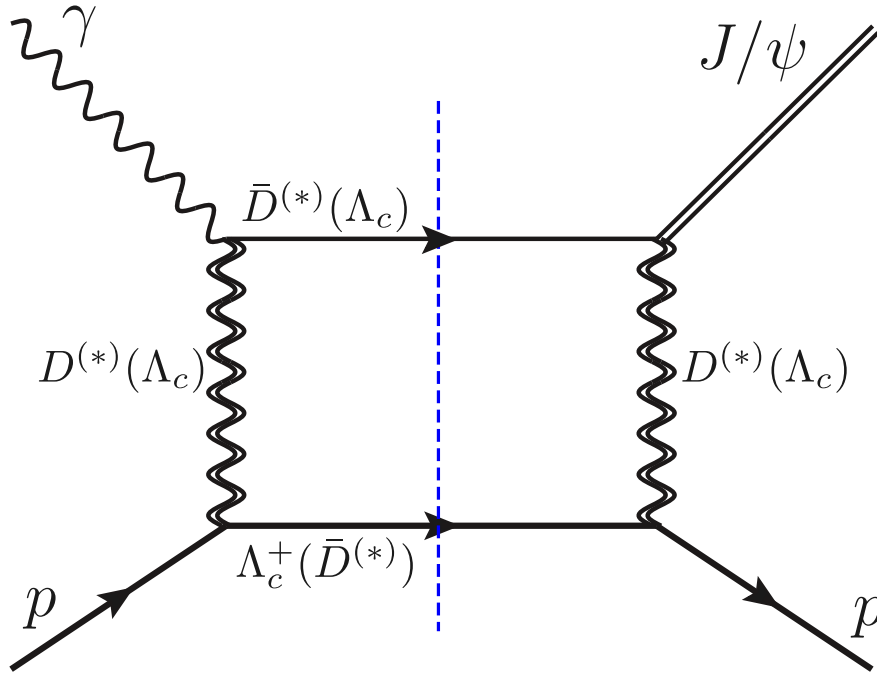


Figure 1.13: Feynman diagram for the proposed CC mechanism. The dashed blue line pinpoints the open-charm intermediate state [40].

In February 2023, Duran *et al.* published their data on the J/ψ photoproduction using the J/ψ -007 experiment in Hall C of Jefferson Lab [44], discussed in greater detail in chapter 2. Interestingly, they found the differential cross section began to flatten out at high- t near threshold, shown in Figure 1.15. Like with the dip in cross section, this flattening of the differential cross section at high- t near threshold cannot be explained by the gluonic exchange models. In April of that same year, GlueX updated their results [34] and published both the cross section and the differential cross section with 4 times the amount of data from the first publication. Two interesting features were found: first, the dip in the cross section around 9.1 GeV became more pronounced with more statistics and smaller error bars, and second, the differential cross section also began to flatten out at high- t near threshold, like what Duran *et al.* found. This sparked a renewed interest in the effect of open-charm exchange models to J/ψ photoproduction.

In September 2023, the Joint Physics Analysis Center (JPAC) published a paper [45] that looked at the newly published data by GlueX and Duran *et al.* They aimed to describe the photoproduction amplitude in a generic form, using a small number of s-channel partial waves. They looked at four models, including gluonic exchange and open-charm exchange models, of J/ψ photoproduction and

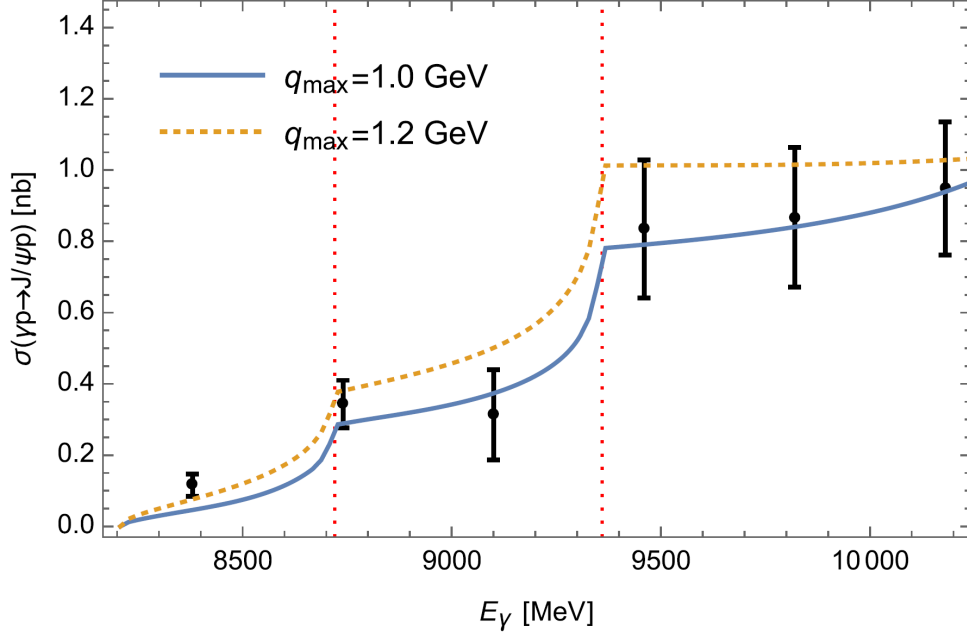


Figure 1.14: Comparison of the J/ψ photoproduction through open-charm loops, such as that shown in Figure 1.13, by Du *et al.* [40] with the first GlueX published cross section [33]. The vertical dashed lines represent the $\Lambda_c \bar{D}^{(*)}$ thresholds.

find which ones best describe the recently published data. The four models they look at include what they call "Single Channel" (1C), where only gluonic exchange models are considered, "Two Channel" (2C), where they add contributions from an intermediate $\Lambda_c \bar{D}^*$ channel, and "Three Channel" (3C), where they include contributions from both intermediate $\Lambda_c \bar{D}^{(*)}$ channels. In the 3C case, these intermediate $\Lambda_c \bar{D}^{(*)}$ channels were found to have two distinct fit results with similar χ^2 values: one with the pole near the real axis labeled 3C-R (resonant) and one without a nearby pole labeled 3C-NR (nonresonant). The fits to the GlueX cross section can be seen in figure 1.15. We see good agreement in the 1C fits, except around the dip at 9.1 GeV where, according to the JPAC calculations, the data points lie at least 2σ away from the 1C fit results. The 2C fit shows a cusp feature similar to that found by Du *et al.*, which qualitatively fits the data better. However, JPAC found that the significance was not high enough to prefer 2C over the 1C curve. The 3C fits have the most structure, with the 3C-NR curve qualitatively matching the best with the GlueX data but still differing in the lineshape of the cusp-dip structure in the data.

JPAC also looked at these 4 models and their effect on the differential cross section, with fits to the GlueX data found in figure 1.16. The 1C model predict a stark increase in the differential cross section at high- t in the lowest beam energy bin, while the 2C and 3C curves show a flattening

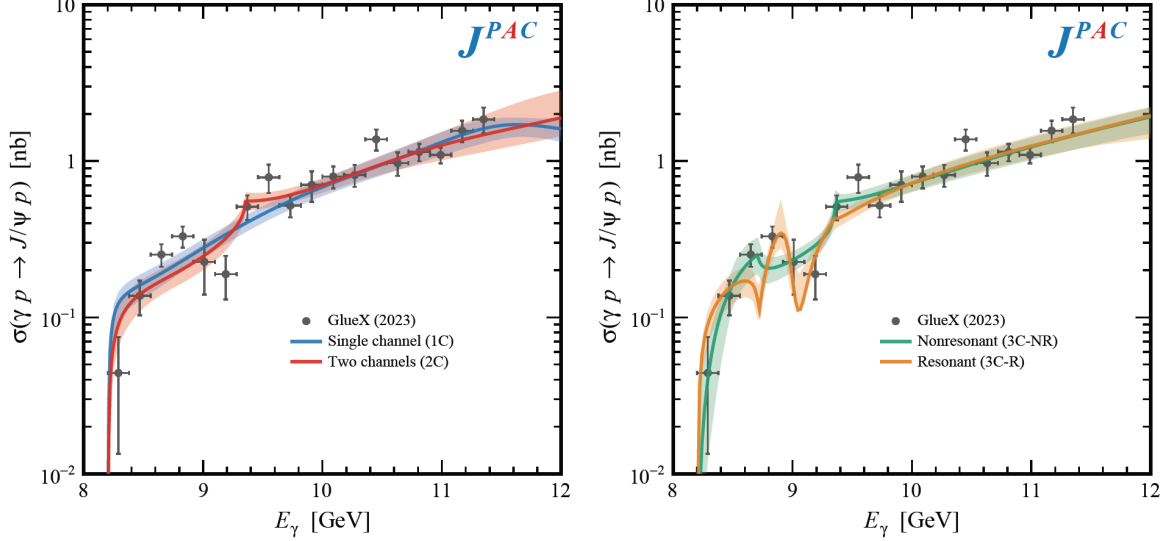


Figure 1.15: Fit results by JPAC [45] of the integrated cross section of all four models compared to GlueX data from [33]. Bands correspond to 1σ uncertainties from bootstrap analysis.

at high- t . However, all curves describe, within uncertainties, the available data by GlueX. JPAC concludes that the current data cannot exclude the presence of these open-charm exchange models. To better distinguish between the models, more data and better precision are needed, specifically in the high- t region.

1.5.3 Pentaquarks

The last broad category of models that could contribute to J/ψ photoproduction are s-channel models through the production of hidden-charm pentaquarks in the $J/\psi p$ spectrum, shown in figure 1.18. The discovery of pentaquarks in the $J/\psi p$ spectrum by LHCb [41, 42, 43] in 2019 led to great interest in charmonium photoproduction both experimentally and theoretically. LHCb found three peaks, two within the narrow $P_c^+(4450)$ and a new one $P_c^+(4312)$, which can be seen in Figure 1.17. These three states ($P_c^+(4440)$, $P_c^+(4457)$, and $P_c^+(4312)$) did not fit into the standard quark model, and their decay to $J/\psi p$ suggests a quark content of $c\bar{c}uud$ [41, 42, 43]. Soon after these states were found, many theorists suggested that the photoproduction at GlueX could observe these states with large cross sections, through the reaction $\gamma p \rightarrow P_c^+ \rightarrow J/\psi p$ [46, 47, 48, 49]. The pentaquarks would then be seen as structures in the J/ψ photoproduction cross section. JPAC [49] looked at the effect of the $P_c(4450)$ resonance, using the fitting parameters from the LHCb results, on the total J/ψ photoproduction cross section for the two possible spin assignments (3/2 and 5/2) and

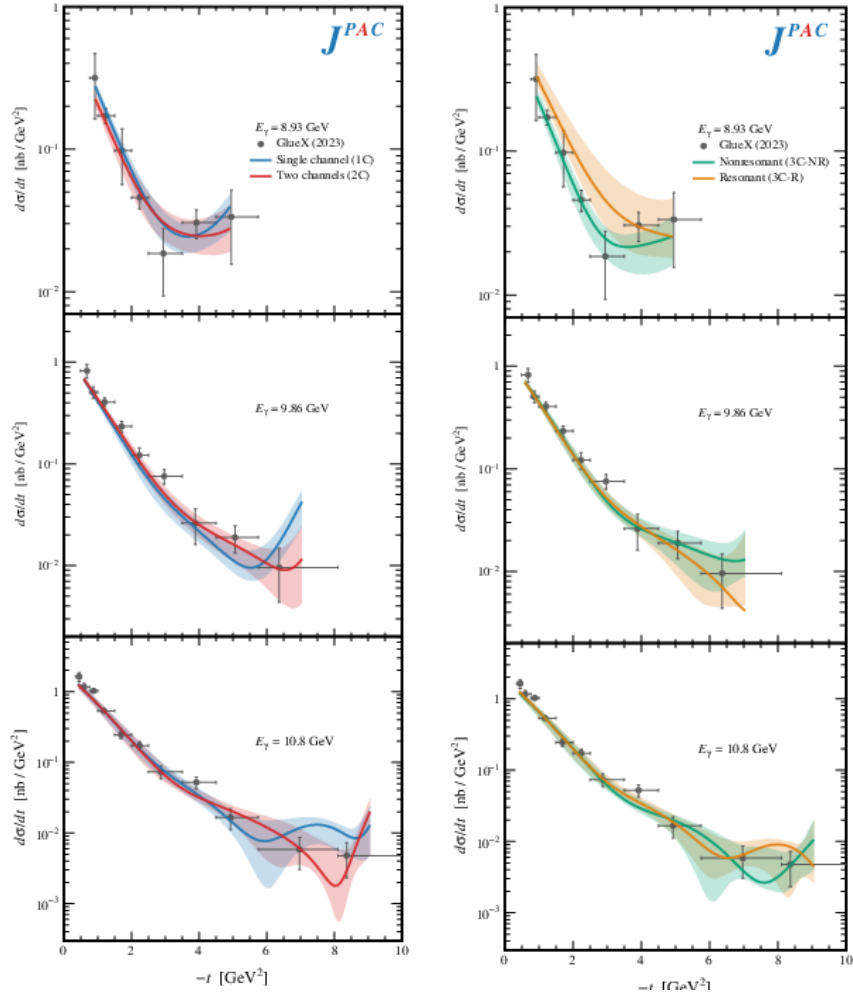


Figure 1.16: Fit results by JPAC [45] of the differential cross section of all four models compared to GlueX data from [33]. Bands correspond to 1σ uncertainties from bootstrap analysis.

different experimental resolutions, shown in figure 1.19. Considering the J/ψ photoproduction total cross section is approximately 1 nb at 10 GeV beam energy, there results show a significant bump in the cross section, even with poor experimental resolution.

In 2023, Strakovsky *et al.* [50] looked at the effect of the $P_c(4450)$ resonance by fitting it to the updated GlueX data. Unlike the JPAC interpretation, where they assume the resonant and non-resonant background would interfere constructively, Strakovsky *et al.* looked at the possibility of destructive interference. Their results are shown in figure 1.20. They conclude that the pentaquark resonance could contribute to this dip feature in the total cross section, but contributions from the open charm exchange mechanism could make this more complicated than just a resonance plus a

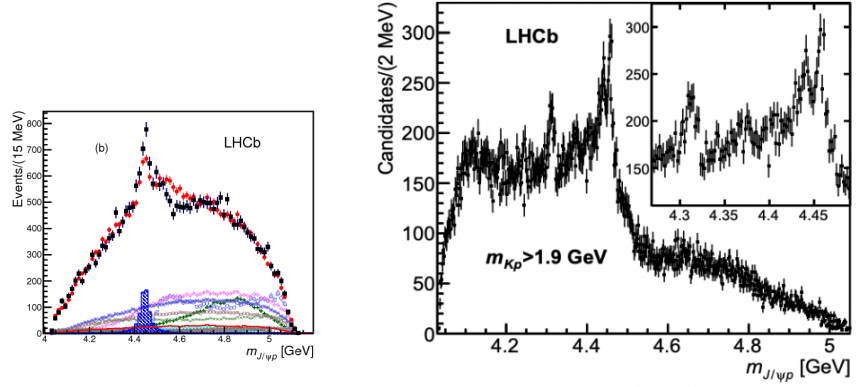


Figure 1.17: (Left) Distribution of $m(J\psi p)$ for $\Lambda_0^b \rightarrow J/\psi p K^-$ candidates. (Right) Same distribution but with removal of dominant background. The inset shows a zoom into the region of the narrow P_c^+ peaks. [43]

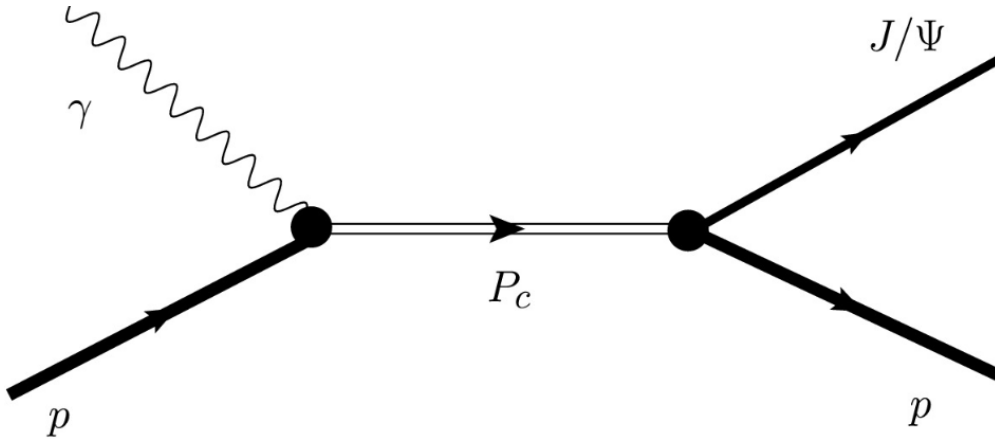


Figure 1.18: Model of pentaquarks produced in the s -channel of J/ψ photoproduction.

background, such as that shown in figure 1.20.

1.5.4 J/ψ and The GlueX Experiment

This dissertation enhances the theoretical understanding of J/ψ photoproduction, particularly near the threshold, by contributing new data to the existing measurements and allow for a more comprehensive analysis of theoretical models. Building on previous experimental results briefly referenced earlier and discussed in detail in Chapter 2, this work’s cross-section measurements provides critical data to test predictions from gluonic exchange models, open-charm exchange models, and potential contributions from exotic states such as pentaquarks. By comparing these experimental

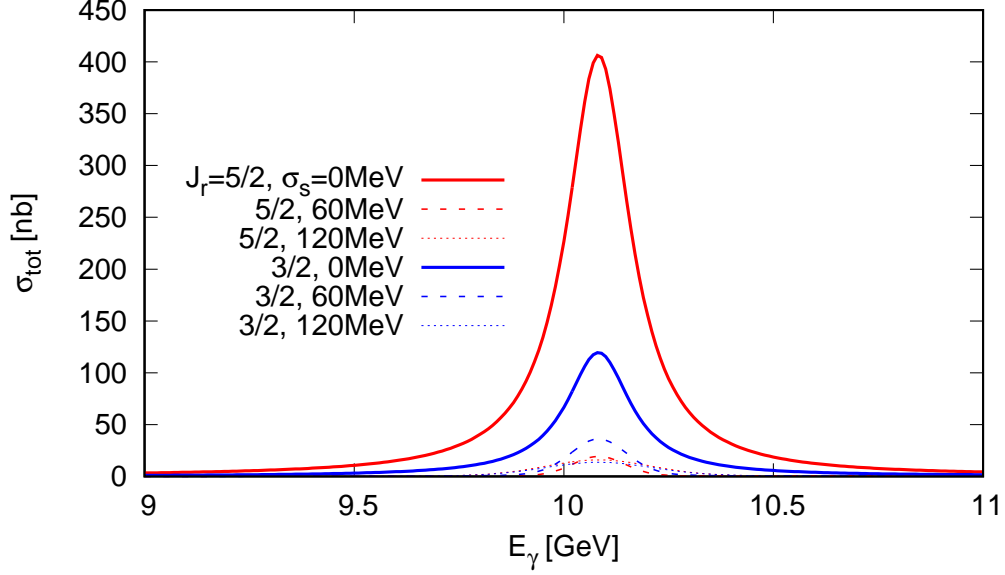


Figure 1.19: JPAC prediction of the expected total J/ψ photoproduction cross section in the $P_c(4450)$ resonance region, as a function of the lab-frame photon energy E_γ [49].

findings with previous results and exploring cross-section deviations, this study informs ongoing theoretical efforts to model strong interactions within the proton.

The following chapters will elaborate on the background and methodology behind this research. Chapter 2 reviews prior experimental data relevant to J/ψ photoproduction close to threshold, highlighting this work's context and its additions to the field. Chapter 3 details the GlueX experimental setup and detection techniques utilized to identify J/ψ events. Chapter 4 covers the data analysis procedures, including event selection and cross-section calculation, while Chapter 5 interprets the experimental findings' implications for theoretical models and suggests directions for future research.

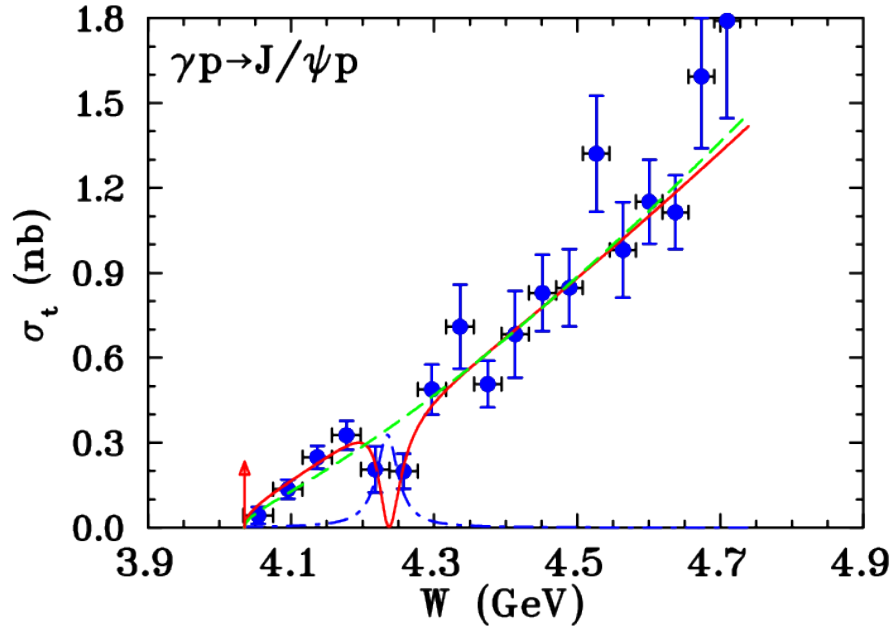


Figure 1.20: Strakovsky *et al.* [50] results for new GlueX total cross sections for the reaction $\gamma p \rightarrow J/\psi p$ (blue filled circles) [34]. The vertical error bars represent the total uncertainties (statistical and point-to-point systematic uncertainties in quadrature). The horizontal error bars reflect the energy binning (not used in the fit). The best-fit result, shown by red solid curve, include non-resonant background plus $P_c(4450)$ resonance with destructive interference. Green dashed curve corresponds to the non-resonant fit as a function of q . Blue dash-dotted curve corresponds to the S-wave resonance. The red vertical arrow indicates the J/ψ production threshold.

CHAPTER 2

PREVIOUS MEASUREMENTS

In this chapter, we review the previous measurements of J/ψ photoproduction near threshold. Section 2.1 reviews the first J/ψ photoproduction measurements near threshold performed in 1975 by Camerini *et al.* [30] at SLAC, while Section 2.2 reviews the results of Gittelman *et al.* [31] made in 1975 at Cornell University. Section 2.3 reviews the work done by our collaboration, GlueX, on J/ψ photoproduction near threshold through the decay of $J/\psi \rightarrow e^+e^-$. Lastly, section 2.4 reviews the most recent findings of J/ψ photoproduction near threshold published by Duran *et al.* using a different Jefferson Lab experiment, $J/\psi - 007$, in Hall C [44].

2.1 SLAC

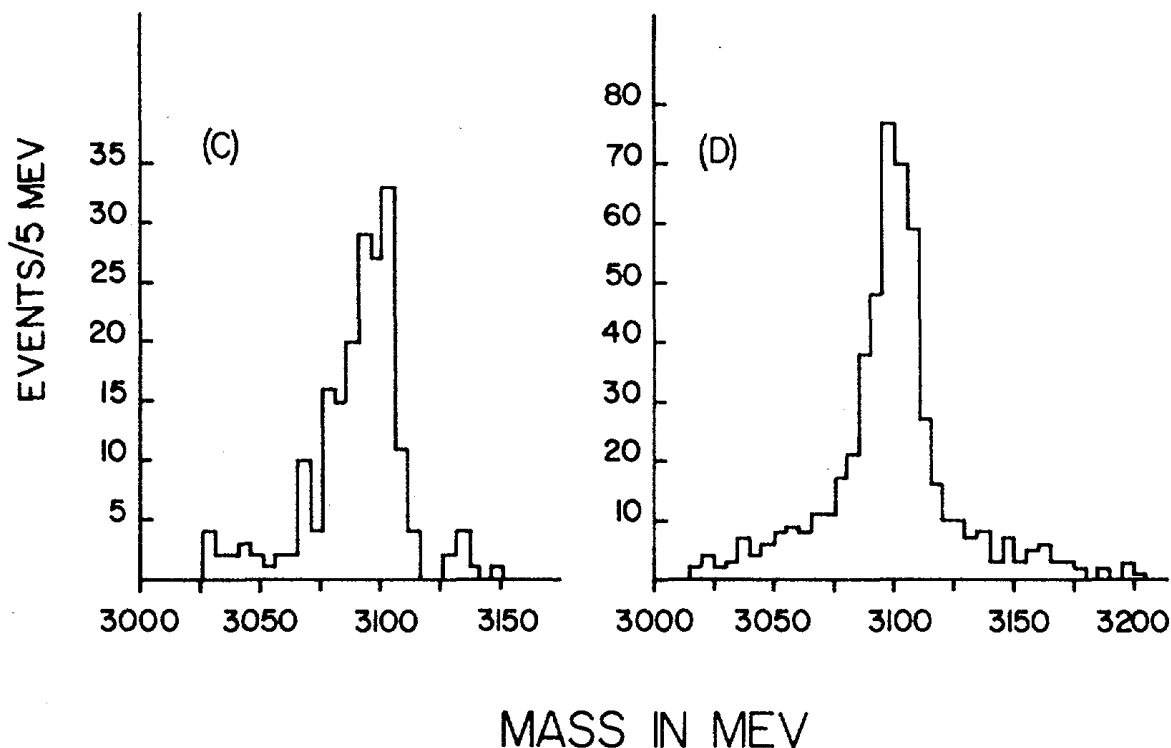


Figure 2.1: (Left) Camerini *et al.* measurement of the invariant mass spectrum of electron-positron pairs at SLAC. (Right) Their measured invariant mass spectrum of muon pairs [30].

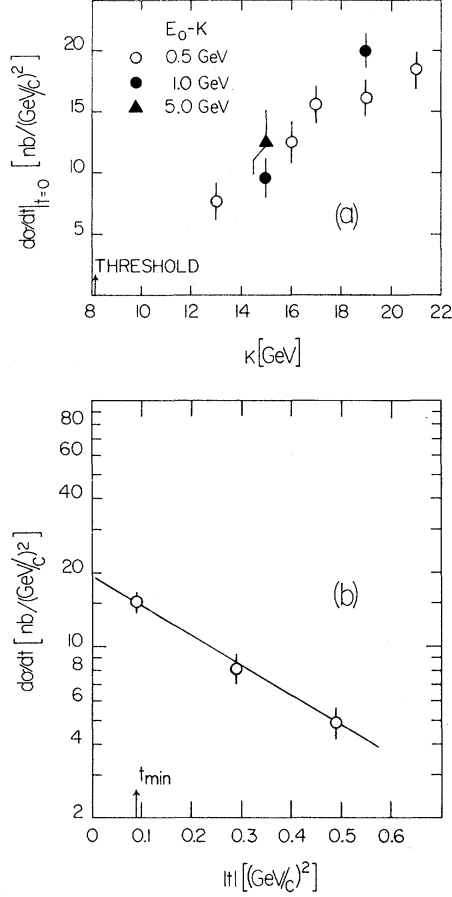


Figure 2.2: (Top) Camerini *et al.* cross section extrapolated to $t=0$ for J/ψ as a function of beam energy. (Bottom) Camerini *et al.* differential cross section as a function of t for J/ψ at $E_{beam} = 19$ GeV. The estimated t -slope is $b = 2.9 (\text{c}/\text{GeV})^2$ [30]

The Camerini *et al.* measurements were published in June 1975 [30]. They had a bremsstrahlung photon beam incident on a liquid deuterium (majority of runs) or liquid hydrogen target, with beam energies between 13.0 GeV and 21 GeV. Two spectrometer arms were used to detect electron and muon pairs from the J/ψ decay, which used a gas Cherenkov counter and lead glass calorimeter to detect e^\pm and iron scintillation counters to detect muons. The invariant mass distributions of the e^+e^- and $\mu^+\mu^-$ pairs measured can be seen in Figure 2.1. Measurements of the differential cross section were also taken as a function of beam energy and Mandelstam- t variable, shown in Figure 2.2. Camerini *et al.* found an estimated t -slope of $b = 2.9 (\text{c}/\text{GeV})^2$, shown in the bottom plot of Figure 2.2. Since Camerini *et al.* were unable to measure the recoiling proton, they used the location of the spectrometer arms to determine the Mandelstam- t values. Because of this limited

range of Mandelstam- t values they had access to, Camerini *et al.* was only able to measure a few bins in the differential cross section.

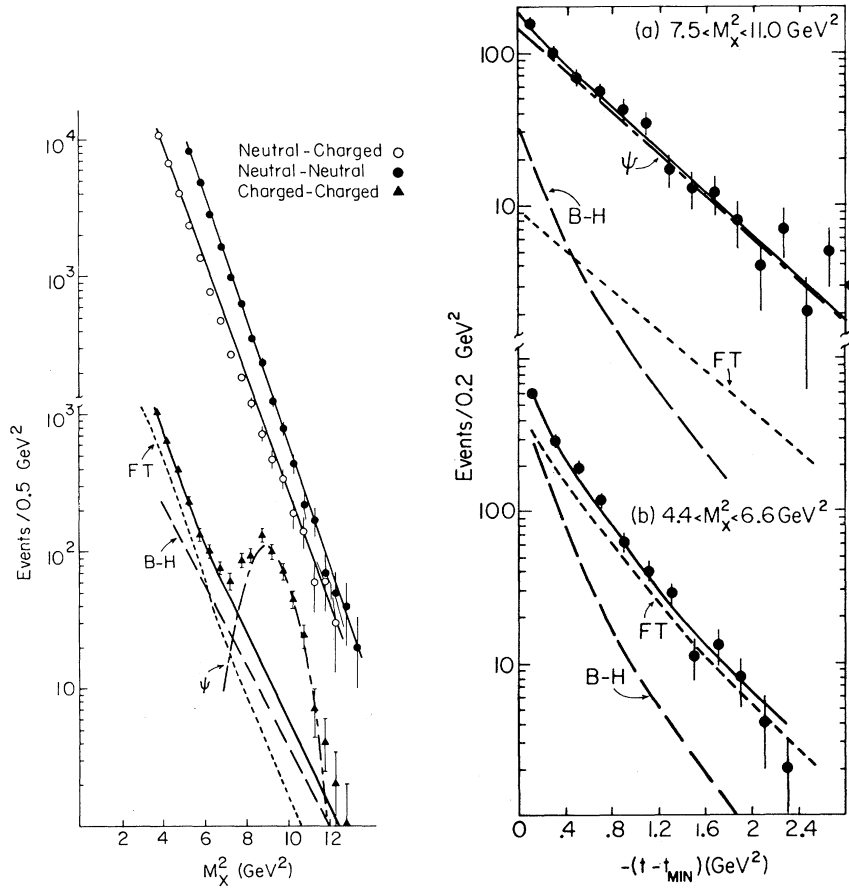


Figure 2.3: (Left) Gittelman *et al.* measured two-particle invariant mass squared spectrum. The triangular points are of two charged particles, presumably e^+e^- and $\mu^+\mu^-$ pairs. The solid line through the triangular points is background associated with Bethe-Heitler (B-H) pairs, and the finely dashed line is background from neutral-charge and neutral-neutral particle feedthrough (FT). (Right) Gittelman *et al.* differential cross section as a function of $t' = t - t_{min}$ at $E_{beam} = 11$ GeV. The top plot is in the J/ψ mass region with an estimated t -slope, $b = 1.2$ (c/GeV^2)², while the bottom plot shows the background t distribution below the J/ψ mass [31].

2.2 Cornell

Two months after the Camerini *et al.* measurements were published, Gittelman *et al.* published their results in August of 1975 [31]. Like the Camerini *et al.* measurement, Gittelman *et al.* also had a bremsstrahlung photon beam incident on a target; however, the Gittelman *et al.* measurement used a Beryllium target, which was sandwiched between a pair of lead glass Cherenkov hodoscopes

and had beam energies between 9.0 GeV and 11.8 GeV. Gittelman *et al.* two-particle M^2 distribution can be seen in the right plot of Figure 2.3, where they classify the particle by either being charged (e^\pm) or neutral (photons) based on energy deposition in the hodoscopes. In the neutral-neutral and neutral-charged cases, no peaking structure appears around 9 GeV². However, in the charged-charged case, there is a peak at around 9 GeV² that aligns well with the J/ψ mass of 3.1 GeV. After subtracting the background, which was determined to come from Bethe-Heitler production of e^+e^- pairs and identification of photons as charged particles, Gittelman *et al.* found 542 J/ψ events, about half of what was found in the Camerini *et al.* measurement. Gittelman *et al.* were also able to measure the differential cross section as a function of $t' = t - t_{min}$ at $E_{beam} = 9.3 - 11.8$ GeV, shown in the right plot of Figure 2.3. Gittelman *et al.* found an estimated t slope of $b = 1.2$ (c/GeV)², represented by the solid line in the top plot. Just like the Camerini *et al.* measurement, Gittelman *et al.* were also not able to measure the recoiling proton. Instead, to measure Mandelstam- t , Gittelman *et al.* used the lead glass Cherenkov hodoscopes to determine the ϕ and θ angles of the particle pairs. Combining this information with the beam energy, they can calculate the Mandelstam- t for each J/ψ event. Because of this, Gittelman *et al.* were limited in Mandelstam- t by the angular coverage of their hodoscopes.

2.3 GlueX Collaboration

2.3.1 Initial $J/\psi \rightarrow e^+e^-$ Publication

In August 2019, the GlueX Collaboration published its first results on the exclusive measurement of the $\gamma p \rightarrow J/\psi p$ cross section through the decay of $J/\psi \rightarrow e^+e^-$. A description of the experimental setup can be found in Section 3, with a more detailed description found in Ref. [51]. In this first publication, only data taken in 2016 and 2017 was used. The plot on the left of figure 2.4 shows the measured $M(e^+e^-)$ spectrum. We see a narrow peak at about 3.1 GeV, which is consistent with what we would expect for the mass of the J/ψ particle. We also observed a narrow ϕ peak at approximately 1 GeV.

This analysis is the first measurement of the J/ψ exclusive photoproduction cross section from threshold to 11.8 GeV [33]. The cross section measurement performed in this analysis was a relative cross section to the Bethe-Heitler (BH) process, which is the dominant production mechanism of e^+e^- pairs at lower masses. This is done using the following formula:

$$\sigma_{J/\psi}(E_\gamma) = \frac{N_{J/\psi}(E_\gamma)}{N_{BH}(E_\gamma)} \frac{\sigma_{BH}(E_\gamma)}{B_{J/\psi}} \frac{\epsilon_{BH}(E_\gamma)}{\epsilon_{J/\psi}(E_\gamma)}. \quad (2.1)$$

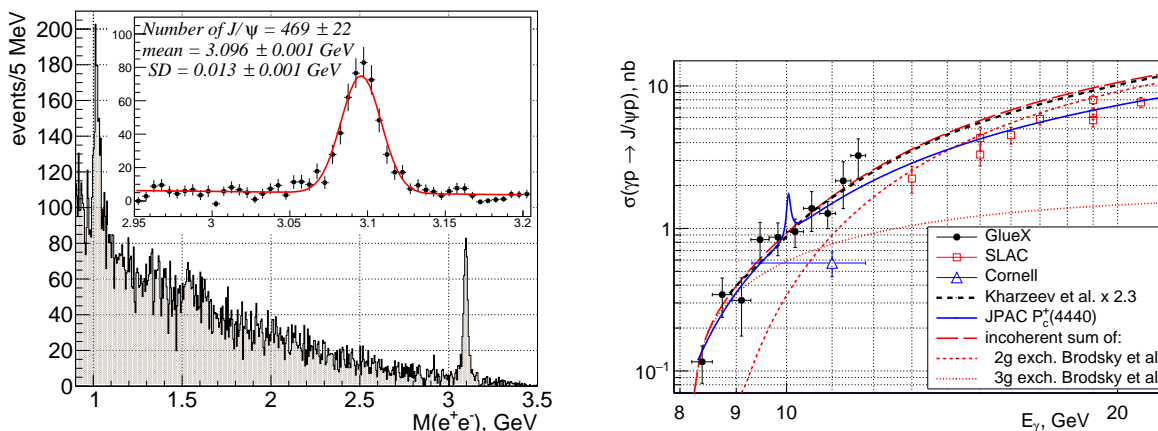


Figure 2.4: (Left) The measured invariant mass spectrum of electron-positron pairs by GlueX. (Right) The total cross-section versus beam energy measured at GlueX compared to the previous data (Camerini *et al.* [30] and Gittelmann *et al.* [31]), theoretical predictions (Kharzeev [28] and Brodsky [29]), and the JPAC model [52].

In this equation, $N_{J/\psi}$ and N_{BH} are the J/ψ and BH yields, σ_{BH} is the calculated BH cross section, $B_{J/\psi}$ is the branching ratio of $J/\psi \rightarrow e^+e^-$ taken from the PDG [1], and the last term is the relative BH to J/ψ efficiency. The yields come from fits to the mass spectrum, and because of the deep understanding of the BH process, the BH cross section is calculated with high precision. The relative BH to the J/ψ efficiency is determined from simulations, since the two processes occupy different kinematic regions. Doing this allows for cancellation of uncertainties due to factors such as luminosity and e^\pm detection efficiencies. However, it also leads to the largest relative uncertainty in the total cross section, $23 \pm 18\%$ of the total normalization uncertainty of 27%. The initial results from GlueX on this relative cross section are shown in the right plot of Figure 2.4, from which several important results can be seen. First, the cross sections are larger and rise slower than suggested by the SLAC and Cornell measurements, but as stated before, these previous measurements were limited in statistics and had large uncertainties [30][31]. We also see that using the model mentioned in chapter 1 from Kharzeev *et al.* [28], it suggests that there is a large gluonic contribution to the proton mass. Using the model by Brodsky *et al.* [29], the cross sections favor some combination of both two and three-hard gluon exchange. Lastly, we see no evidence for any of the P_c^+ states that were found in the LHCb published results [41]. The JPAC model [52] shown in figure 2.4 provides the shape that our cross section would form if this state $P_c^+(4440)$ were to be found. By comparing the model to the cross section results, it is clear that there is no visible peaking structure

at ≈ 10 GeV.

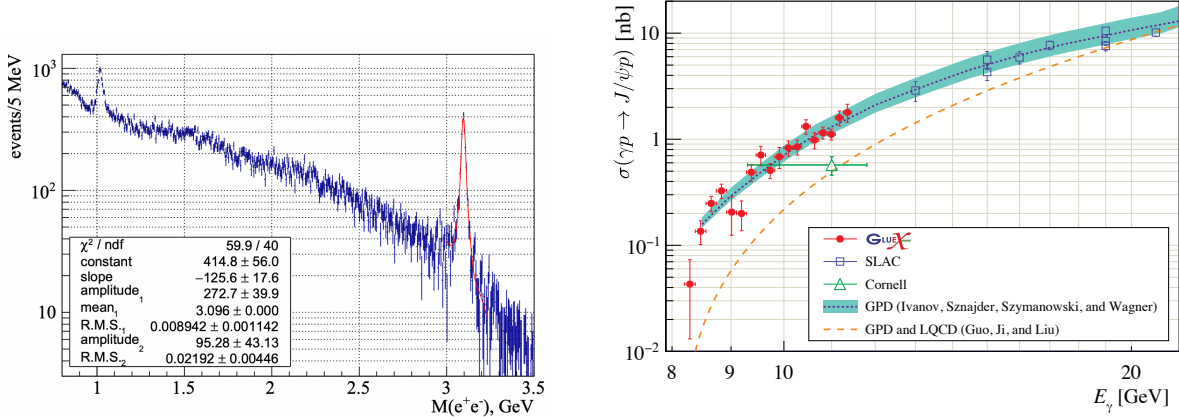


Figure 2.5: (Left) The updated GlueX measured invariant mass spectrum of electron-positron pairs, fit with 2 Gaussian’s and a linear background. Found 2270 ± 58 J/ψ events [34]. (Right) The updated total cross section versus beam energy measured at GlueX compared to the previous data (SLAC [30] and Cornell [31]) and two theoretical QCD calculations in the two-gluon exchange factorization model from Ref. [34] and from Ref. [38]. The latter calculation uses gravitational form factors from lattice calculations from Ref [53].

2.3.2 Updated GlueX Results

After the publication in 2019, the hadronic community took great interest in the results, with more than 200 citations as of August 2024. In 2023, GlueX published an update of the total cross section, using the same method as the original publication, as well as differential cross sections in both beam energy and Mandelstam-t [34]. In this update there was an increase of five times that published in 2019. The updated mass spectrum and total cross section results can be seen in figure 2.5. In this update, GlueX measured 2270 ± 58 J/ψ events, a significant increase from the 469 ± 22 J/ψ events found in the original publication.

From the total and differential cross sections, a few important results can be found. First, the total cross section, which is shown in the right plot of Figure 2.5, still shows no evidence for any of the P_c^+ states found in the published results of LHCb [?], even with the greater statistics. We also see in the total cross section a potential dip structure between 8.8 GeV and 9.4 GeV. The dip was found to have a significance of 2.6σ . This dip is quite interesting because it lies right at the thresholds for open-charm channels, $\Lambda_c \bar{D}$ (8.71 GeV) and $\Lambda_c \bar{D}^*$ (9.35 GeV), which could produce cusp-like features shown in Figure 2.6. In the differential cross section, shown in Figure 2.7, we see

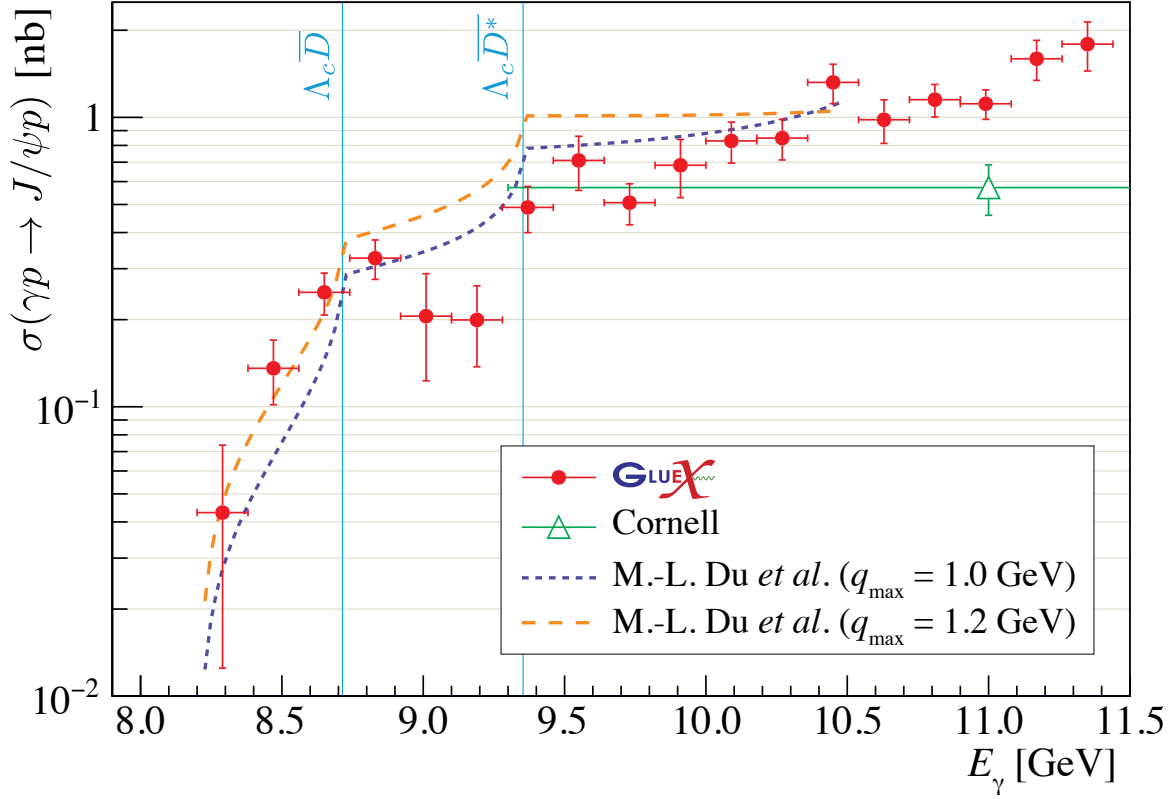


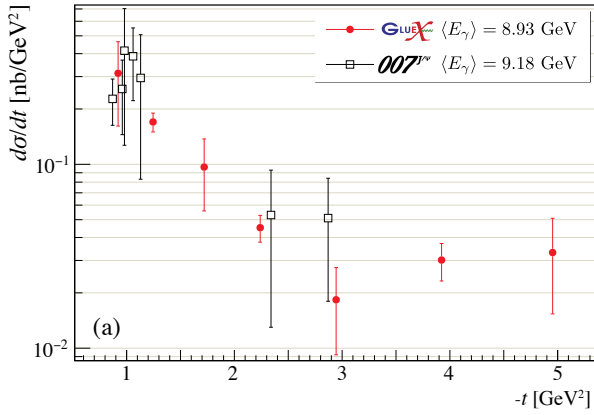
Figure 2.6: The updated total cross section versus beam energy measured at GlueX compared to the Cornell [31] results and two open-charm calculations from Ref. [40]. The vertical lines are the thresholds for open-charm channels, $\Lambda_c \bar{D}$ (8.71 GeV) and $\Lambda_c \bar{D}^*$ (9.35 GeV).

a flattening at high Mandelstam- t in the lowest beam energy bin, closest to the threshold. With a significance of 2.3σ deviation compared to a dipole fit of the differential cross section, this feature can be interpreted as a contribution of the s - or u -channels to the cross section, as mentioned in chapter 1. If these open-charm exchanges mentioned before are contributing to the cross section, this would be consistent with the flattening at high- t that we see in the differential cross section.

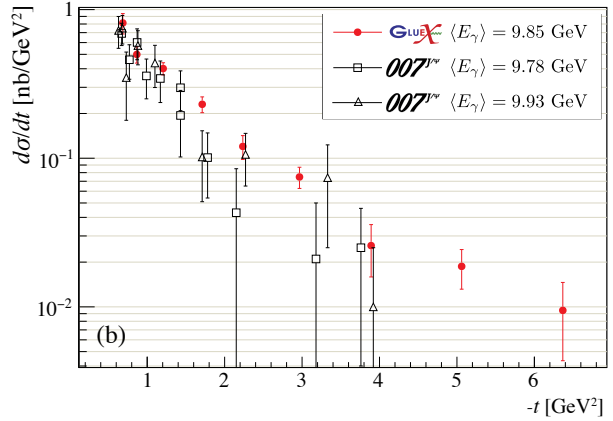
2.4 J/ψ -007 Experiment

Right before the update by GlueX, Duran *et al.* published their findings of J/ψ photoproduction near threshold using a different Jefferson Lab experiment, J/ψ –007, in Hall C [44]. The J/ψ –007 experiment produced a bremsstrahlung photon beam from the CEBAF 10.6 GeV electron beam,

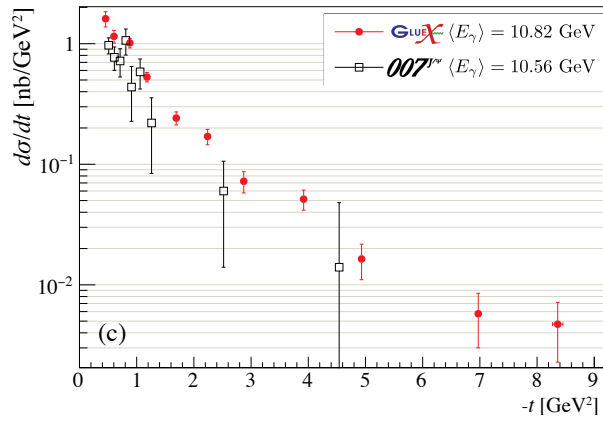
similar to that of the GlueX experiment. The photon beam, together with the electron beam, is passed through a liquid hydrogen target, and the J/ψ events are detected by two high-momentum spectrometer arms through the decay of $J/\psi \rightarrow e^+e^-$. Each spectrometer, shown in Figure 2.8, consists of identical drift chambers for tracking charged particles, a pair of XY-plane hodoscopes for triggering, and a threshold Cherenkov counter and an electromagnetic calorimeter to separate electrons and positrons from muons and pions. Like the Camerini *et al.* measurement, Duran *et al.* were also not able to measure the recoiling proton and used the positioning of the spectrometer arms to determine the Mandelstam- t of each event. This limits their kinematic range to that available of the positioning of the spectrometer arms. Duran *et al.* report a differential cross section measurement in 10 bins of beam energy, shown in Figure 2.9, with an overall 4% scale uncertainty. Using some of the models discussed in chapter 1, they compare their results to what these models predict with fixed parameters determined from the GlueX results, which are the curves in Figure 2.9. After comparing these results to our updated GlueX analysis in Figure 2.7, we see that these measurements align with the updated GlueX $J/\psi \rightarrow e^+e^-$ analysis, especially considering the 20% scale uncertainty in the GlueX results.



(a) GlueX measurements at $8.2 \text{ GeV} < E_\gamma < 9.28 \text{ GeV}$



(b) GlueX measurements at $9.28 \text{ GeV} < E_\gamma < 10.36 \text{ GeV}$



(c) GlueX measurements at $10.36 \text{ GeV} < E_\gamma < 11.44 \text{ GeV}$

Figure 2.7: Comparison of the GlueX differential cross sections [34] for the three energy slices to the closest in energy measurements done by Duran *et al.* [44]

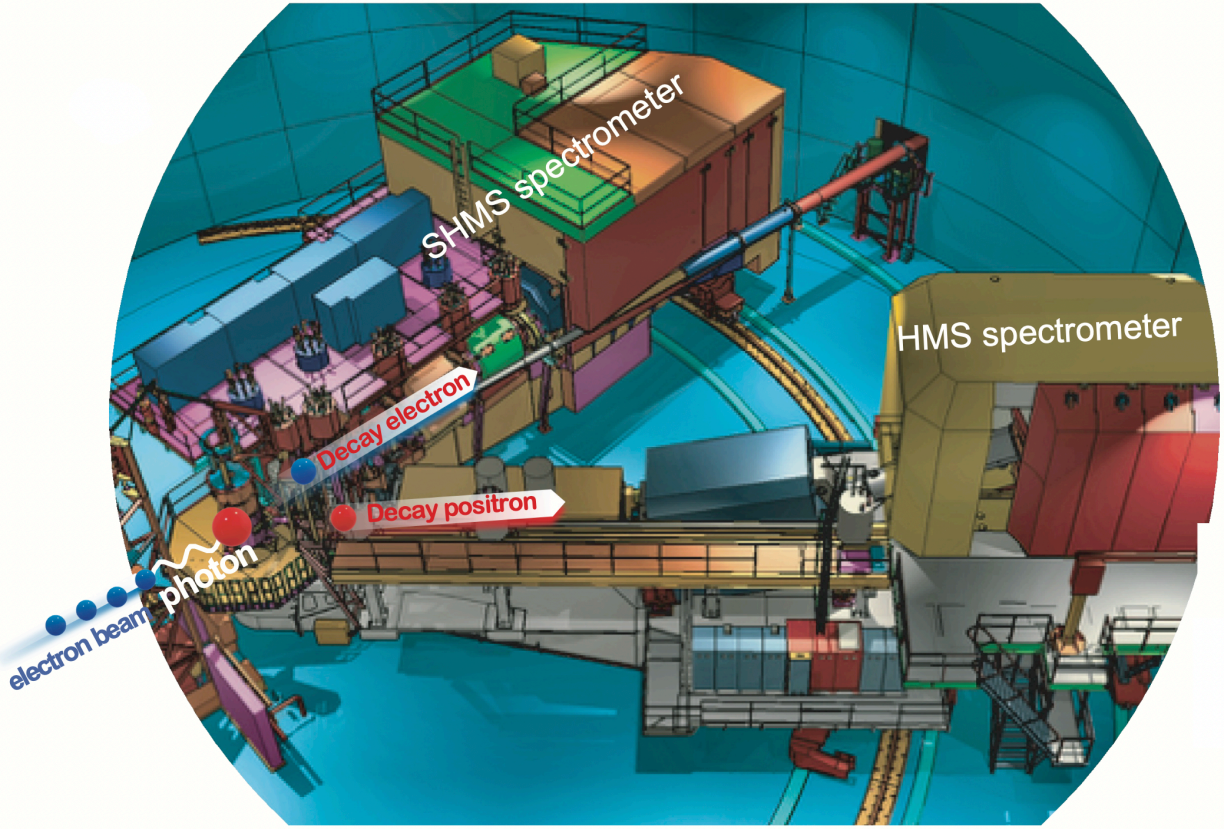


Figure 2.8: Layout of the J/ψ -007 experiment in Hall C [44].

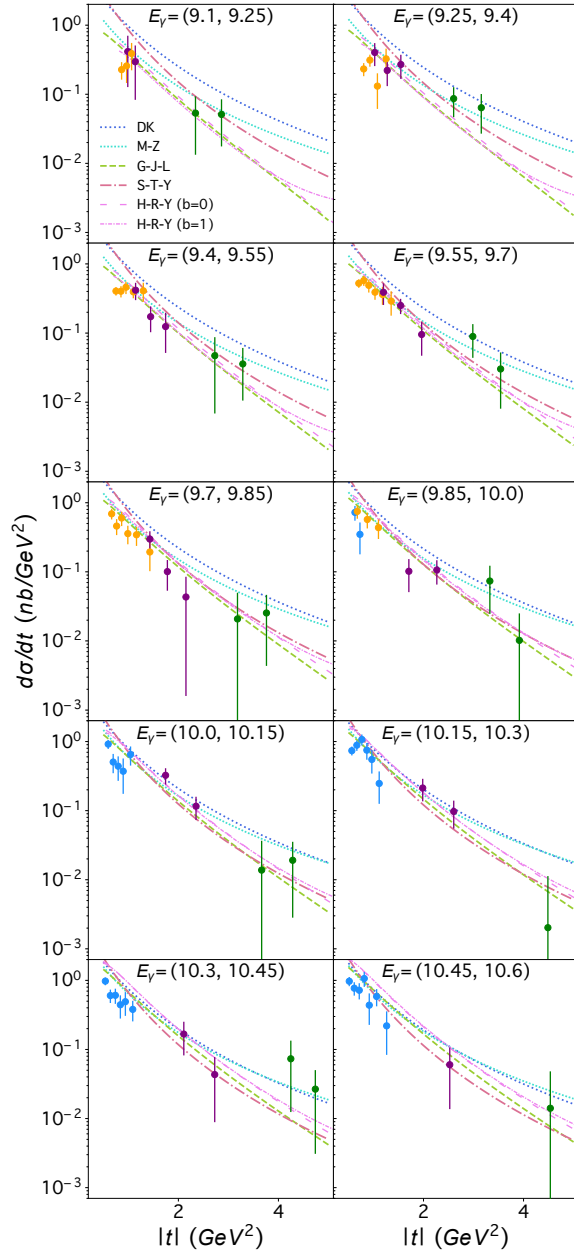


Figure 2.9: Duran *et al.* differential cross sections versus t in 10 different beam energy bins. Every curve is a prediction with fixed parameters determined from the GlueX results. The blue dotted line (labeled DK) uses parameters from Ref. [32], the cyan dotted line (labeled M-Z) is the holographic QCD approach [54], the green dashed line (labeled G-J-L) is the GPD approach [38], the red-dash-dotted line is a higher twist approach (labeled S-T-Y) [39], and finally the purple dash (purple dash-dot) labeled H-R-Y is another holographic calculation [55] with maximal (minimal) trace anomaly contribution to the EMT matrix element [44].

CHAPTER 3

THE GLUEX EXPERIMENT

The GlueX experiment is located in Hall D of Thomas Jefferson National Accelerator Facility (JLab). An electron beam is produced by the Continuous Electron Beam Accelerator Facility (CEBAF). This electron beam is used to produce a tagged, linearly polarized photon beam that is then incident on a liquid hydrogen (LH_2) target. The target is surrounded by a nearly 4π hermetic detector that is used to measure both charged particles and photons. In the chapter, we discuss the experimental setup, from how the electron beam is produced and accelerated to the reconstruction of the wide array of particles in the GlueX detector. For the most complete description of the beamline and detector instrumentation, please refer to Ref. [51].

3.1 The Photon Beam

CEBAF, housed at JLAB, is a race-track shaped accelerator with two linear accelerators (called the North and South Linac) connected by two arcs, which can be seen in Figure 3.1. Bunches of electrons are produced by shining a laser incident on a gallium-arsenide wafer. Using magnets, the electron bunches are directed into the North Linac, where they are accelerated and focused using Radio Frequency (RF) cavities). Halls A, B, and C receive electrons that have passed through each Linac five times before the electrons are redirected to the halls. The GlueX experiment, located in Hall D, receives electrons that gain another pass through the North Linac before being redirected into the Hall. The energy of these electrons can reach up to 12 GeV and can be supplied to all halls simultaneously.

Produced in 4 ns intervals, the electron beam bunches reach Hall D, where they pass through a radiator to produce the photon beam via bremsstrahlung radiation. The setup can be seen in Figure 3.2. Two types of radiator are used: a diamond radiator, which produced a linearly polarized photon beam, and an aluminum radiator, which produces an unpolarized photon beam. The two combined beams of electrons and photons pass through a dipole magnet, causing the trajectory of the electrons to bend into the tagger detector. Based on the bending angle and initial energy of the electron beam provided by CEBAF, we can determine the energy of the outgoing photon

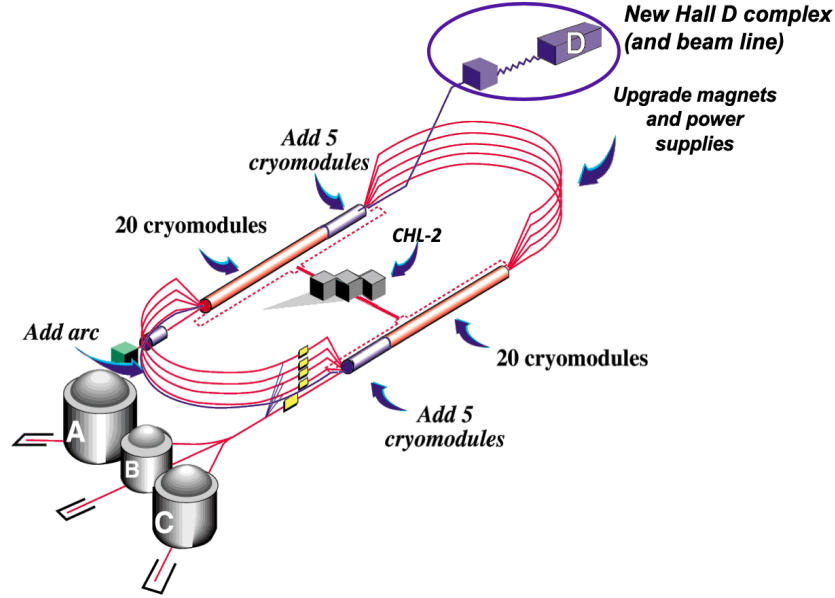


Figure 3.1: Schematic of CEBAF and the four halls housed at JLab [51].

beam. This photon beam travels a distance of 75m before a collimator focuses the beam. The photon beam then passes through the Triplet Polarimeter (TPOL) and Pair Spectrometer (PS), which provide us the photon beam’s degree of polarization and its flux. The photon beam then finally reaches the LH_2 target, where it either produces a reaction or continues until it reaches the beam dump.

3.1.1 Producing a Tagged Photon Beam

When higher energy electrons pass through a diamond crystal radiator, a linearly polarized photon beam is produced through a process called coherent bremsstrahlung radiation. The orientation of the diamond radiator controls the angle between the floor and the linear polarization of the photon beam. Because of this, we collect data in four different orientations of the 20–60 μm thick diamond radiator: 0° , 45° , 90° and 135° (or -45°). To understand the systematic effects of using a polarized photon beam, we use an aluminum radiator to produce an unpolarized photon beam via incoherent bremsstrahlung radiation. Aluminum radiators range in thickness from 1.5 to 40 μm .

Once the electron beam passes through the radiator, the combined photon and electron beams enter a dipole magnet. This causes the trajectory of the electron beam to bend into either the Tagger Hodoscope (TAGH), the Tagger Microscope (TAGM), or the electron beam dump. As seen

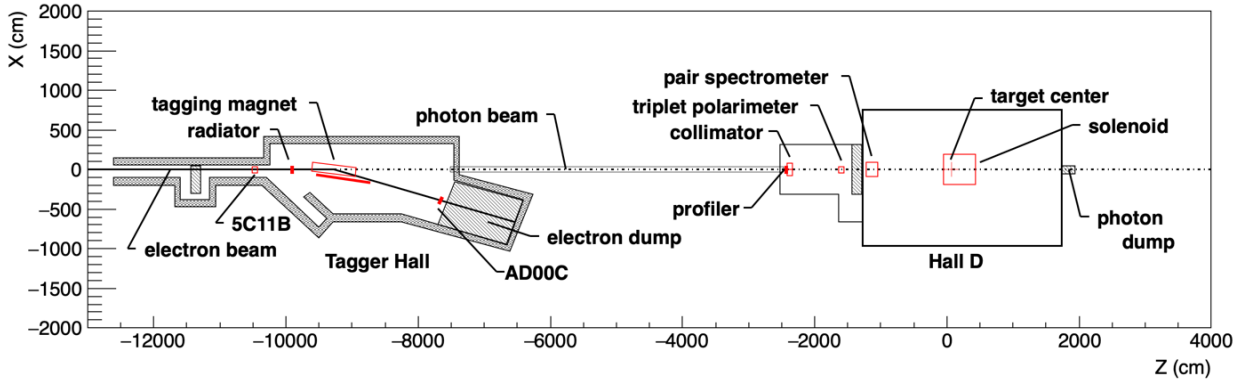


Figure 3.2: Schematic of the Hall D photon production beamline [51].

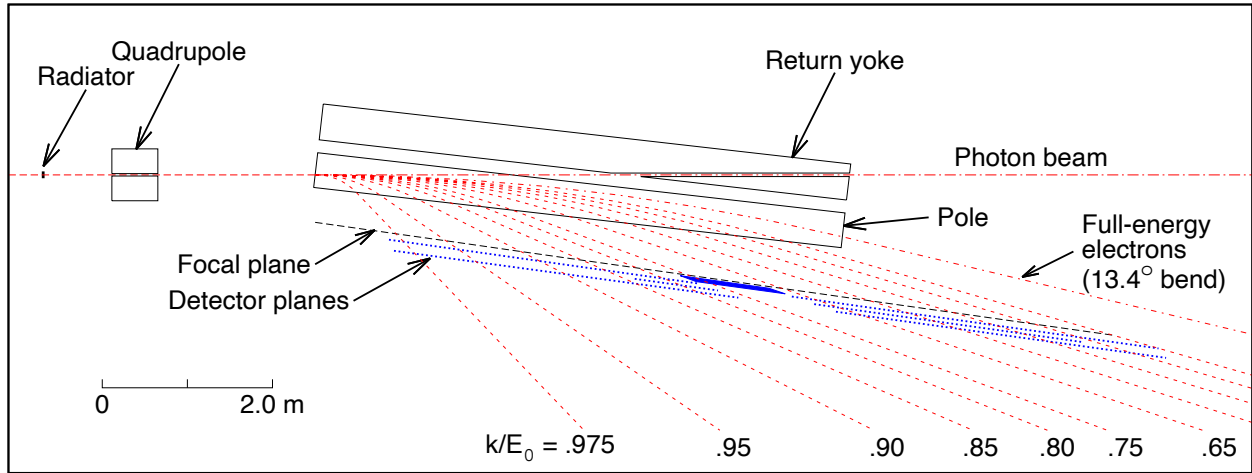


Figure 3.3: Schematic of the tagger system [51].

in Figure 3.3, the more energy that is lost by the electron (and consequently put into the photon), the larger the angle of curvature by the dipole magnet. Using this and the initial energy of the electron beam provided by CEBAF, we can determine the photon beams energy. We determine the angle of curvature through our tagger system, which is divided into two components: TAGH and TAGM. Both taggers are arrays of scintillators, but they differ in resolution and coverage area. Covering a narrow energy range, the TAGM is a high-resolution hodoscope, indicated by the dense portion of the focal plane in Figure 3.3. This narrow range corresponds to the *coherent peak*, where the flux and degree of polarization are the highest, as seen in Figure 3.4. This optimization in the coherent peak is primarily for other GlueX analysis, where the highest degree of polarization is of great interest. The microscope is segmented into 102 energy bins (columns) of equal width, with each bin segmented into 5 rows. Each segment is a scintillating fiber with a square transverse profile of dimensions $2 \times 2 \text{ mm}^2$ and 10 mm long. The TAGH covers a much larger energy range of about 25% to 97% of the electron beam energy, which corresponds to approximately 3 GeV to 12 GeV, excluding the range covered by the TAGM. It consists of 222 scintillator counters, covering 9.25m across the focal plane. This is much larger than the 0.2m that is covered by the TAGM, but with $\approx 40 \text{ MeV}$ precision on the beam energy compared to $\approx 8 \text{ MeV}$ of the TAGM.

3.1.2 Beam Polarization and Flux

Collimating the beam. When the photon beam is produced, it is a mixture of coherent and incoherent bremsstrahlung radiation. In the coherent peak (8.2–8.8 GeV), the angular spread of incoherent bremsstrahlung photons is greater than that of coherent bremsstrahlung photons. Therefore, by collimating the beam before it enters the hall, we can block a large portion of the unpolarized photons from reaching the target. The collimator, with a 5 mm diameter aperture, increases our overall polarization fraction of the beam entering the hall.

Measuring photon polarization. To measure the photon beams polarization, we use the TPOL and PS to measure the triplet photoproduction ($\gamma e^- \rightarrow e^- e^+ e^-$) off a beryllium foil. When a photon interacts with the electric field of a beryllium atom (specifically its valence electron), a high-energy e^+e^- pair is produced. The cross section for polarized triplet photoproduction is described by the equation

$$\sigma_{triplet} = \sigma_0[1 - P\Sigma\cos(2\phi)] \quad (3.1)$$

where σ_0 is the unpolarized triplet cross section, P the photon beam polarization, Σ the beam asymmetry for the process, and ϕ the azimuthal angle of the recoil electron trajectory with respect to

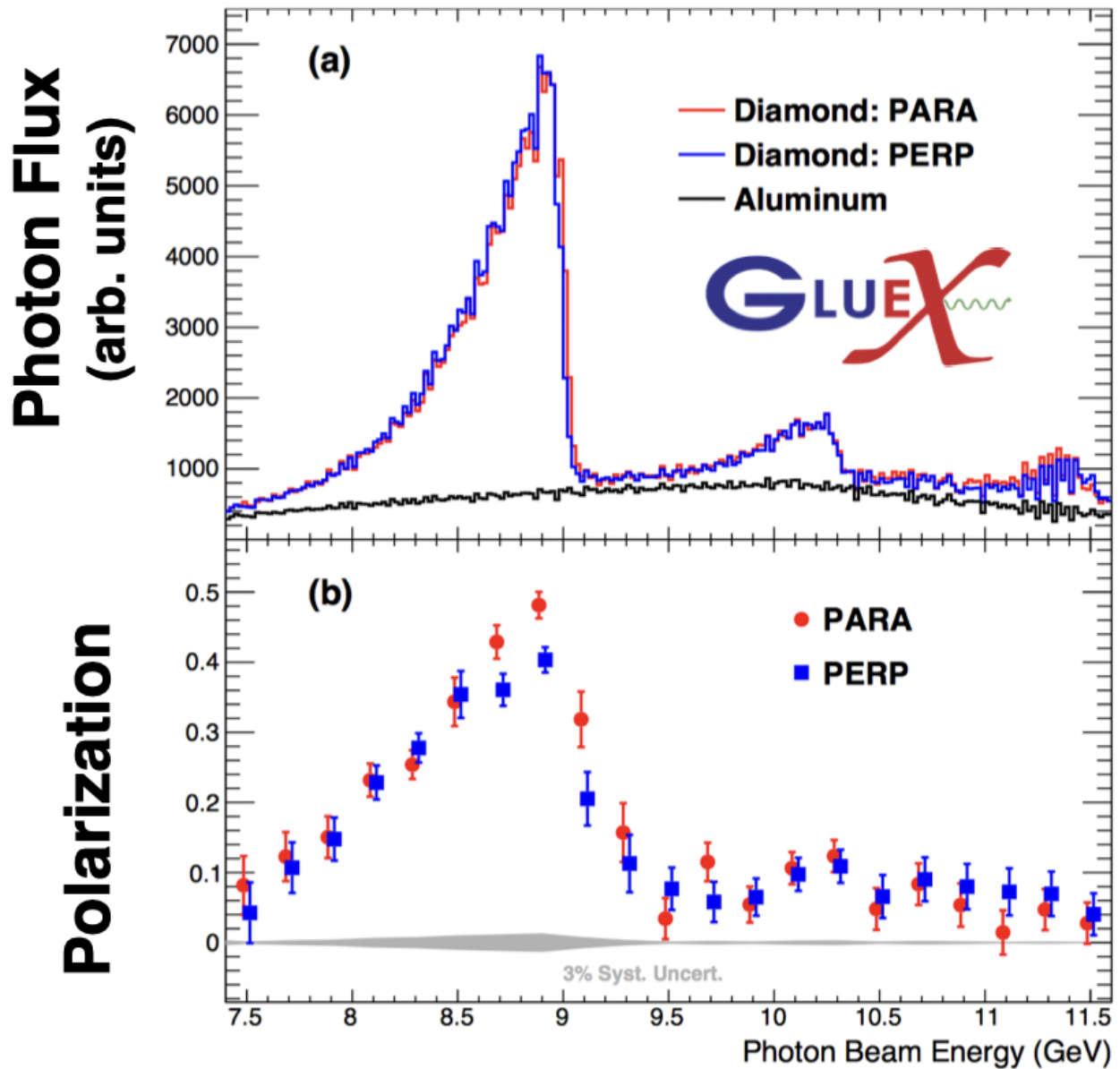


Figure 3.4: (Top) Photon flux as a function of beam energy for PARA ($0/90^\circ$) and PERP ($-45/45^\circ$) diamond orientations and for the aluminum radiator. (Bottom) Polarization fraction as a function of beam energy for PARA and PERP diamond orientations, the aluminum radiator produces an unpolarized photon beam. An increase in the photon flux is seen where the polarization fraction is enhanced. The coherent peak is referred to the beam energy range between 8.2–8.8 GeV [51].

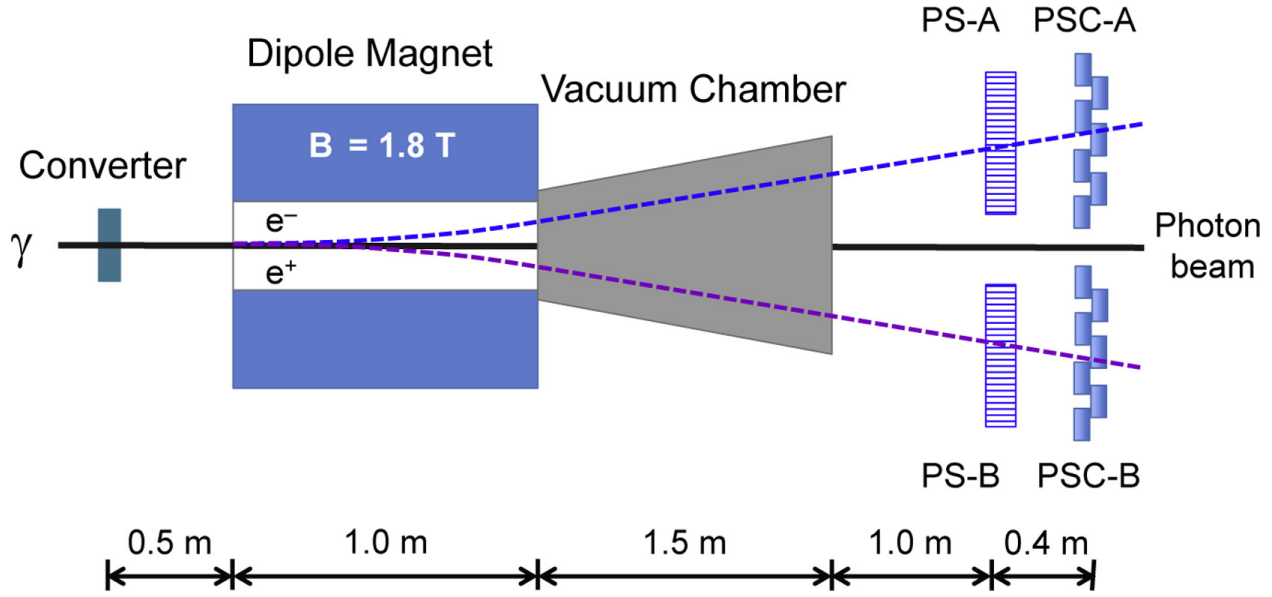


Figure 3.5: Schematic of the Pair Spectrometer. Figure taken from Ref. [57].

the plane of polarization for the incident photon beam. To determine the photon beam polarization, P , we can then record the azimuthal distribution of the recoil electron and fit it to the function $A(1 - B\cos(2\phi))$, where A and B are parameters with $B = P\Sigma$ ¹.

We use the TPOL to measure the recoiling electron that arises from triplet photoproduction. It consists of a converter tray and a positioning assembly for the beryllium foil to hold in place. The recoiling electron is detected by a silicon strip detector (SSD), providing the energy and azimuthal angle of the slower, recoiling electron. Because the high-energy electron pair is produced at much smaller angles, these electron pairs, along with any photons that did interact with the beryllium foil, continue down the beamline towards the PS. The PS, as shown in Figure 3.5, begins by bending the trajectory of the electron pairs with a 1.8 T dipole magnet. The electron pairs are then measured by two arms (one for e^+ and one for e^-), each with two layers of scintillators. The first layer is formed with two high-resolution hodoscopes called PS-A and PS-B. They each consist of 145 stacked scintillator tiles, each readout by silicon photomultipliers. The second layer is formed by a set of course counters called PSC-A and PSC-B, each consisting of 16 scintillating counters. These course counters are used to trigger on the e^+e^- pairs. The TPOL rely on these course counters to trigger on pairs in coincidence with the recoiling electron.

¹At 9 GeV, Σ has been measured to be 0.1990 ± 0.0008 for the GlueX beamline using a $75 \mu\text{m}$ beryllium foil[56].

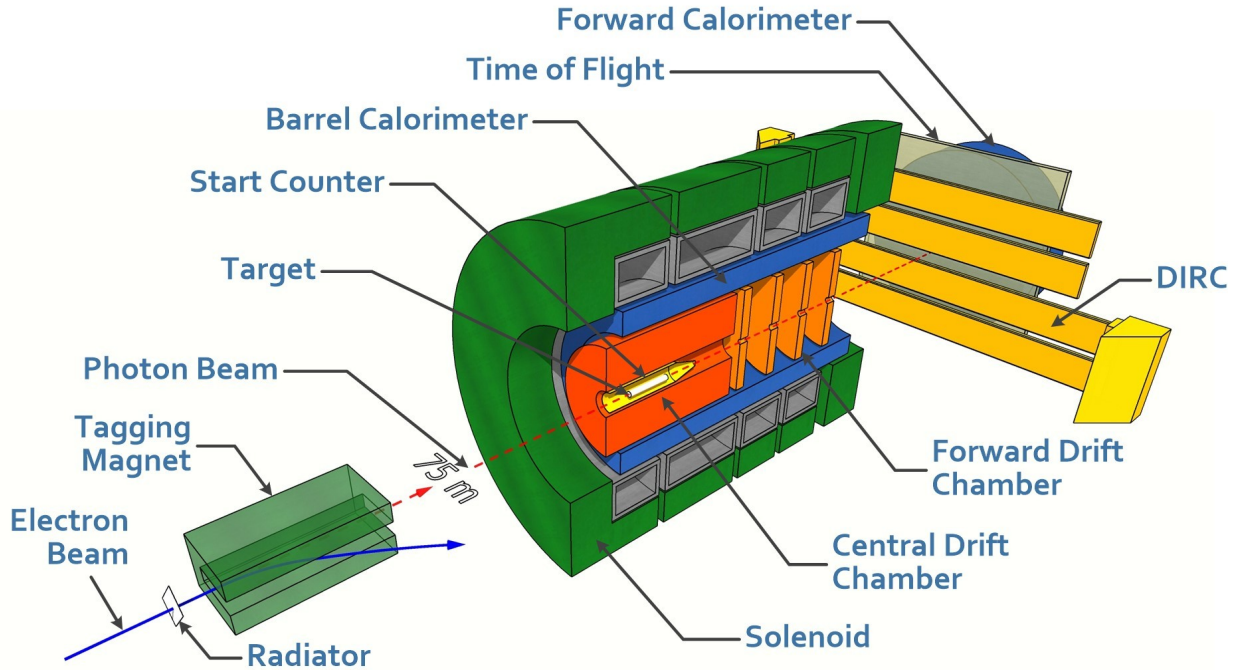


Figure 3.6: Schematic of the GlueX beamline and spectrometer [51].

Measuring the photon flux. Using the PS on triggered electron pairs, we determine the photon flux by counting these electron pairs and converting this using a known fraction of the photon beam to e^+e^- pairs as a function of beam energy. We get the total number of beam photons from the tagger system described previously. The PS is able to reconstruct photon energies from 6–12.4 GeV.

3.2 GlueX Spectrometer

Once the beam passes through the TPOL and PS, it finally reaches the LH_2 target, which is surrounded by the GlueX spectrometer. A schematic of the GlueX spectrometer is seen in Figure 3.6. Directly surrounding the target, we have the Start Counter (SC), Central Drift Chamber (CDC), Barrel Calorimeter (BCAL), and a superconducting solenoid magnet. Downstream of the target, we have the Forward Drift Chamber (FDC), DIRC (Detection of Internally Reflected Cherenkov radiation) detector, Time of Flight (TOF), and Forward Calorimeter (FCAL). Next, we will describe each of these components in detail.

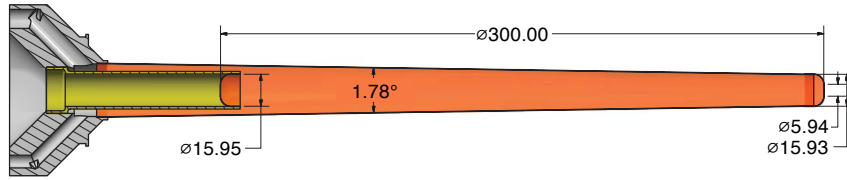


Figure 3.7: Liquid hydrogen target cell (dimensions are in mm) [51].

3.2.1 Target

The 30 cm long LH_2 target cell is located along the path of the photon beam, as seen in Figure 3.7. The target cell is contained within a vacuum chamber and operates at 18 K and 18 psi in nominal conditions. The walls of the cell where the photon beam enters and exits are made of 100 μm thick polyimide foils, which act as a window for the photon beam to enter.

3.2.2 Solenoid Magnet

Surrounding the target, drift chambers, and the BCAL, we have a superconducting solenoid magnet, shown in Figure 3.6. It has a bore diameter of 1.85m and a length of 4.8m. A 1350 A current passes through the solenoid during nominal run conditions, producing a 2T magnetic field along the central axis, where the photon beam passes through. It consists of four superconducting coils, colored gray in Figure 3.6, and four cryostats that maintain the coils at 4.5 K. Calculations have been performed to determine the expected magnetic field inside the solenoid. Along the central axis, these calculations have a maximum of 0.2% from the measured magnetic field. The largest deviation from the calculation was found to be downstream at large radii and is approximately 1.5%. Because the overall track efficiency of the spectrometer is much larger than these deviations, these deviations have very little effect on the momentum resolution and thus the calculated field maps are used for track reconstruction.

3.2.3 Charged Particle Reconstruction

For charged particle track reconstruction, we primarily use two sub-detectors, the CDC and FDC. These are both drift chambers, with the CDC focused on larger polar angles and the FDC focused on forward going charged particles. In this section, we will look at each of the drift chambers

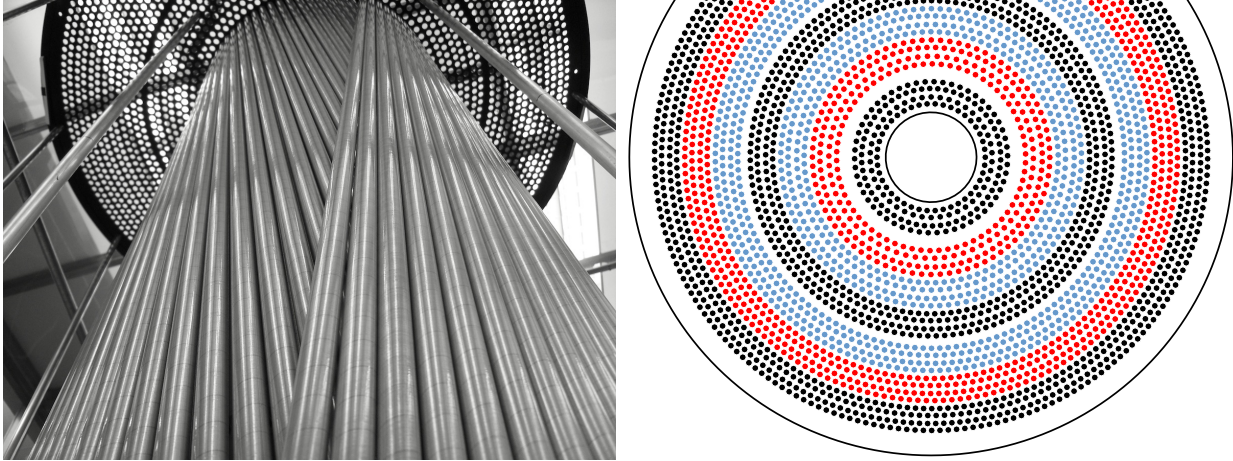


Figure 3.8: (Left) Picture of CDC during construction. (Right) Diagram of each CDC layer, straws parallel to the beam line are shown in black, straws with $+6^\circ$ stereo angle are shown in red and straws with -6° stereo angle are shown in blue. Figures taken from Ref.[58].

separately and then how they are used in conjunction with the other sub-detectors to reconstruct charged-particle tracks.

The Central Drift Chamber is a cylindrical straw tube drift chamber that tracks the position, timing, and energy loss information for charged particles. It surrounds the target and SC, but is fully located within the BCAL, as seen in Figure 3.6. It detects particles coming from the hydrogen target with polar angles between 6° and 168° , with an optimal range between 29° and 132° . The CDC consists of 3522 Mylar straw tubes arranged in 28 layers, 12 layers parallel to the beam, and 16 layers are at stereo angles of $\pm 6^\circ$, shown in Figure 3.8, to provide position information along the direction of the beam. Each 1.6 cm diameter tube contains a $20 \mu\text{m}$ diameter, gold-plated tungsten anode wire running down the middle of the tube, with each tube filled with a 50:50 mixture of Argon and CO_2 gas. A $+2.1\text{kV}$ current is passed through the wires. When charged particles ionize the gas inside the tubes, the ionized particles are attracted to the charged wire, creating a pulse in the voltage readout. If a particle passes within 4mm of the anode wire, we get a spacial resolution of $130 \mu\text{m}$ and detection efficiency per straw of 98%. The volume surrounding the tubes is enclosed with an inner fiberglass wall, an outer aluminum wall, and two circular end plates. The upstream end plate is made of aluminum, like the outer wall, but the downstream end

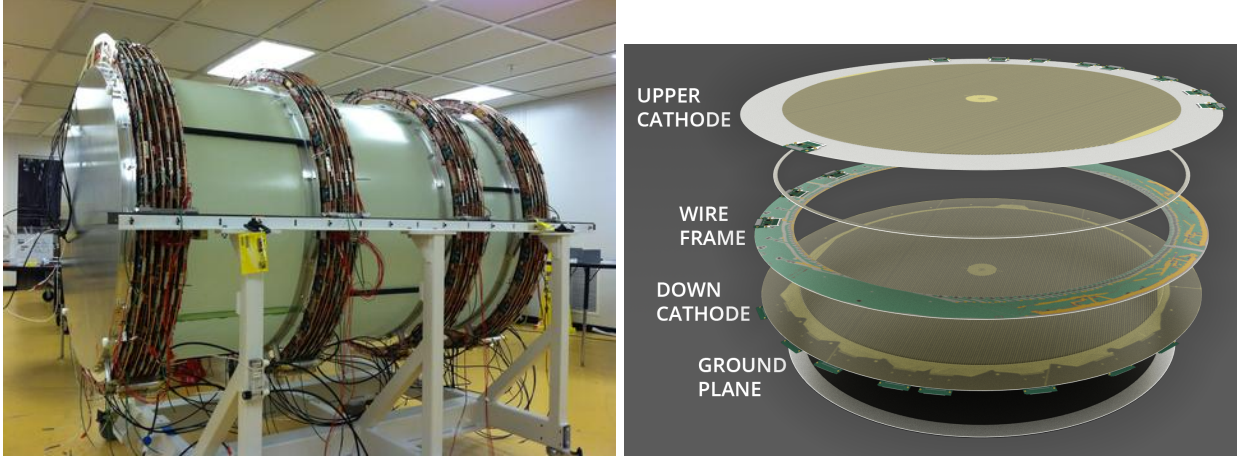


Figure 3.9: (Left) Picture of the fully assembled FDC. (Right) Rendition of one FDC chamber. From top to bottom: upstream cathode, wire frame, downstream cathode and ground plane that separates the chambers.

plate is made of carbon fiber to minimize energy loss.

The Forward Drift Chamber is inside the BCAL also, but located downstream of the target, as seen in Figure 3.6. It detects particles with polar angles between 1° and 10° with all chambers and up to 20° for partial coverage. It consists of 24 disc-shaped planar drift chambers, each 1 m in diameter, and grouped into four packages. Because of the high density of particles in forward region, forward tracking requires good separation of multiple tracks. This is achieved by sandwiching the wire plane between two grounded cathode strips a distance of 5 mm from the wire plane, allowing for a reconstruction of a space point for each tracked particle in each chamber. This can be seen in Figure 3.9. The wire plane consists of two wires 5 mm apart, a sense wire ($20 \mu\text{m}$ diameter) and a field wire ($80 \mu\text{m}$ diameter). The sense wire is kept at voltage of $+2.2\text{kV}$, while the field wire is kept at voltage -0.5kV . We fill the chambers with a mixture of 40% Ar and 60% CO_2 . The drift times from the wire signals are used to determine the position of the hit in the direction perpendicular to the wire plane. Using this information from each chamber, we can reconstruct high density tracks close to the beam line. This process can similarly be done for the two cathodes, strengthening our track reconstruction. We get a resolution of the position of between $140\text{--}240 \mu\text{m}$, depending on the distance from the hit to the wire.

Charged Track Reconstruction is done in the three stages. For forward-going charged particles, the process begins by forming track segments using hits recorded in adjacent layers of the FDC. The track segments are then connected using a helical model to form track candidates.

For charged particles with larger polar angles, a similar process is performed in CDC. Adjacent rings in the CDC form segments, with multiple segments connected using a helical model to form candidate tracks. Those particles going in the overlap region between the CDC and FDC (polar angle between $5^\circ - 20^\circ$) use both drift chambers to form track candidates.

The second stage involves using a Kalman filter to find the fitted track parameters z , D , ϕ , $\tan\lambda$, q/p_T at the position of closest approach of the track to the beam line. The parameters of the track candidate in the first stage are used as initial guesses. The Kalman filter then starts with the hits farthest from the beam line and proceeds hit by hit towards the hit closest to the beam line. Using a map of the magnetic field, we also take into account the energy loss and multiple scattering that can occur at each step. At this stage, all particles are assumed to be pions. Particles with momentum less than $0.9 \text{ GeV}/c$ are an exception; they are assumed to be protons.

The final stage incorporates the timing information from the Start Counter (SC), Time-of-Flight (TOF) detector, Barrel Calorimeter (BCAL), and Forward Calorimeter (FCAL) to determine the starting time of each track. This start time, combined with drift time information from the FDC and CDC, allows for a refined track fit. Unlike stage two, this refit considers all possible particle types: electrons (e^\pm), pions (π^\pm), kaons (K^\pm), and protons (p/\bar{p}).

3.2.4 Neutral Particle Reconstruction

Unlike charged particles that curve in a magnetic field, neutral particles travel in straight lines. Therefore, reconstructing their 4-momentum (energy and momentum) only requires their initial and final positions and times. However, determining the initial position, or vertex, for neutral particles presents a challenge. We rely on the reconstruction process described earlier for at least one charged particle, typically the recoiling proton, assuming a strong decay in which all particles originate from a common point. In weak decays, we allow the vertex to be displaced. Finally, we utilize the Forward Calorimeter (FCAL) and Barrel Calorimeter (BCAL), detailed below, to pinpoint the final position and time of the photons. We also use the Time-of-Flight (TOF) for timing information.

The Barrel Calorimeter is an electromagnetic sampling calorimeter that completely surrounds the CDC and FDC and lines the inside of the solenoid magnet, forming an open cylinder. It has complete coverage in the azimuthal angle and detects photon showers with polar angles between $11^\circ - 126^\circ$. Its dimensions can be seen in Figure 3.10. The BCAL is constructed as a matrix of 0.5 mm -thick lead sheets and 1.0 mm -diameter multicladd scintillating fibers. It consists of 48

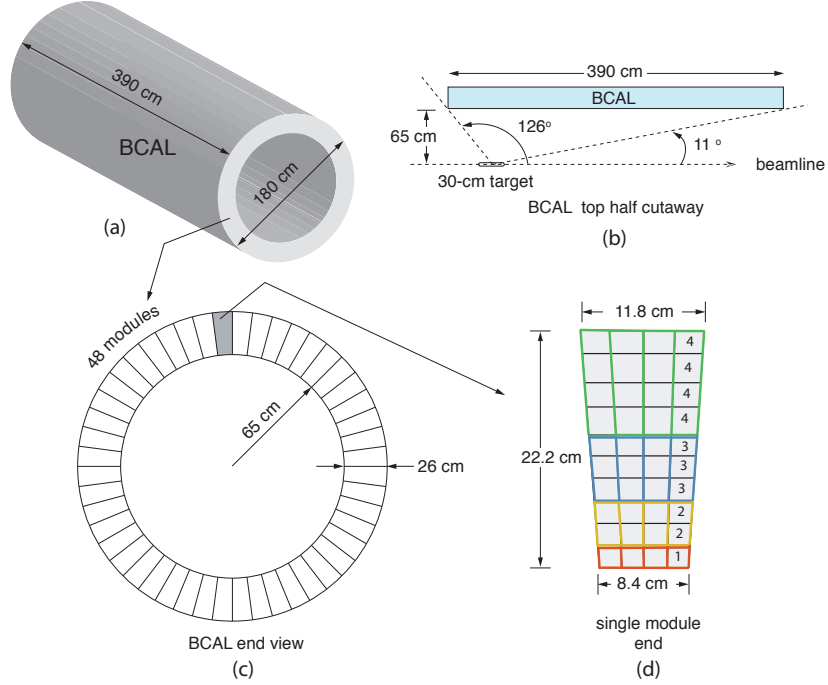


Figure 3.10: Three dimensional rendition of the BCAL. Figure taken from Ref. [59].

optically-isolated modules, each covering about 7.5° in the azimuthal angle and spanning the entire length of the BCAL. Each module has about 185 total layers, all grouped into 10 bunches with the bunches split into 4 groups, shown in Figure 3.10. Each module has approximately 15,000 fibers that run parallel to the beam line. The light generated in the fibers gets collected by small light guides at each end of the module. These light guides transport the light into silicon photomultipliers (SiPMs), which were used because of their insensitivity to the magnetic field. Each module has 40 SiPMs that generate signals that are delivered to the FADCs. The reconstruction of showers is done using a cluster algorithm that groups signals, called hits, close in time and space to get the shower energies and positions in the BCAL. A more detailed description of this BCAL clustering algorithm can be found in Ref. [59]. Using π^0 and η production, the BCAL was determined to have an energy and spatial resolution of $\sigma_E/E < 10\%$ and 150 ps at 1 GeV, respectively.

The Forward Calorimeter is placed 5.6 m downstream of the center of the target. It is completely outside the solenoid magnet and detects photon showers between $1^\circ - 11^\circ$ in the polar angle. The FCAL consists of 2800 lead glass blocks stacked in a circular 2.4m diameter array, shown in the left picture in Figure 3.11. Each lead glass block is rectangular prism with dimensions $4 \text{ cm} \times 4 \text{ cm} \times 45 \text{ cm}$ that are connected to photo-multiplier tubes (PMTs) by a acrylic cylindrical

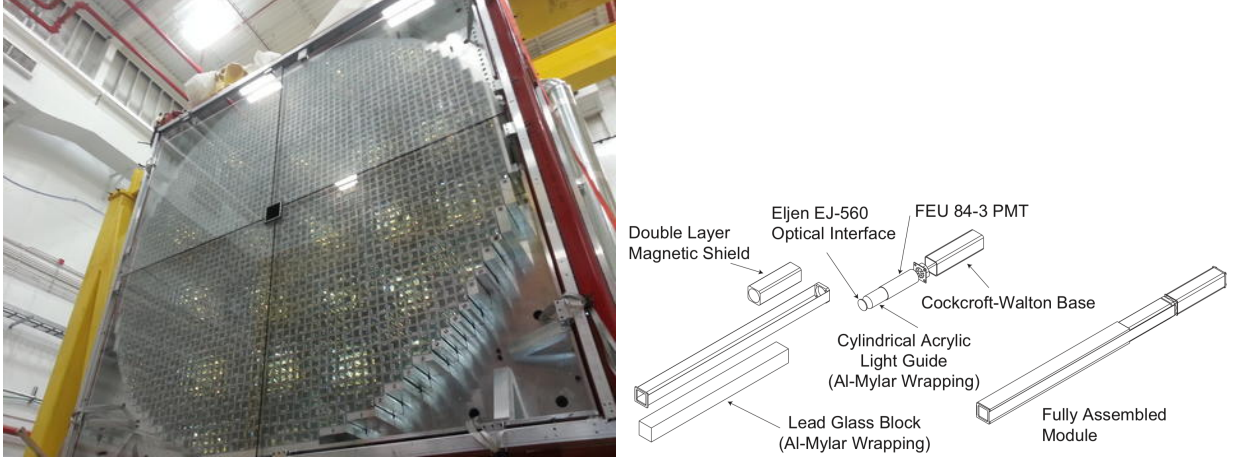


Figure 3.11: (Left) Picture of the FCAL inside Hall D. (Right) Components of an FCAL block.

light guide. Majority of the lead glass blocks and PMTs were taken from the decommissioned E852 experiment at Brookhaven National Laboratory and the decommissioned RadPhi experiment at JLab. A schematic of a single FCAL module is shown in the right figure in Figure 3.11. The signals from the PMTs are routed to FADC electronics directly behind the FCAL. Using a clustering algorithm, described in Ref. [60], we are able to determine the showers' energy and position in the FCAL. The resolution of the FCAL was found using the same technique as the BCAL: through π^0 and η production. The FCAL was determined to have an energy and spatial resolution of $\sigma_E/E < 11\%$ and 70 ps at 1 GeV, respectively.

3.2.5 Particle Identification

As mentioned above, the two scintillator-based detectors, the Start Counter (SC) and the Time-of-Flight (TOF), provide timing information. However, the energy loss (dE/dx) in the SC and the flight time from the TOF can also be used to identify charged particles.

The Start Counter surrounds the LH_2 target and covers $\sim 90\%$ of the solid angle of particles coming from the center of the target. The Start Counter (SC), shown in Figure 3.12, consists of thirty 3 mm thick and 600 mm long scintillator paddles, which form a cylinder shape around the target. To minimize acceptance loss in the forward region, the edges of the paddles are bent to create a nose section, shrinking the radius from 78 mm to 20 mm at the downstream end. These scintillator paddles are connected to silicon photomultipliers (SiPMs), since these are not affected by the solenoid magnet, and get readout by FADCs. The main purpose of the SC is to select the beam bunch that generated the tagged photon that created the reaction of interest. Each hit

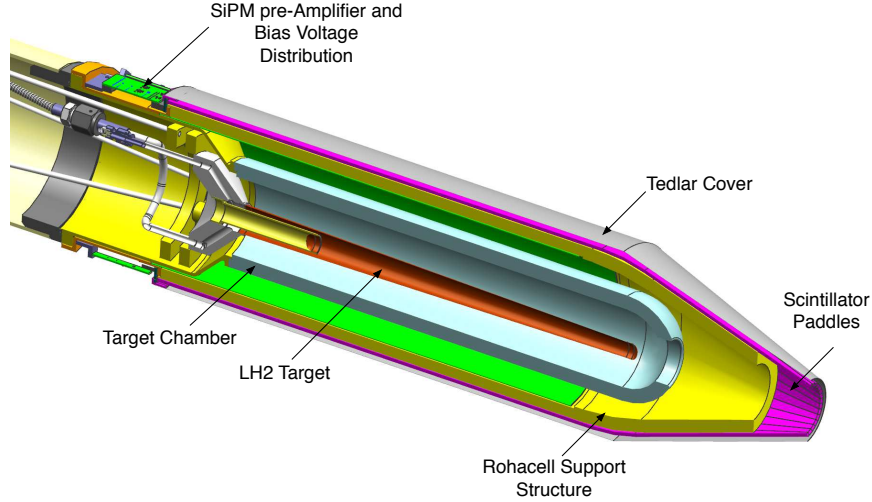


Figure 3.12: Start Counter and target. The photon beam exits through the conically shaped end of the SC, see Ref. [61].

provides both this timing information, with a resolution of 234 ps, and energy loss (dE/dx), being able to separate protons from electrons, pions, and kaons up to $p = 0.9 \text{ GeV}/c$.

The Time of Flight is a wall of scintillators located in front of the FCAL at $\approx 5.5 \text{ m}$ downstream of the target, shown in Figure 3.13. It delivers fast timing signal from charged particles with polar angles between 0.6° and 13° for the purpose of particle identification. It consists of two layers of scintillators with a $12 \times 12 \text{ cm}^2$ hole in the center of the beam line. One layer has scintillator paddles stacked horizontally with the other layer stacked vertically. Each paddle outside the beam hole region is connected at each end to a PMT by a light guide. These paddles are 252 cm long, 6 cm wide, and 2.54 cm thick. The paddles inside the beam hole region are only connected to a single PMT and measure 120 cm long with the same width and thickness as the others. Using the vertical and horizontal paddles, we are able to make an xy-grid of the hits in the TOF, giving us both position and timing information. The TOF has a timing resolution of $\sim 100 \text{ ps}$. The right plot in Figure 3.13 shows velocity vs. momentum for positively charged tracks detected by the TOF. In the Start Counter, we could only separate protons up to $p = 0.9 \text{ GeV}/c$ and could not distinguish between pions and kaons. In the TOF, clear bands can be seen starting at the top left with positrons, pions, kaons, and protons. We can distinguish, with high uncertainty, kaons up to $p = 2 \text{ GeV}/c$ and protons up to $p = 4 \text{ GeV}/c$.

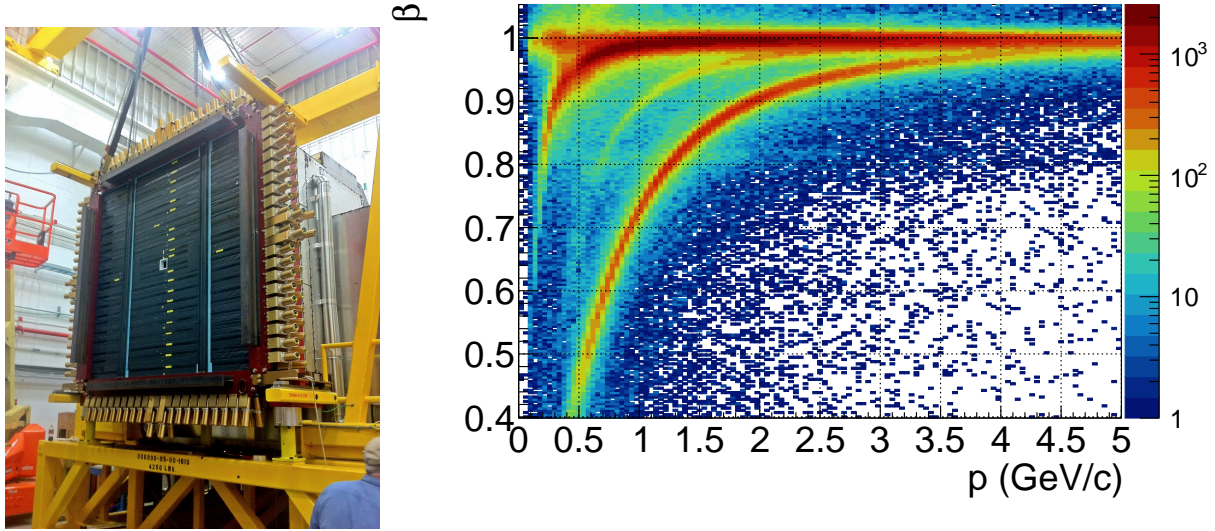


Figure 3.13: (Left) Picture of TOF being lifted into place. (Right) Velocity vs. momentum of positively charged tracks. Bands correspond to e^+ , π^+ , K^+ and p for the TOF detector.

Due to the increase in beam current for GlueX II runs, an update needed to be made to the TOF in 2019 between phases I and II. Since the TOF paddles near the beam hole were already close to their limit, this update focused mainly on increasing the beam hole from $12 \times 12 \text{ cm}^2$ to $18 \times 18 \text{ cm}^2$ hole and increasing the segmentation of the panels around the beam hole. The 4 double-sided paddles surrounding the beam hole were replaced with 8 smaller paddles, 4 at 4.5 cm and 4 at 3 cm. The 4 single-sided paddles that border the beam hole were replaced with 8 paddles at 4.5cm, that match the increase in the size of the beam hole. This allowed for better timing resolution around the area that is most impacted by the increase of beam current.

3.2.6 The DIRC Detector

Before the start of GlueX Phase II in 2020, the DIRC detector (Detection of Internally Reflected Cherenkov Radiation), shown in Figure 3.14, was added to the GlueX spectrometer. Its purpose was to improve the separation of charged pions and kaons with momentum up to $\sim 4 \text{ GeV}$. The first two runs of Phase II, taken in 2020 and 2023, have been collected with the addition of the DIRC and are approximately twice the size of all Phase I. The DIRC detector was not used in this analysis.

The DIRC, housed directly in front of the TOF, resuses four unmodified bar boxes from the BaBar Experiment at SLAC[64], each with twelve 4.9 m long fused silica radiator bars. These bars

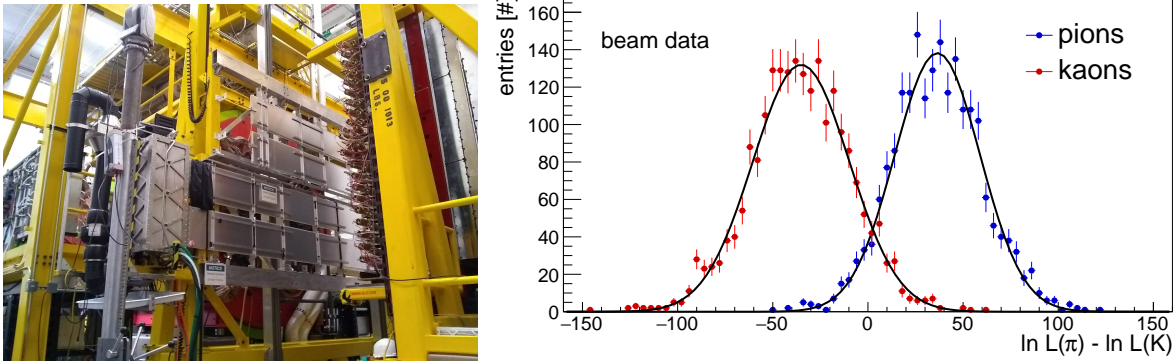


Figure 3.14: (Left) Picture of the installed DIRC detector, figure taken from Ref. [62]. (Right) Log-likelihood difference distribution for 4000 π/K events with 3.5 GeV momentum. The π/K separation is at a 3σ level. Figure taken from Ref. [63].

are attached to two compact photon expansion volumes, both filled with distilled water to match the refractive indices of the radiator and photon detectors. When charged particles pass through a dielectric material, such as distilled water, at a greater speed than light in that material, photons are emitted, called Cherenkov radiation. Since the emission angles of these photons are based on the mass of the charge particle, by collecting the Cherenkov radiation, we can separate pions from kaons. Using mirrors, we focus the photons on an array of Multi-Anode Photomultipliers (MaPMTs), each with sixty-four $6 \times 6 \text{ mm}^2$ area pixels. The photon timing resolution is $\sim 0.8 \text{ ns}$. When including the DIRC information, we can identify 3.5 GeV momentum pions and kaons with a 3σ confidence, shown in Figure 3.14.

3.2.7 Trigger and Data Acquisition

To reduce background events induced by low-energy electromagnetic and hadronic interactions, we used two main triggers. We previously discussed the first trigger applied on the pair spectrometer. The second trigger algorithm is applied on measurements of energy deposition in the FCAL and BCAL. For the second trigger to be satisfied, one of two conditions must be true:

- $2 \times E_{FCAL} + E_{BCAL} > 1 \text{ GeV}, E_{FCAL} > 200 \text{ MeV}$
- $E_{BCAL} > 1.2 \text{ GeV}$

where E_{FCAL} and E_{BCAL} are the total energy depositions in the given calorimeter. The first trigger condition is in place because a large portion of events of interest have the most energy in

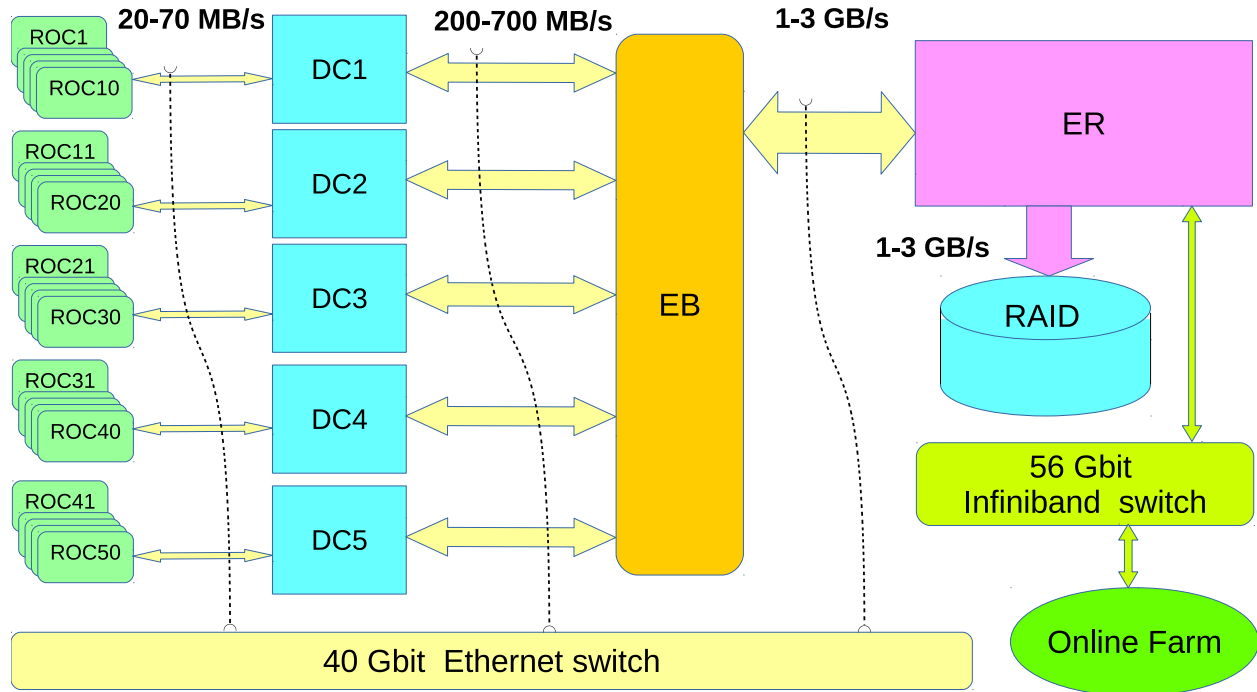


Figure 3.15: Schematic data acquisition system for GlueX [51].

the forward-going region. The other trigger condition is important for accepting events with large transverse energy, such as J/ψ decays, where most of the energy is deposited in the BCAL.

If an event satisfies the trigger conditions, it enters the data acquisition system (DAQ), shown Figure 3.15. Data from a particular event first enters the readout controller (ROC), which transfers data to the Data Concentrators (DC) at a rate of 20–70 MB/s. The DCs are programs able to build partial events received from several crates. These partially constructed events are routed, at a rate of 200–700 MB/s, to the Event Builder (EB) to build complete events. These complete events are sent to the Event Recorder (ER) that writes data to local data storage. All paths are routed through the 40 Gb Ethernet switch, while the online monitoring system has a separate 56 Gb Infiniband switch.

CHAPTER 4

DATA ANALYSIS

4.1 Overview

In the following, we present an analysis of J/ψ photoproduction using the complete GlueX-I dataset combined with the GlueX-II data collected in 2020. This chapter details the process of isolating a sample of the exclusive reaction

$$\gamma p \rightarrow J/\psi p \rightarrow \mu^+ \mu^- p,$$

beginning with a description of the datasets and data processing stages, including the selection criteria and particle identification methods used to filter relevant events. We then outline the reconstruction techniques employed to identify charged particle tracks, validate final states, and differentiate muons from similar particles, such as pions, through kinematic fitting and refined selection strategies.

Since very few reactions (and none at this high in mass) in our experiment have a two-muon final state, the primary goal of the event selection is to remove misidentified events, such as those where the charged particles are actually pions, kaons, electrons, etc., rather than muons. The largest and most problematic misidentification is the pion: given the pion's similar mass to the muon (approximately 135 MeV versus 106 MeV), distinguishing between the two based on kinematic fitting presents a challenge, making this separation a critical part of our analysis and a primary focus of this chapter.

Following event reconstruction, we present the key measurements, including the total cross section and the differential cross section as a function of Mandelstam- t , providing insight into the photoproduction dynamics of J/ψ at the energies probed. Finally, we review the systematic studies conducted to assess potential uncertainties, covering factors such as detector resolution, particle misidentification rates, and background contamination. This chapter thus provides a comprehensive framework for the analysis of J/ψ photoproduction, emphasizing both the precision of the measurements and the robustness of our methods.

4.1.1 Datasets

The GlueX collaboration is scheduled for data to be taken in two phases, referred to as GlueX-I and GlueX-II. The first phase, GlueX-I, was divided into the three run periods labeled by when they were taken: Spring 2017, Spring 2018, and Fall 2018. The integrated luminosity for each run above the J/ψ threshold (8.2 GeV) is 53.1, 152.7, and 98.1 pb^{-1} , respectively, which corresponds roughly to a ratio of 1:3:2. This gives a total integrated luminosity of 304 pb^{-1} for the full GlueX-I dataset. The second phase, GlueX-II, is also divided into the three run periods, two of which have already been completed, and the third is scheduled to start early 2025. In this analysis, we will only look at the first run period of GlueX-II taken in 2020 with an integrated luminosity of 321.2 pb^{-1} above the J/ψ threshold, which is roughly equivalent to all of GlueX-I. The combination of the full GlueX-I dataset and the GlueX-II dataset taken in 2020 produced ~ 6 PB of raw data. The GlueX collaboration, through computing centers at Jefferson Lab, the National Energy Research Scientific Computing Center (NERSC), the Pittsburgh Supercomputing Center (PSC) and Indiana University, processes the raw data into Reconstructed Event Storage (REST) files, reducing down to ~ 1 PB of data. Based on a set of standardized criteria for particle identification, we can reconstruct a particular reaction of interest from these REST files. The GlueX Collaboration manages this through Analysis Launches, where reactions of interest to GlueX members are reconstructed. The Analysis Launch version used for each data set in this analysis can be seen in Table 4.1.

Table 4.1: Summary of datasets used for this analysis

Run Period	REST Version	Analysis Launch Version
2017-01	3	37
2018-01	2	09
2018-08	2	07
2019-11	1	05

Table 4.2: Summary of simulation samples used for this analysis.

Run Period	Halld_recon Version	Random Trigger Versions
2017-01	recon-2017_01-ver03.9	recon-2017_01-ver03.2
2018-01	recon-2018_01-ver02.8	recon-2018_01-ver02.2
2018-08	recon-2018_08-ver02.8	recon-2018_08-ver02.2
2018-08	recon-2019_11-ver01.3	recon-2019_11-ver01

For this analysis, a few loose standard event selections are used to reconstruct $\gamma p \rightarrow J/\psi p \rightarrow \mu^+ \mu^- p$ events, prior to the selections mentioned below. These loose standard cuts are mainly timing cuts on the BCAL, TOF, FCAL, and SC mentioned in chapter 3. These timing cuts look at the time difference between the RF time, the accelerators time associated with each electron beam bunch produced, and the time recorded by the subdetector for the hit associated with that event. These standard timing cuts, shown in table 4.3, were determined for each particle using simulations. In this analysis, some of these timing cuts were loosened even more to prevent the removal of any J/ψ events. In particular, all FCAL and BCAL timing cuts (except for those on the photon) were loosened to ± 2.5 ns. The only other loose selection made was on the missing mass squared (MMS) of the reaction, which is the invariant mass squared of the final state particles minus the invariant mass squared of the initial state particles. We require that $|MM|^2 < 2.5 (\text{GeV}/c)^2$.

Table 4.3: Summary of loose timing cuts.

PID	BCAL/RF Δt (ns)	TOF/RF Δt (ns)	FCAL/RF Δt (ns)	SC/RF Δt (ns)
γ	± 1.5	NA	± 2.5	NA
e^+	± 1.0	± 0.5	± 2.0	± 2.5
e^-	± 1.0	± 0.5	± 2.0	± 2.5
μ^+	± 1.0	± 0.5	± 2.0	± 2.5
μ^-	± 1.0	± 0.5	± 2.0	± 2.5
π^+	± 1.0	± 0.5	± 2.0	± 2.5
π^-	± 1.0	± 0.5	± 2.0	± 2.5
K^+	± 0.75	± 0.3	± 2.5	± 2.5
K^-	± 0.75	± 0.3	± 2.5	± 2.5
p	± 1.0	± 0.6	± 2.0	± 2.5
$p\bar{p}$	± 1.0	± 0.6	± 2.0	± 2.5

4.1.2 Simulation

In addition to data collection, we also need to have a good understanding of the efficiency of our detector if we want to accurately calculate cross sections. To do this at GlueX, we use Monte Carlo (MC) to simulate our detector response for signal events, i.e. $\gamma p \rightarrow J/\psi p \rightarrow \mu^+ \mu^- p$ events. We do this in a four-step process using a GEANT-based software package.

The process begins by generating four vectors of our given reaction $\gamma p \rightarrow J/\psi p \rightarrow \mu^+ \mu^- p$ using the generator *bggen* based on Pythia [51]. Taking information about the photon beam (energy distribution, coherent peak energy, etc) from our calibration database and the energy and

t-dependence of the cross section of the reaction, *bggen* generates four vectors in a format suitable for the next stage in the GEANT simulation.

These generated events are fed through the Hall D GEANT (*hdgeant4*) simulation code, which is based on the GEANT4 framework. *hdgeant4* tracks particles through our experimental setup and records the signals (hit times and energies) that are produced in our detector. The behaviour of the detector is specific to each run number and is based on certain conditions taken from our calibration database such as beam polarization and intensity, beamline and detector geometry, magnetic field maps, etc [51].

The next step is to convert this time and energy signal from *hdgeant4* into electronic detector responses that match the readout from the experiment using a detector response package called *mcsmeas*, producing an output that is identical to what is found in real data. At this stage, run-dependent efficiency effects (such as missing electronic channels, etc.) and additional smearing of some signal are applied to better match the Monte Carlo to real data. The *mcsmeas* package also factors in additional hits from uncorrelated backgrounds, which are provided from files containing real background samples using random triggers [51].

The last step in producing simulated data is reconstruction. We process these Monte Carlo events through the same reconstruction software used for real data. The output is saved to REST files, which can be used in the same way as real data REST files are.

4.2 Event Kinematics and Calorimeter Motivation

A key aspect of accurately analyzing J/ψ photoproduction is understanding the kinematic properties of these events and the role of the calorimeters in capturing them. Examining the kinematic distributions provides insight into how these event kinematics influence the detection efficiency and the need to understand the calorimeter-based triggers.

4.2.1 Kinematic Distributions of J/ψ Photoproduction Events

J/ψ photoproduction events exhibit diverse momentum and angular distributions, as shown in Figure 4.1. At higher photon energies, events are generally scattered at forward angles, making them suitable for detection in the Forward Calorimeter (FCAL). Lower energy events, which tend to scatter at wider angles, fall within the coverage of the Barrel Calorimeter (BCAL). These distributions underline the need for both the FCAL and the BCAL to ensure that events across the full angular spectrum are detected, thus capturing the entirety of J/ψ photoproduction events.

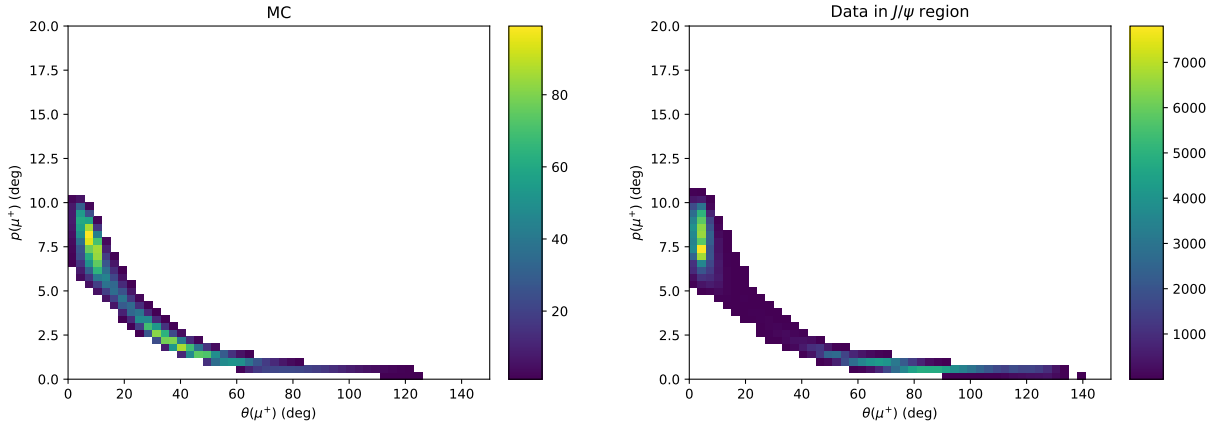


Figure 4.1: Momentum (p) versus polar angle (θ) distributions for positively charged muons (μ^+). The left plot shows Monte Carlo (MC) simulation results, while the right plot presents the corresponding distribution from experimental data in the J/ψ mass region.

4.2.2 Calorimeter Energy Distributions

Figure 4.2 presents the 2D total energy distributions across both calorimeters for Monte Carlo (MC) simulation. The majority of detected events lie near the lower end of the energy range, especially for wide-angle events in the BCAL, which places them close to the calorimeter trigger thresholds, which are represented by the red lines.

Since many events are detected at energies close to these thresholds, the accuracy of trigger simulations is important to ensuring that our analysis correctly represents the events passing the experimental triggers. Specifically, our detector efficiency is sensitive to accurate trigger simulations. This effect is particularly evident in the comparison between data and MC, where slight shifts in energy distributions near the threshold can reveal calibration or simulation discrepancies.

The kinematic properties and calorimeter responses show the need to understand the two primary calorimeter-based triggers: the FCAL/BCAL trigger, which covers both forward- and wide-angle events, and the BCAL-only trigger, tailored to lower-energy, wide-angle events. Although most GlueX analyzes use the FCAL / BCAL trigger for comprehensive event coverage, the BCAL only trigger enables efficient capture of J/ψ events where all particles populate the central part of the detector.

These kinematic insights are foundational for the cross-section analysis that follows. In addition, they support subsequent sections by explaining the rationale behind event selections.

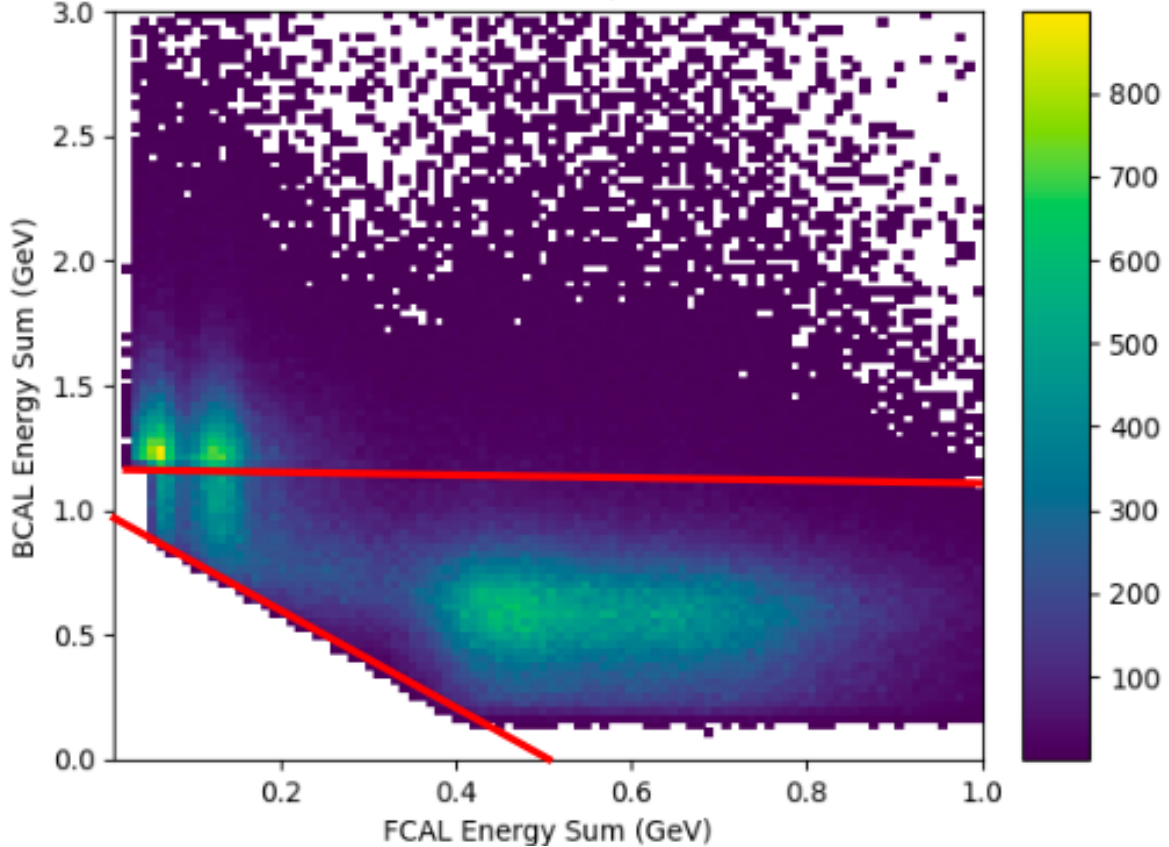


Figure 4.2: The 2D total energy distributions across both calorimeters for Monte Carlo (MC) simulation. Calorimeter trigger thresholds are represented by the red lines.

4.3 Event Selections

We will now discuss the event selections that we use to make sure that we are accurately identifying $\gamma p \rightarrow J/\psi p \rightarrow \mu^+ \mu^- p$ events. As discussed before, the first selection on the data is done using the calorimeter triggers mentioned previously. After these triggers, the purpose of the next few event selections is to select events where the 3 charged particles correspond to a muon pair and a proton. To do this, we begin with a selection on the beam energy, where we remove events below the threshold for J/ψ production of 8.2 GeV. Next, we use a background subtraction method known as accidental subtraction to correctly match an event to its incoming photon. We then make a selection that constrains the kinematics of the reaction to require exclusivity, a technique called kinematic fitting. However, since the mass of the muon is very similar to that of the pion, this kinematic fitting does not distinguish between muons and pions. We will use three other selections to distinguish between the muon and the pion: one on the energy deposition in the FCAL, one on

the energy deposition in the BCAL, and one on the polar angle of the muons.

4.3.1 Accidental Subtraction

Because the CEBAF electron beam comes into Hall D in bunches every 4 ns and each beam bunch has a relatively high intensity, some events are tagged with multiple photons of different energies. Photons that are consistent with an event but did not produce that event are called accidentals. To make sure that we are properly matching events to the corresponding photon, we use a technique called accidental subtraction. Since each photon is treated as independent from every other photon, there is no difference between accidental photons produced by the same beam bunch and those produced in a different beam bunch. In Figure 4.3, we see each events RF time, which is the accelerators time associated with each electron beam bunch produced. The central peak is known as the prompt peak and represents the correct choice in RF bunch associated with the beam photon. We define photons in this peak as “in time”. The side peaks are known as “out-of-time” beam photons, which show a 4 ns pattern matching that of the 4 ns timing between electron bunches. Since we can expect the number of mismatched events to be about the same in each peak, we can utilize a weighted sideband subtraction of the RF time distribution to remove these mismatched events from the “in-time” events. The in-time events are given a weight of +1, and the “out-of-time” events are given a weight $-1/8$ because there are 8 beam bunches outside of the main peak. All “out-of-time” events can be given the same weight, since each side peak is roughly the same.

4.3.2 Kinematic Fitting

Since we only require that our events have 3 charged tracks (2 positively charged tracks and 1 negatively charged track) in our final state, we have to distinguish the muons and proton from other charged particles. For this analysis, we use kinematic fitting to do some of this separation and require exclusivity for each event. Kinematic fitting is the act of varying the measurements within their uncertainties such that the resulting values are consistent with the external constraints on the system. The constraints in this analysis are energy and momentum conservation as well as a position constraint on the final-state particles so that they come from the same vertex. We then define the χ^2 of this kinematic fit and normalize it to the number of degrees of freedom (NDF). In this analysis, selecting events with low χ^2/NDF from the kinematic fit primarily removes events with a large missing mass or missing energy, such as those with additional undetected particles.

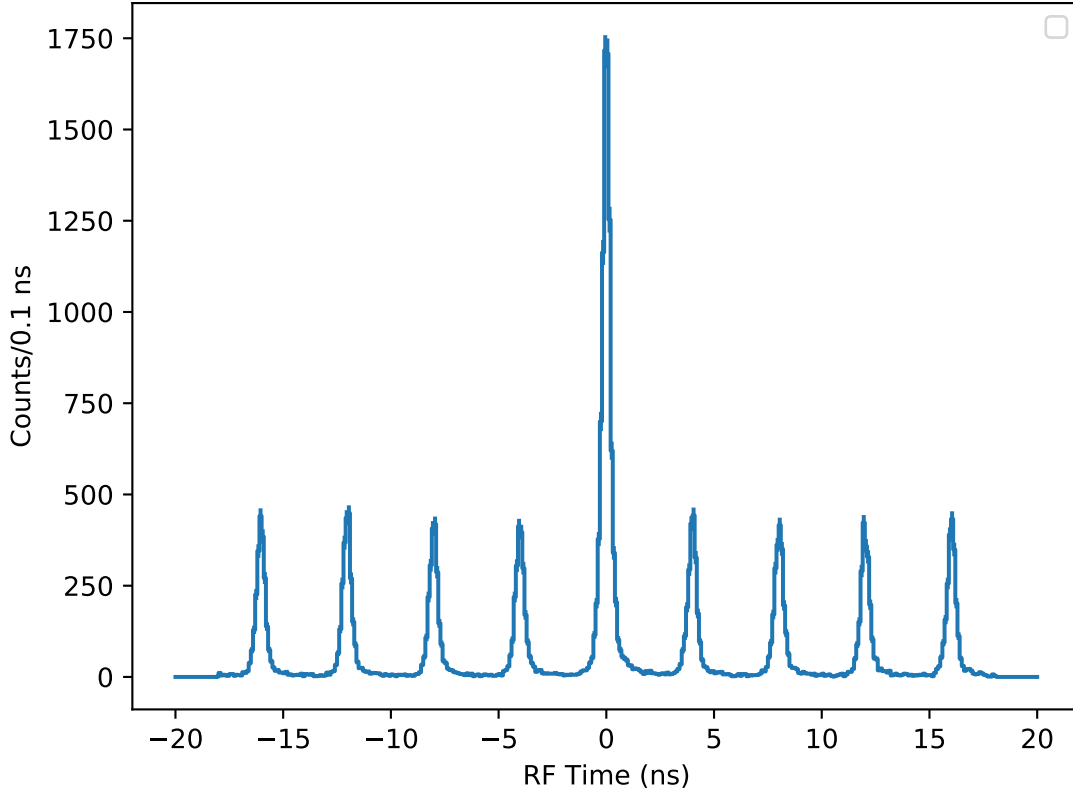


Figure 4.3: Difference between the measured time of the beam photon and RF time. Events in the tallest middle peak are “in-time” and given a weight of 1. Events in the 8 smaller peaks are “out-of-time” and given a weight of $-1/8$.

It also removes many of the events that have charged particles with masses much different than the muons (such as Kaons and electrons) by constraining the 4-momenta to conserve energy and momentum. An example of this χ^2 distribution can be seen in the plot on the left of Figure 4.4. The red line represents arbitrarily weighted Monte Carlo, while the blue is data in the J/ψ region. We see a large tail in data that mostly comes from events that have extra, undetected particles, causing a large missing mass and energy. There is still a mismatching between data and Monte Carlo, which is primarily coming from events with misidentifying pions. These events can still have low χ^2/NDF , so we use other selections to remove these events.

To determine what selection criteria we need to use, we conducted a systematic analysis to optimize signal-to-background ratio without compromising signal significance. We did this by loosening all selections and systematically tightening them to find the maximum signal significance,

which we approximate as

$$\text{significance} \approx \frac{S}{\sqrt{S+B}} \quad (4.1)$$

where S is the estimated signal yield and B is the estimated background in the signal region. To estimate the signal, S , for different values of a cut parameter, we weight simulated signal events using the cross section results from our published results to approximate the yields in data with reconstructed Monte Carlo. We define a signal region centered on the J/ψ mass (3.096 GeV) with a width of $\pm 3\sigma$ (3.096 ± 0.039 GeV), based on the GlueX published $J/\psi \rightarrow e^+e^-$ mass and width measurements [33]. To estimate the background, B , for different values of a cut parameter, we found the number of events from data in the sideband regions around the peak (2.9 GeV - 3.0 GeV and 3.2 GeV - 3.3 GeV). We then scaled this value using a signal region to background region ratio to get an estimate of background events in the peak region. In the right plot on Figure 4.4, we see the results of this analysis for the χ^2/NDF selection, and it was through this analysis we chose select events to have a $\chi^2/\text{dof} < 5$, signified by the red line in figure 4.4.

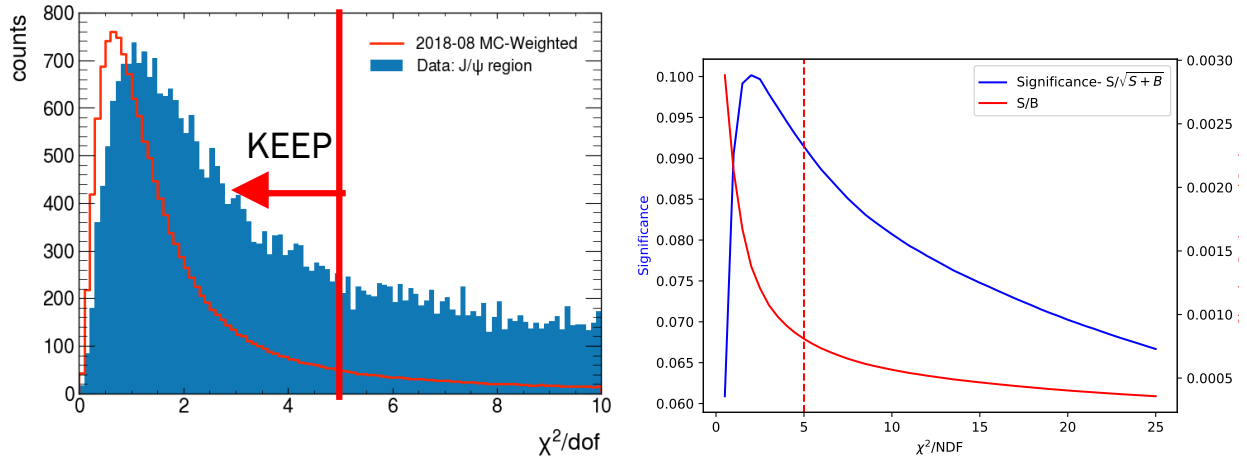


Figure 4.4: (Left) χ^2/NDF in Data and Monte Carlo. This is only in the $M(\mu^+\mu^-)$ region of $M(J/\psi) \pm 3\sigma$. The Monte Carlo is arbitrarily weighted to match heights. The red line represents where the selection was made, and we keep events to the left of that line. (Right) χ^2/dof significance distribution. The red dashed line signifies where our selection is made. We chose events with $\chi^2/\text{dof} < 5$.

4.3.3 Muon/Pion Separation: FCAL Energy Deposition

The first of the three selections used to help reduce the background due to misidentified pions (as discussed above) is a cut on the energy deposited by the muons in the FCAL. We expect the muons to deposit constant energy into the calorimeters per unit length; however, this is not the case

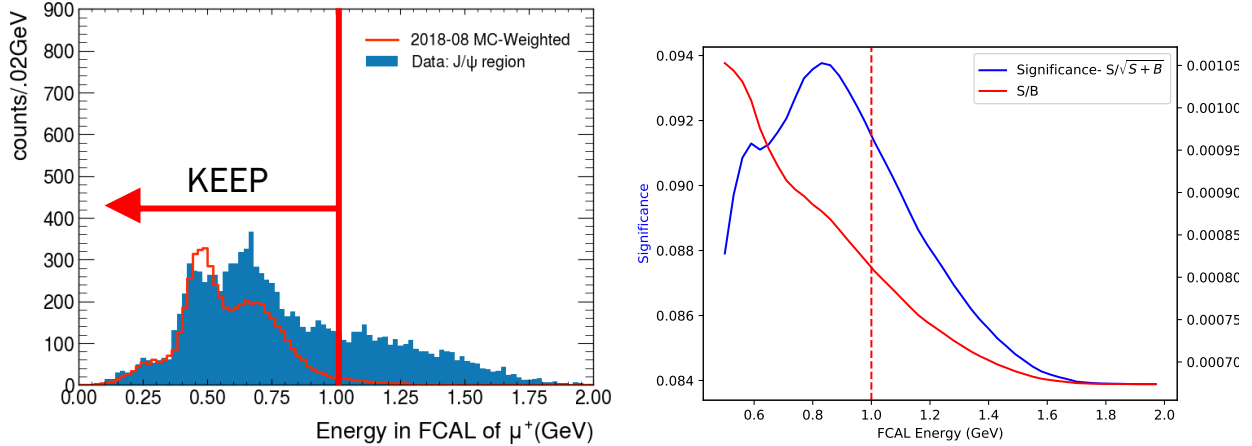


Figure 4.5: (Left) Energy in the FCAL distribution in Data and Monte Carlo. This is only in the $M(\mu^+\mu^-)$ region of $M(J/\psi) \pm 3\sigma$. The Monte Carlo is arbitrarily weighted. The red line represents where the selection was made, and we keep events to the left of that line. (Right) Significance and signal to background ratio distributions of energy deposited in the FCAL. The red dashed line signifies where our selection is made. We chose events with Energy in FCAL $< .5$ GeV.

for all pions. Because some of the pions will interact with the nuclei in the detector via the strong force, unlike the muons, some pions will deposit more energy into the calorimeters. If a particle "minimally ionizes" in the calorimeter, it should deposit a small and relatively constant amount of energy into the calorimeter that is only dependent on the path length through the calorimeter. This difference between muons and pions led us to make a selection on the amount of energy that is deposited into each calorimeter. The FCAL shower energy for a particle is the total energy of the shower that is correctly matched to the track of that particle. If no matching occurs, this energy is zero. Since the FCAL is perpendicular to the beam, we expect the path length through the FCAL to be relatively constant for all particles traveling through the FCAL. An example of the FCAL energy deposition distribution in data and signal Monte Carlo is shown in the left plot of Figure 4.5. In this plot, the data shows some clear differences from the signal Monte Carlo. The Monte Carlo suggests that there are very few signal events above 1 GeV, while the data has a much larger tail. We expect this large tail in the data to be misidentified pions that are depositing more energy into the FCAL. To determine the cut selection, we again performed a significance analysis on the selection. We found that the signal is maximized at the energy in the FCAL of $\mu^\pm < 1$ GeV, which can be seen in the right plot of Figure 4.5. In the process of analysing this selection, we found a mismodeling of the energy deposition of minimally ionized particles in our Monte Carlo simulations. This will be discussed in more detail in Section 4.4.

4.3.4 Muon/Pion Separation: BCAL Energy Deposition

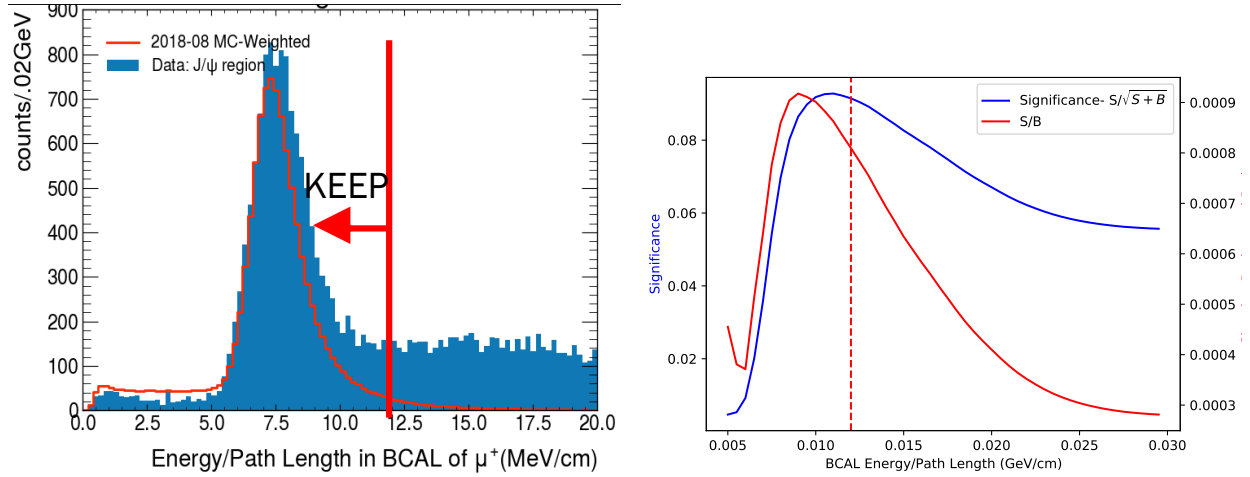


Figure 4.6: (Left) Energy divided by path length in the BCAL distribution in Data and Monte Carlo. This is only in the $M(\mu^+\mu^-)$ region of $M(J/\psi) \pm 3\sigma$. The Monte Carlo is arbitrarily weighted to match heights. The red line represents where the selection was made, and we keep events to the left of that line. (Right) Significance distribution of energy divided by path length in the BCAL. The red dashed line signifies where our selection is made. We chose events with E/PL in BCAL $< .012$ GeV/cm.

The next selection we make to remove background due to misidentified pions is a cut on the energy deposited by the muons in the BCAL. This is very similar to the selection for the FCAL; however, we need to make a modification because of the shape of the BCAL. Since the BCAL is a cylindrical ring (described in more detail in Chapter 3), particles will travel through more material and spend more time in the calorimeter depending on its polar angle. Thus, we normalize the energy deposition of the particle with its path length through the calorimeter, and this quantity should be relatively constant for minimally ionizing particles. To estimate the path length through the material, we use the thickness of the calorimeter and sine of the polar angle in the equation

$$PL \approx \frac{\text{thickness}}{\sin(\theta)} \quad (4.2)$$

If particle is moving perpendicular to the target ($\theta = 90^\circ$), we get the minimum path length equal to the thickness of the BCAL, and as we decrease the polar angle, this path length decreases. This does assume that the particles are moving in straight paths, but this seems to be a good approximation considering the high momentum of these tracks. A clustering algorithm similar to the FCAL is used for the BCAL to get the shower energy, but with the added complexity of the layers and 3D shape of the BCAL [65]. We then match these showers to the tracks, just like

what is done for the FCAL. An example of the BCAL energy deposition divided by path length distribution is shown in the left plot of Figure 4.6. Again, after performing a significance analysis on this selection, we found the signal to be maximized at energy in BCAL divided by path length of $\mu^\pm < .012$ GeV/cm, which can be seen in the right plot of Figure 4.6. In the process of analyzing this selection, we also found a mismodeling of the energy deposition of minimally ionized particles in our Monte Carlo simulations. This will be discussed in more detail in Section 4.4.

4.3.5 Muon/Pion Separation: Baryon Rejection

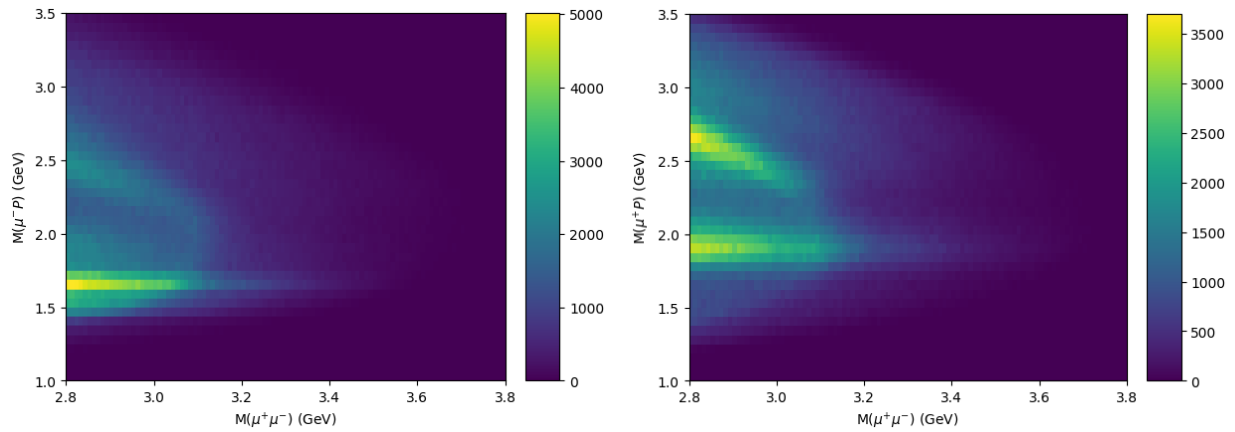


Figure 4.7: The Dalitz plots of the muon-proton ($\mu^\pm p$) mass vs the J/ψ ($\mu^\pm \mu^\mp$) mass. Bands in the muon-proton mass show baryon contributions to the background.

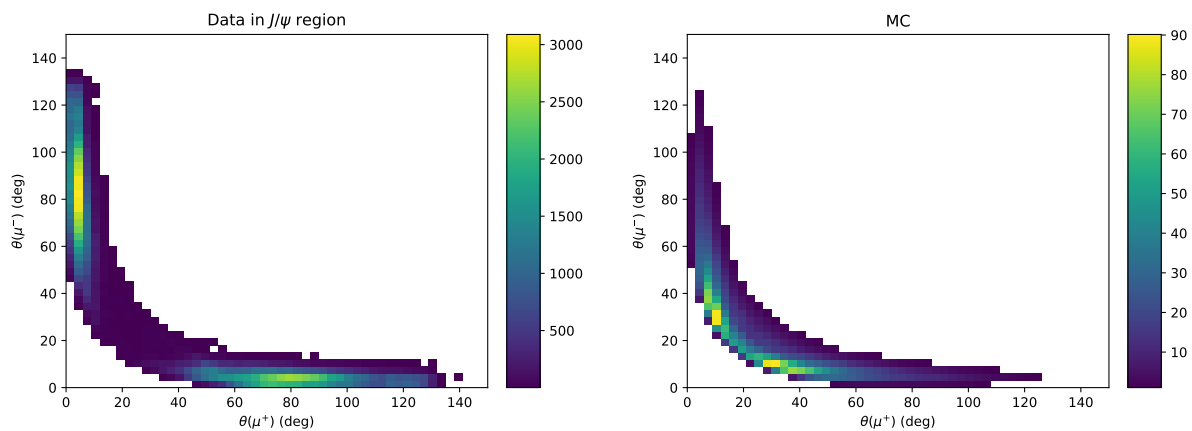


Figure 4.8: The μ^- polar angle versus the μ^+ polar angle for both data in the J/ψ mass region (left) and Monte Carlo (right).

The last selection we make is on the polar angle of the muons in the lab frame. This is because we expect pions that are produced from a baryon decay to have a specific and unique geometry. If a background event were produced from a baryon decay, it would be of t-channel exchange of the form

$$\gamma p \rightarrow \pi^+(N^*/\Delta^0) \rightarrow \pi^+(\pi^- p)$$

or

$$\gamma p \rightarrow \pi^-\Delta^{++} \rightarrow \pi^-(\pi^+ p).$$

Looking at the Dalitz plots in Figure 4.7, the clear bands at 1.9 GeV in μ^+p and 1.6 GeV in μ^-p show clear baryon background at the J/ψ mass of 3.1 GeV. With these baryons at low Mandelstam-t, most of the energy of the photon is transferred into the lone pion, leaving the baryon with lower momentum. In the lab frame, these lower-momentum and slower-moving baryons would then have large theta angles. Thus, the pion that is produced from the baryon will also have a larger theta angle. Figure 4.8 shows the μ^- polar angle versus the μ^+ polar angle for both data (left plot) and Monte Carlo (right plot). The data distribution is predominantly pion background (more than 95%), while the MC shows the expectation for the signal events. In data, we see two peaks from baryon backgrounds where the μ^\pm polar angle is below about 12.5° and the μ^\mp polar angle is between 40° and 140° . However, in MC we see an opposite structure where there is a curved band of events between 10° and 40° with tails stretching out to about 90° . By removing these two peaks coming from baryons, we can significantly reduce our background without removing a significant amount of signal events. To do this, we make a two-dimensional selection where we remove events that have $\theta(\mu^\pm) < 12.5^\circ$ and $\theta(\mu^\mp) > 40^\circ$. To pinpoint which cut maximizes the significance of the signal, we used the same process that we used to find the χ^2/dof cut. The results of this analysis are shown in Figure 4.9. Although we are removing some of our signal with this selection, it is needed because of the significant reduction in our background that we see with it.

4.4 Modeling of Calorimeter Energy Deposition

In the process of working on my analysis of the channel $\gamma p \rightarrow J/\psi p \rightarrow \mu^+\mu^-p$, we saw some inconsistencies between the data and the Monte Carlo simulations. The two selections that led to this calorimeter energy deposition study: Energy in FCAL of $\mu^\pm < 1$ GeV and Energy/ Path Length in BCAL of $\mu^\pm < .012$ GeV/cm, each described in detail above. In this section, we will

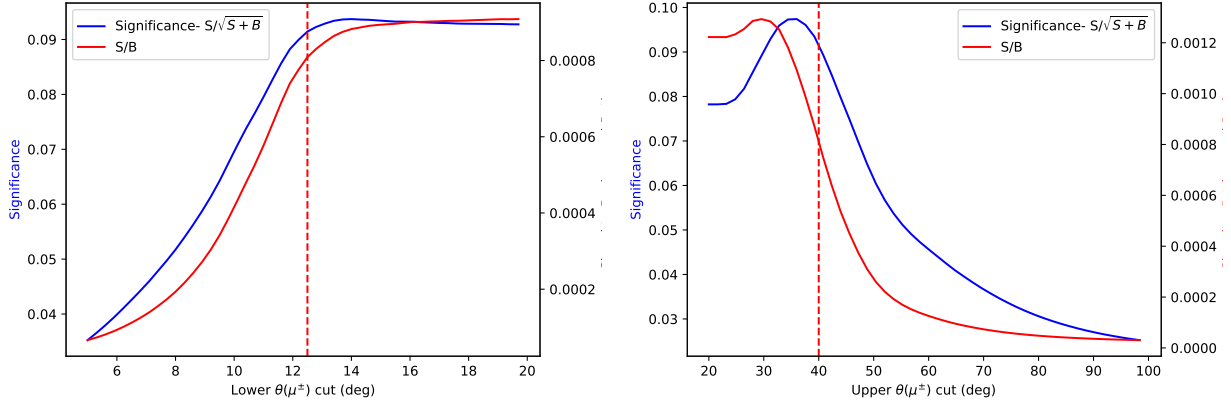


Figure 4.9: (Left) Lower θ of the μ^\pm significance distribution. The red dashed line signifies where our selection was made. (Right) Upper θ of the μ^\mp significance distribution. The red dashed line signifies where our selection was made. We remove events with $\theta(\mu^\pm) < 12.5^\circ$ (lower cut) and $\theta(\mu^\mp) > 40^\circ$ (upper cut).

describe the discrepancies we found, the process we used to fix them, and the final results of the study.

4.4.1 FCAL Energy Deposition

When we began this analysis, the first non-kinematic selection we looked at was the energy deposition in the FCAL. As we described above, this was done to separate muons from pions because the pions can strongly interact with the lead in the calorimeter and deposit more energy than the minimally ionizing muons. When we first looked at the distribution of this FCAL shower energy matched to a muon tracking data and Monte Carlo, we found a couple of major discrepancies, which can be seen in Figure 4.10. The first and most apparent is the two-peak structure that we see in the data but not in Monte Carlo. The second discrepancy we see is that the first peak is shifted down a little in Monte Carlo. We first needed to understand where these structures are coming from, then decide what modifications need to be made to the Monte Carlo simulations, and then implement those modifications to see if there is better matching between data and Monte Carlo.

To understand these structures in data, we began with the work done by our GlueX collaborator, Dr. David Lawrence, and an undergraduate student working under him, Ebode Onyie Fabien. They were studying the pion response in the FCAL. These pions they were looking at were forward-going and have high momentum, so understanding the detection of pions in the FCAL is critical. High-momentum pions (2-4 GeV) that registered a hit in the FCAL were chosen for this study.

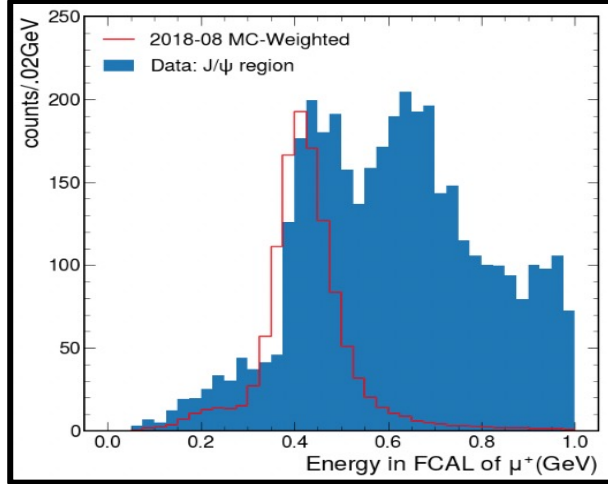


Figure 4.10: FCAL Shower Energy matched to muon track in the $J/\psi \rightarrow \mu^+\mu^-$ channel. The red line is the original Monte Carlo, and the blue is the full Phase-I and 2020 datasets after the non-calorimeter event selections.

Specific channels were not considered. In Figure 4.11, Lawrence and Fabien plotted the projected track position distance from the center of the closest FCAL block (or DOCA- Distance of Closest Approach) versus the energy deposited in that single block. They saw a two-peak structure in the FCAL energy that seemed to peak at approximately 0.42 GeV and 0.65 GeV. Lawrence and Fabien’s result aligns very closely with what we found. However, they also correlate these peaks to positions in the block, with the first peak closer to the edges of the 4 x 4 cm blocks and the second peak more concentrated at the center of the block. They confirmed this by looking at the XY track projection to the back of the FCAL block where the hit was registered for the two peaks separately, shown in Figure 4.12. They also found that the pions in the first peak were mostly around the edges of the block, with the second peak pions concentrated at the center of the block.

This was the first clue into what this second energy peak could be caused by. Lawrence, along with others, thought that this second peak could be due to events that deposit energy into the light guide of the FCAL block module. In Figure 4.13, we see the complete assembly of the FCAL module. Between the optical interface and the PMT, we see a cylindrical light guide. The purpose of this component is to funnel the photons produced in the lead glass block into the PMT with minimal loss. They hypothesized that some pions, those that hit closer to the center of the lead glass crystal, actually interact with these light guides. These pions would deposit more energy than those that interact with just the lead glass block. This would result in two minimally ionizing peaks in the FCAL energy, those minimally ionizing particles just interacting with the lead glass blocks

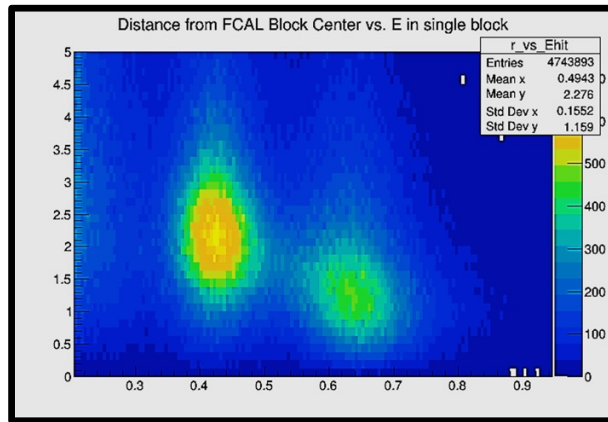


Figure 4.11: David Lawrence and a undergraduate student of his looked at the projected track distance (cm) from center of nearest block (DOCA- Distance of closest approach) versus the energy (GeV) deposited in that nearest block.

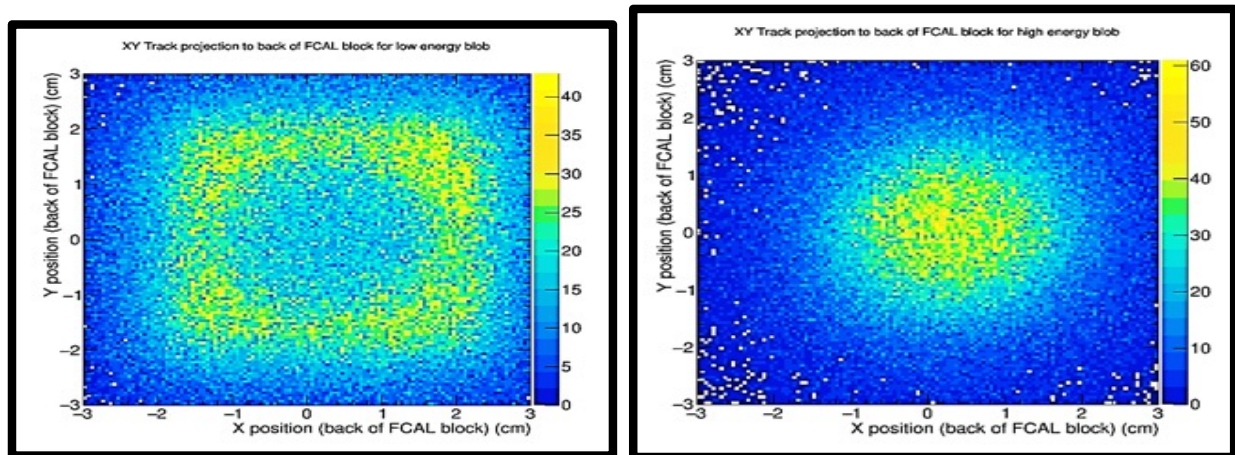


Figure 4.12: (Left) The XY track projection to the back of the FCAL block where the hit was registered, with only events in the lower energy peak. (Right) This same XY track projection to back of the FCAL block but for events in the higher energy peak.

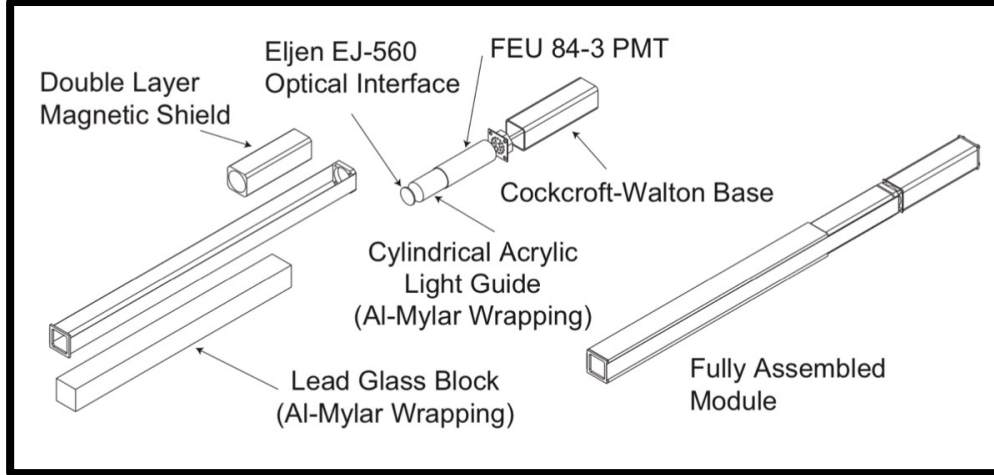


Figure 4.13: Expanded view of a single FCAL module.

(the lower peak) and those particles interacting with both the lead glass block and the light guide (the higher peak).

To validate Lawrence *et al.*'s findings and assess their applicability to our reaction, we required a separate, largely pure samples of pions, muons, and kaons. This would allow us to isolate the effects of each particle type, distinguishing between any potential differences in their behavior. To look at pions and kaons, we chose the $\omega \rightarrow \pi^+\pi^-\pi^0$ and $\phi \rightarrow K^+K^-$ reactions, respectively, because of their large statistics and relatively small background after basic selections. Since the $J/\psi \rightarrow \mu^+\mu^-$ channel has such low statistics and no other channel with muons has been looked at, we chose to use CPP muon data for our FCAL study. The CPP experiment used the GlueX spectrometer, as discussed in chapter 3, along with a new muon detector (located behind the FCAL) to efficiently separate the muon background and to collect a clean sample of muon pairs for the normalization of the experiment. The new muon detector consisted of five layers of multiwire proportional chambers (MWPC) that are separated by iron absorbers. By looking at particles that register hits in all five layers, we have a clean sample of muons that have traveled through the FCAL, exactly what is needed for this study. Since the CPP experiment uses the same detector simulation of the FCAL for their analysis, fixing this discrepancy was also of particular interest to them. For the muons, no exclusive reaction was chosen.

Our initial analysis focused on replicating Lawrence and Fabien's findings for the $\omega \rightarrow \pi^+\pi^-\pi^0$ channel. We examined pions within the 2-4 GeV momentum range, and the resulting FCAL energy distribution, as depicted in Figure 4.14, exhibited a clear two-peak structure. Although the average

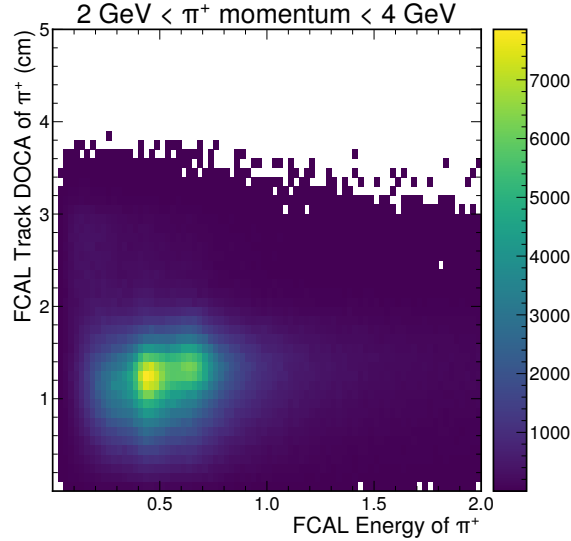


Figure 4.14: The projected track distance from center of nearest FCAL block (DOCA- Distance of closest approach) versus the FCAL energy deposited in that shower. This is for pions with 2-4 GeV in momentum in the $\omega \rightarrow \pi^+\pi^-\pi^0$ channel.

track distance of closest approach (DOCA) for these peaks deviated slightly from their results, the XY projections confirmed the expected spatial distribution: the LG peak was more centrally located, while the MIP peak tended towards the block’s edges. This suggests a discrepancy in the DOCA definition, but it doesn’t significantly impact our conclusions.

We extended our analysis to muons and kaons, examining tracks across all momentum ranges. Figure 4.15 illustrates that both particle types exhibited the same two-peak FCAL shower energy structure.

Next, we confirm the discrepancies between Monte Carlo and data we found in the $J/\psi \rightarrow \mu^+\mu^-$ channel. The results are shown in Figure 4.16. Here we see the Monte Carlo (MC) of all three charged particles have the shifted first peak and no presence of this second peak. We found that our Monte Carlo simulations actually have correction factors that modify the MC to match what is seen in data. Specifically, there is a correction factor for the first minimum ionizing peak and a second correction factor for the light guide (LG) contribution. The latter was set to zero, which is why Monte Carlo did not have this second peak.

Our next objective was to obtain the correct correction factors for both peaks. To do this, we fit both the data and Monte Carlo FCAL energy distributions with two Gaussians to find the two

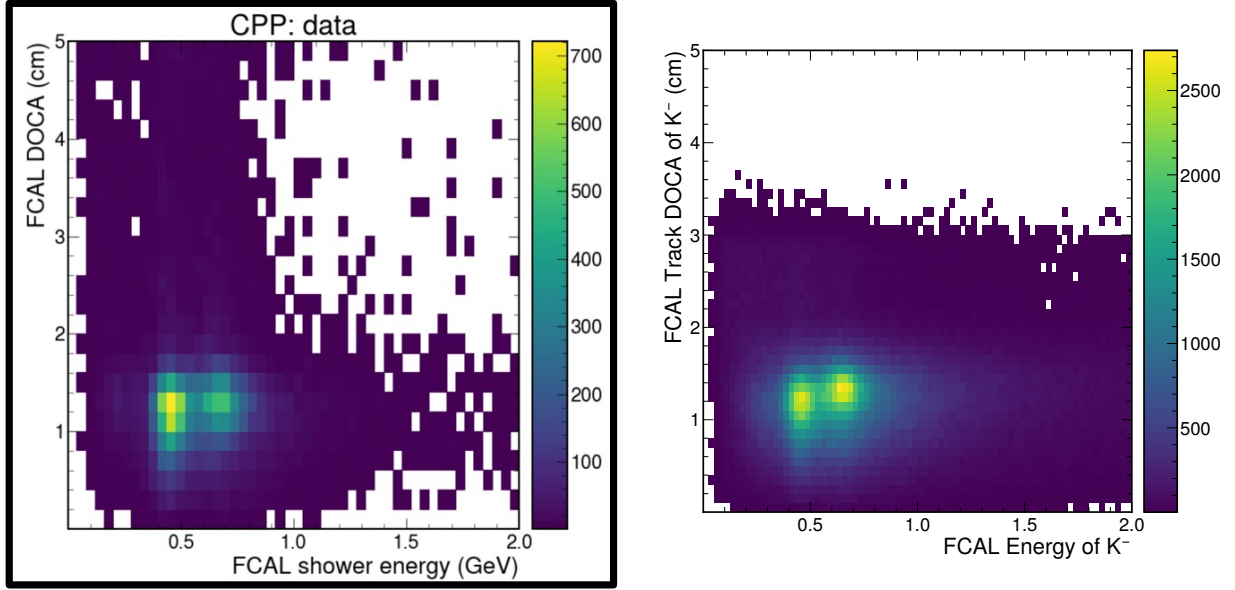


Figure 4.15: The projected track distance from center of nearest FCAL block (DOCA- Distance of closest approach) versus the FCAL energy deposited in that shower. This is done for muons from the CPP experiment (left) and kaons from the $\phi \rightarrow K^+K^-$ channel (right).

peak locations. An example of the fit to the data for the muons, pions, and kaons are shown in Figure 4.17. Since the correction factor for the first peak was already non-zero, we needed to only find the percent increase needed to match the peak locations. We could then apply that percent increase directly to the original factor, giving us the right correction factor. We found that the first peak for all three particles needed to increase 15%. An example of the MC with and without this shift in the first (MIP- Minimally Ionizing Particle) peak for the CPP muons is shown in Figure 4.18.

However, the second correction factor, the one for the light guide (LG) peak, is less straightforward, since it was originally set to zero. To obtain this LG factor, we decided to choose different scale factors and find the mean of the second peak for each scale factor. We then plotted these peak location versus their scale factor and fit a line to this. Using the location of the second peak in data, we can calculate the scale factor that would give us this location. We did this for the CPP muons, the pions in the ω channel, and the kaons in the ϕ channel to see if they find the same correction factor. The linear fits and the correction factor matched to data for each particle is shown in Figure 4.19. There did seem to be a small discrepancy between the muons and the other two particles. We contribute most of this to the fits of the FCAL energy for the pions and kaons. When we compare

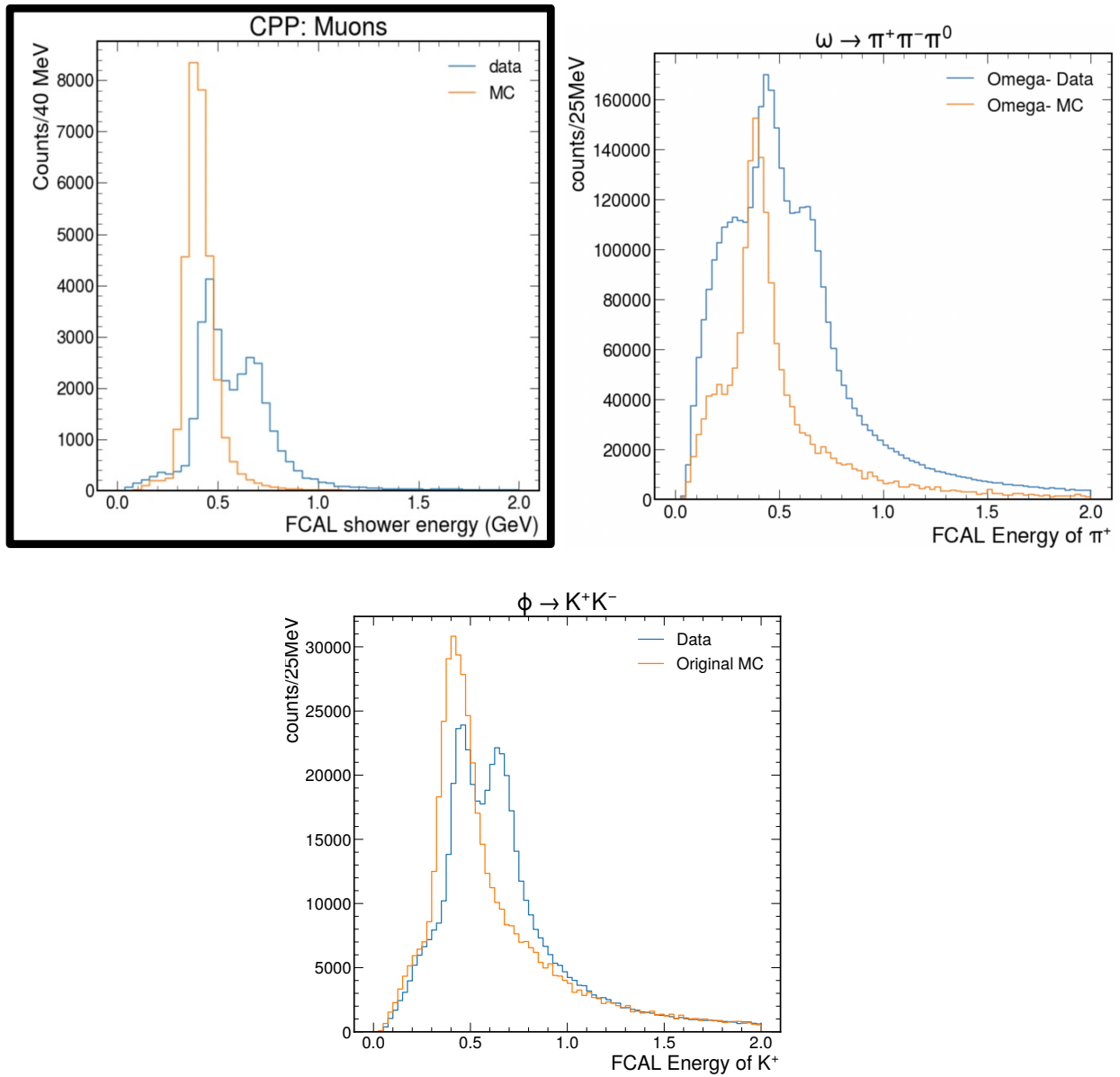


Figure 4.16: FCAL Shower Energy matched to track. The orange line is the original Monte Carlo, and the blue is the data. Top left we have μ^+ from CPP, top right we have π^+ from the $\omega \rightarrow \pi^+ \pi^- \pi^0$ channel, and at the bottom we have K^+ from the $\phi \rightarrow K^+ K^-$ channel.

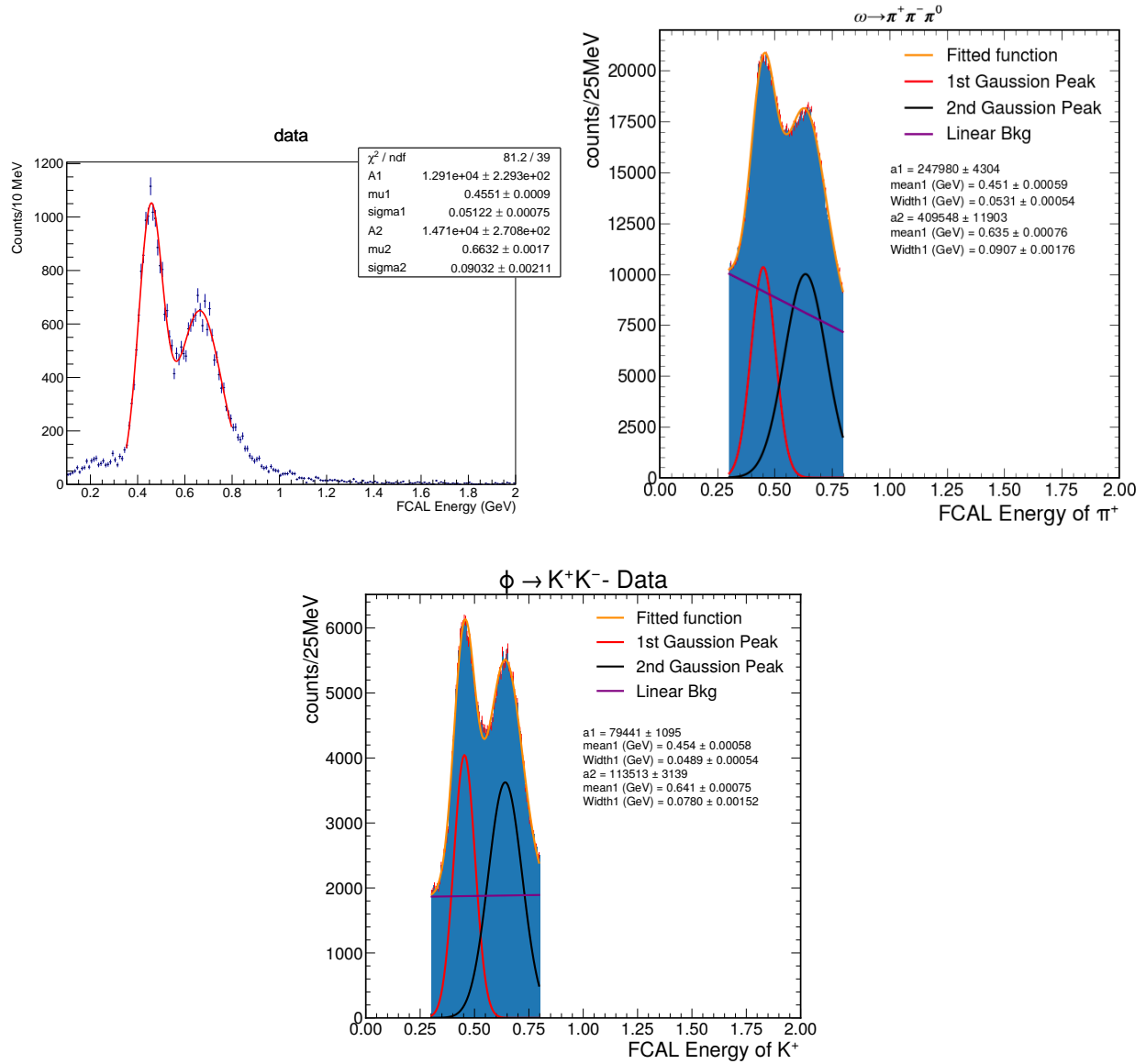


Figure 4.17: Fit of the FCAL Shower Energy matched to tracks using two Gaussians to find the two peak locations. Top left we have μ^+ from CPP data, top right we have π^+ from the $\omega \rightarrow \pi^+ \pi^- \pi^0$ data, and at the bottom we have K^+ from the $\phi \rightarrow K^+ K^-$ data.

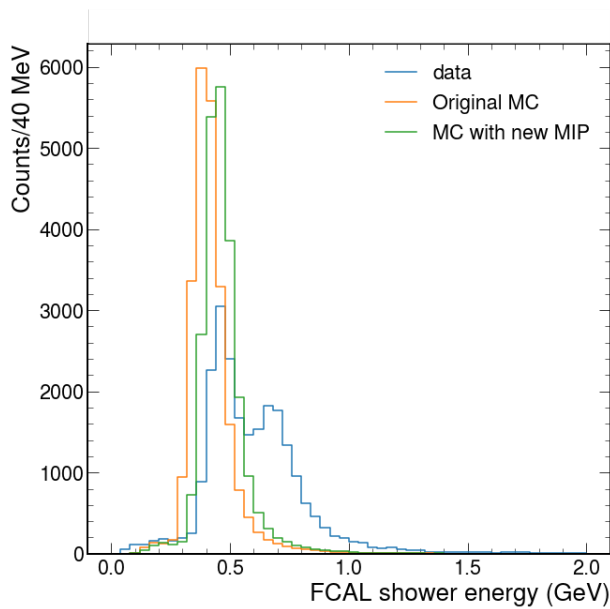


Figure 4.18: FCAL Shower Energy matched to muon track in the CPP data. The orange line is the original Monte Carlo, the green line is with the new MIP factor added, and the blue is the full Phase-I and 2020 datasets after the non-calorimeter event selections.

their distributions to the muons FCAL energy distribution, we see that the muons distribution is cleaner and that the two Gaussian's better describe the muons distribution. The non-Gaussian nature of the pion and kaon distributions, characterized by long tails and irregularities, necessitated the inclusion of a linear background term in our fitting procedure. This background component could have introduced systematic uncertainties into the derived pion and kaon correction factors. Because of this, we chose to use the muons correction factor of 13.5 as the correct value to use in the simulations. The final data and Monte Carlo distributions for all three channels are shown in Figure 4.20. We see much better agreement between the data and Monte Carlo now for all three particles, enough to feel confident in our simulations.

4.4.2 BCAL Energy Deposition

For the BCAL, we look at the shower energy divided by the estimated path length in the BCAL. We do this for similar reasons as for the FCAL, but we have to account for the barrel shape of the BCAL. Depending on the theta angle of the particles in the laboratory frame, the particle could travel at different path lengths in the BCAL. We estimate this path length using the equation: thickness of BCAL (25cm) divided by the sine of the theta angle in the lab frame. The longer the path length in the BCAL, the more energy that we expect the particle to deposit in the BCAL.

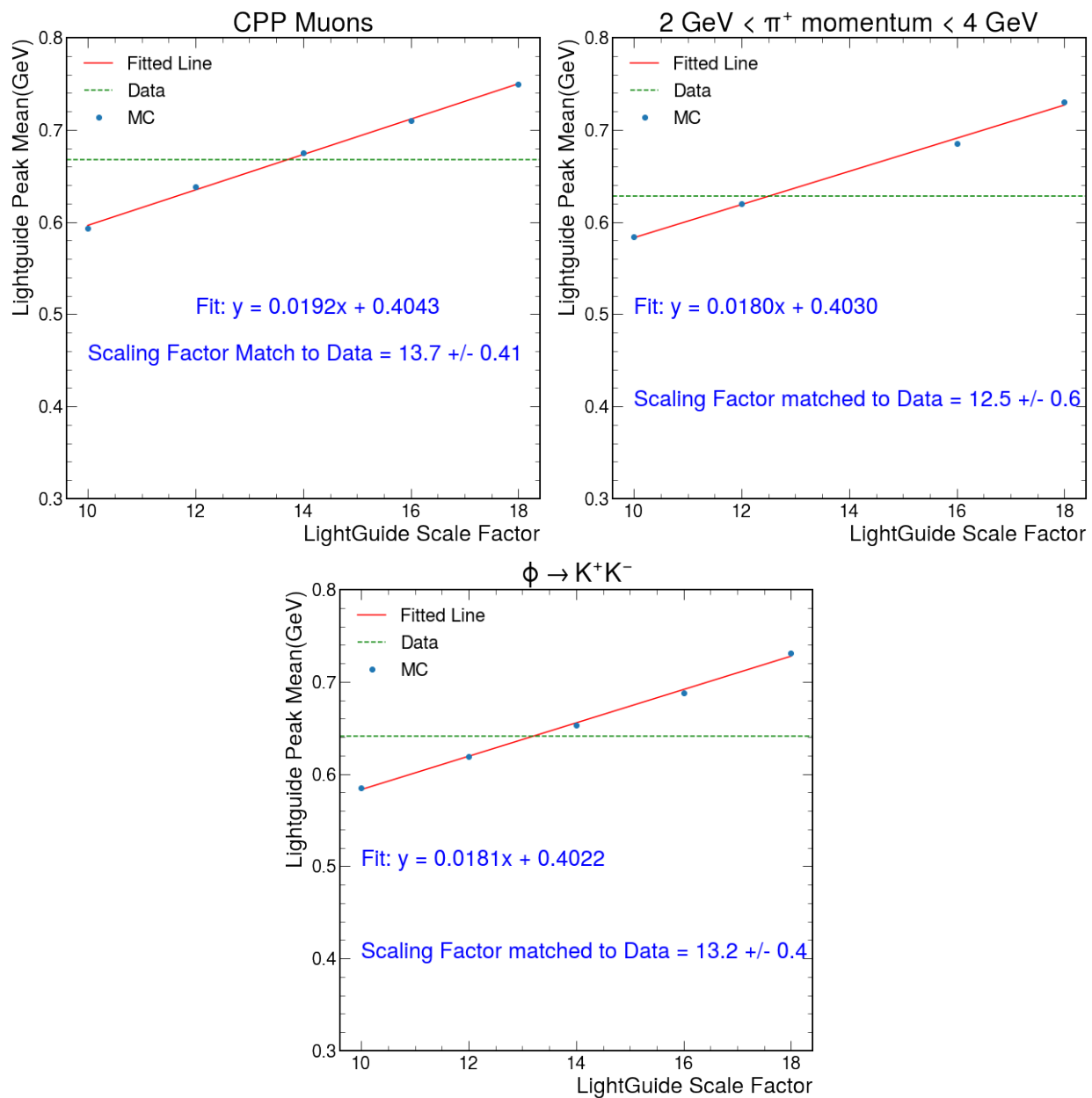


Figure 4.19: The linear fits of light guide peak location versus the correction factor and the light guide correction factor matched to data for each particle. Top left we have μ^+ from CPP data, top right we have π^+ from the $\omega \rightarrow \pi^+\pi^-\pi^0$ channel, and at the bottom we have K^+ from the $\phi \rightarrow K^+K^-$ channel.

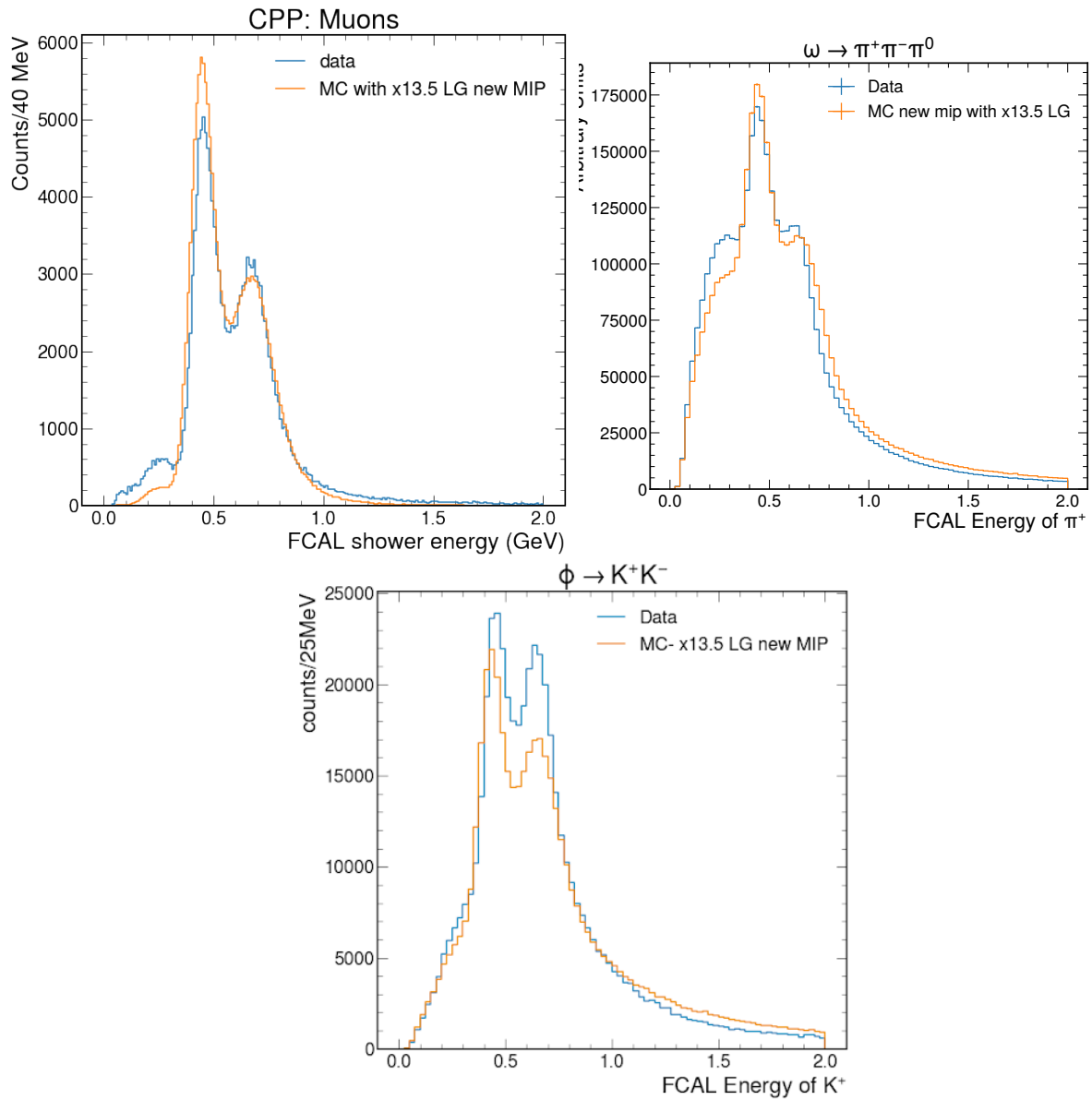


Figure 4.20: FCAL Shower Energy matched to track. The orange line is the new Monte Carlo with the updated correction factors, and the blue is the data. Top left we have μ^+ from CPP data, top right we have π^+ from the $\omega \rightarrow \pi^+\pi^-\pi^0$ data, and at the bottom we have K^+ from the $\phi \rightarrow K^+K^-$ data.

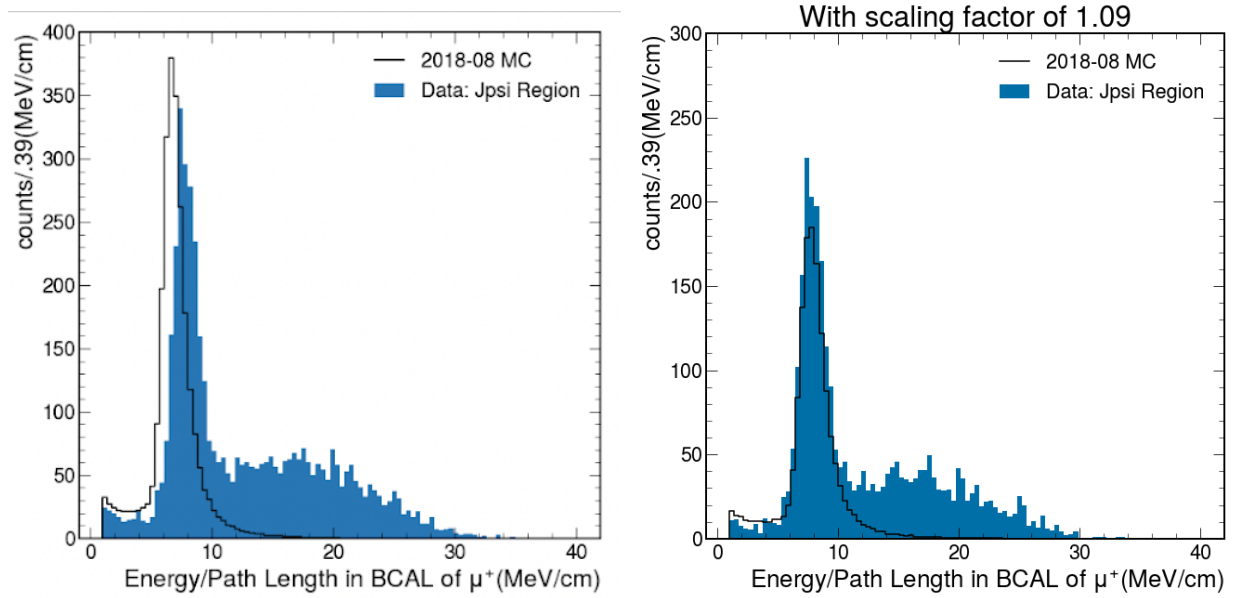


Figure 4.21: (Left) BCAL shower energy deposited by muons divided by the path length in the BCAL for the $J/\psi \rightarrow \mu^+ \mu^-$ data and original Monte Carlo. (Right) Monte Carlo with new shifted MIP peak (x1.09 correction factor).

Because of this effect, we expect the muons BCAL energy over path length to be approximately constant. This can be seen in left plot of Figure 4.21. We see a clear MIP peak in both the data and Monte Carlo, but there is a slight misalignment of those peaks that we need to look into. We attribute the large tail in data to the misidentification of pions as muons, which is the main reason we cut on this variable.

To fix this misalignment, we fit both data and Monte Carlo with Gaussian's to find the peak locations. After fitting both distributions, we find that the data is about 9% higher than the MC peak. If we apply a 1.09 correction factor to MC, we get a much better agreement, which is shown in the right plot of Figure 4.21.

For a comparison, we looked at some of the cosmic runs, which are runs taken with the photon beam off. Since this is a relatively clean sample of muons from cosmic rays going through the BCAL, this gave us something to cross examine our results. However, to calculate the path length, we cannot use the same method as before. This is because we do not have the same tracking information as with the normal runs, since cosmic muons do not necessarily go through the FDC and CDC. To estimate the path length, we use a method similar to that used by our GlueX collaborator Zizis Papandreou and others at the University of Regina used for some BCAL calibrations. In the cosmic

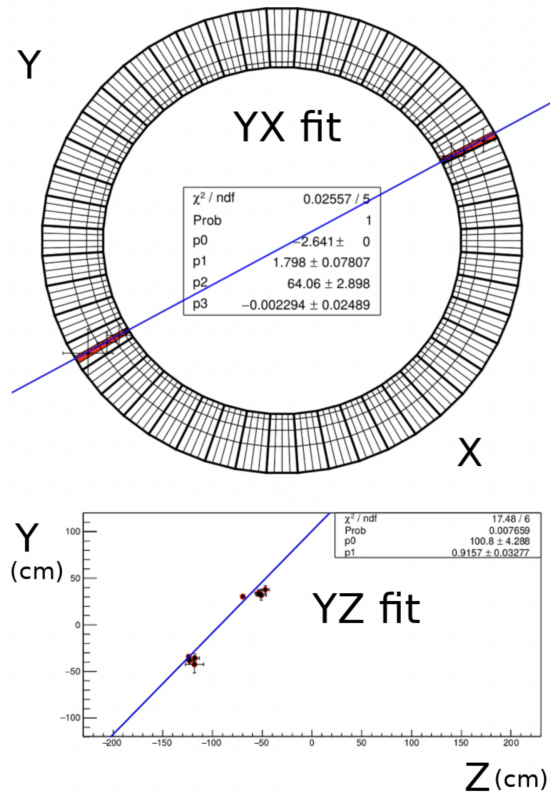


Figure 4.22: XY projection (top) and YZ projection (bottom) of an accepted cosmic event.

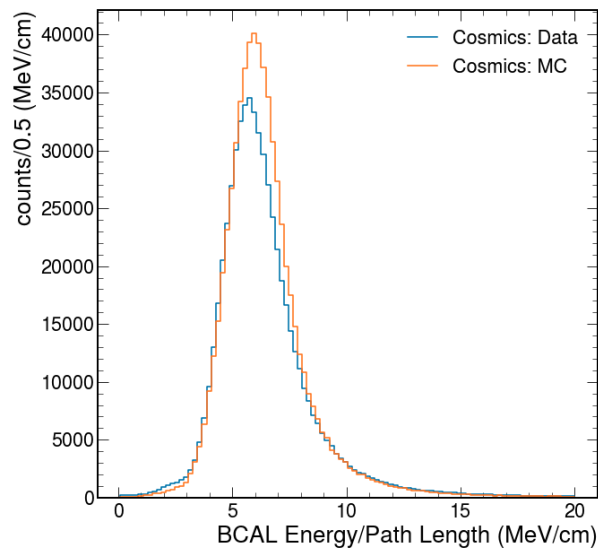


Figure 4.23: BCAL shower energy deposited by muons divided by the path length in the BCAL for the cosmics data and original MC.

run data, we have the position (x,y,z) and energy deposition for a hit in each of the four layers of the BCAL. We first require that an event must go through both sides of the BCAL, having 8 total hits. We then take this hit position information and fit two lines, one in the XY-plane and one in the YZ-plane. We used the slope and y-intercept of each fit plus the inner and out radius of the BCAL to determine the path length of the muon through the BCAL. An example of these fits can be seen in Figure 4.22. With this method of finding the path length, the BCAL energy / path length distribution for the cosmic data and the original MC can be seen in Figure 4.23. We see a slight difference in peak locations, but this effect is much smaller than what is seen in the $J/\psi \rightarrow \mu^+\mu^-$ channel ($\approx 5\%$ versus $\approx 9\%$ difference). The discrepancy we're observing in the J/ψ channel likely stems from our approximation that the muon path is straight in the BCAL. As the solenoid magnetic field is off during cosmic runs, this path length assumption is more accurate. However, during normal runs with the magnetic field on, this approximation may introduce systematic errors in the path length calculation. We seem to actually be modeling the energy deposition in the BCAL quite well, as shown by the cosmic runs. Because of this, we chose to artificially adjust the BCAL energy/path length value in the J/ψ MC and cut on this adjusted value. We left the simulation of the BCAL energy as is.

4.5 Summary of Event Selections

A summary of our event selection is given in Table 4.4, where we list the efficiency of the cut and the signal-to-background ratio of the selection.

Table 4.4: A list of the event selections we used, their relative efficiencies, and the cumulative signal to background ratio when that selection and above is applied.

Event Selection	Eff. (%)	Cumulative Sig./Bkg
Loose Initial Selections	34.4	0.0006053
$\chi^2/dof < 5$	63.4	0.005879
Energy/Path Length in BCAL of $\mu^\pm < .012$ GeV/cm	94.5	0.0344
FCAL Energy of $\mu^\pm < 1.0$ GeV	88.0	0.03886
$\theta(\mu^\pm) < 12.5^\circ$ and $\theta(\mu^\mp) > 40^\circ$	78.7	0.3928
Total	14.4	0.3928

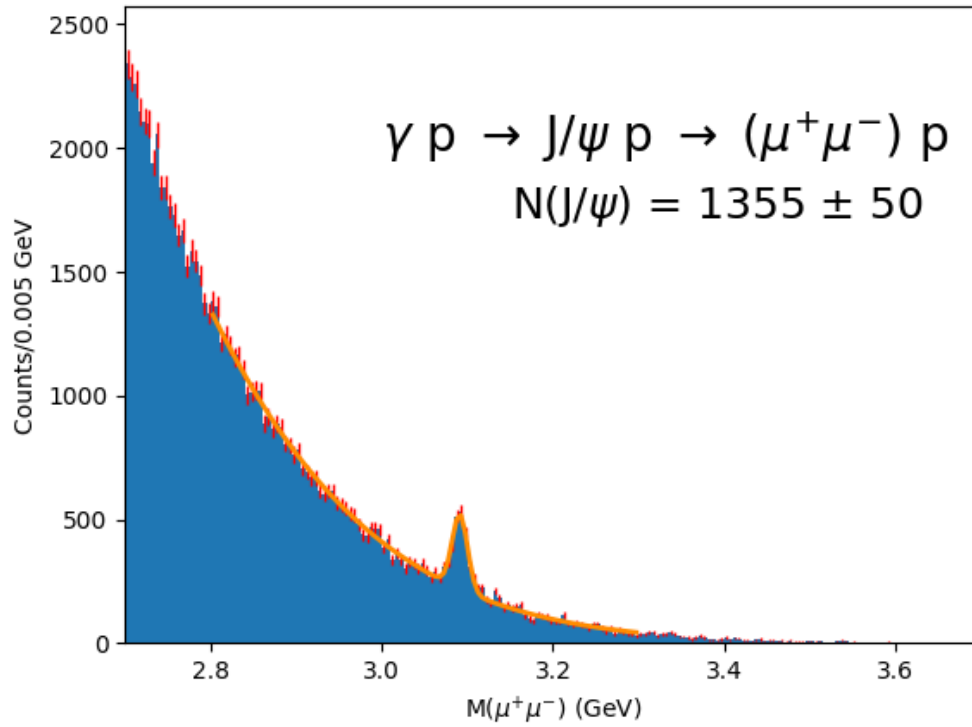


Figure 4.24: The $\mu^+\mu^-$ mass spectra after all selections are applied. It is fit with a Gaussian peak and background of the form $e^{A+Bx+Cx^2}$. We get 1355 ± 50 J/ψ events with a mass of 3.091 ± 0.0035 GeV and a width of 0.0089 ± 0.00041 GeV.

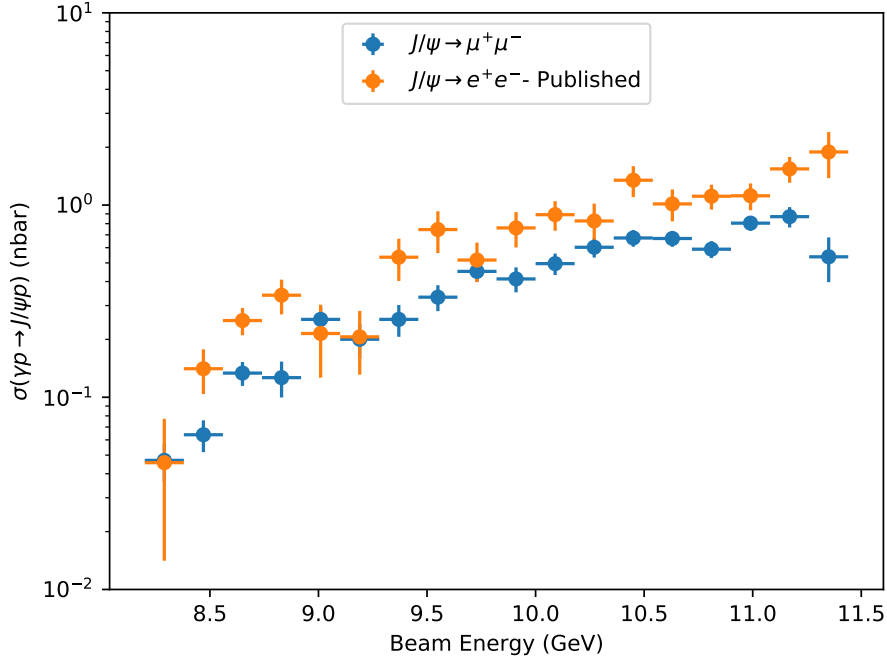


Figure 4.25: The filled blue points show the measured total cross sections obtained from Eq. 4.4 in fine photon energy bins. The error bars represent the statistical errors. The filled orange points represent the GlueX published [34] cross sections from the $J/\psi \rightarrow e^+e^-$ channel, with the error bars representing the statistical and systematic uncertainties added in quadrature.

4.6 The Mass Spectra and Cross Section of $J/\psi \rightarrow \mu^+ \mu^-$

Applying all the selections above, we get the final $\mu^+ \mu^-$ mass spectra shown in figure 4.24. It is fit with a Gaussian peak and background of the form $e^{A+Bx+Cx^2}$. We get 1355 ± 50 J/ψ events with a mass of 3.091 ± 0.0035 GeV and a width of 0.0089 ± 0.00041 GeV. The uncertainties are determined from MINUIT.

We measured the total cross section of the reaction $\gamma p \rightarrow J/\psi p$ through the decay $J/\psi \rightarrow \mu^+ \mu^-$ using the equation:

$$\sigma(\gamma p \rightarrow J/\psi p) = \frac{N_{J/\psi}(E_\gamma)}{\mathcal{L}(E_\gamma)\epsilon(E_\gamma)Br(J/\psi \rightarrow \mu^+ \mu^-)}, \quad (4.3)$$

where $N_{J/\psi}$ is the J/ψ yield taken from mass spectrum fits, \mathcal{L} is the luminosity of the photon beam, ϵ is the estimated efficiency of the GlueX detector from Monte Carlo simulations, and $Br(J/\psi \rightarrow \mu^+ \mu^-)$ is the branching ratio taken from the PDG [1]. The results of the measurement can be seen in Figure 4.25. The filled blue points show the measured total cross sections obtained

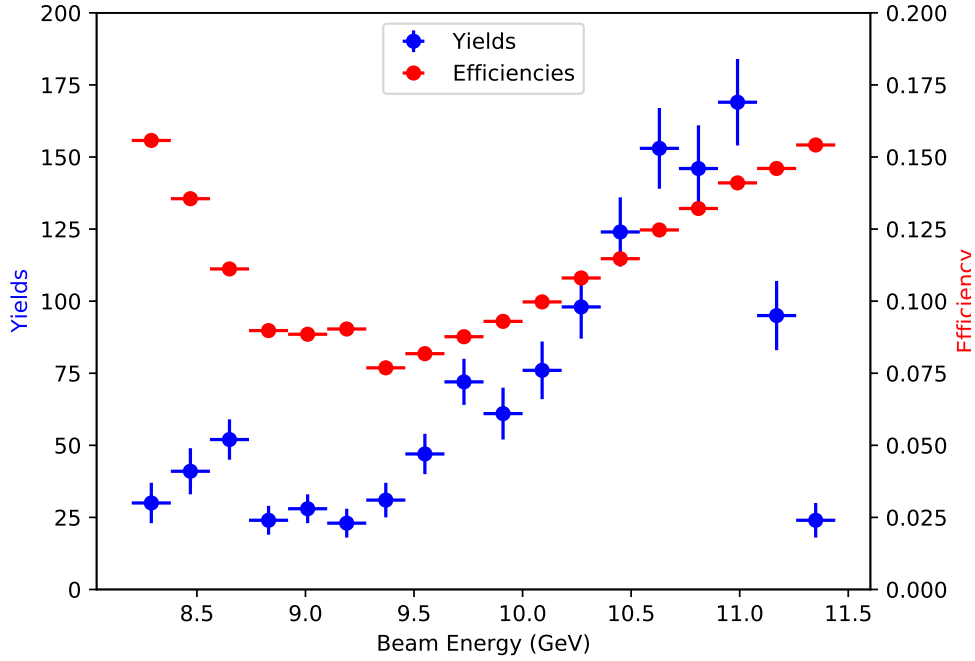


Figure 4.26: The filled blue points show the J/ψ yields obtained from the mass fits shown in appendix A. The error bars represent the statistical errors. The filled red points represent the estimated efficiencies from Monte Carlo simulations.

from Eq. 4.4 in fine photon energy bins. The error bars represent the statistical errors, calculated using MINUIT. The filled orange points represent the GlueX published [34] cross sections from the $J/\psi \rightarrow e^+e^-$ channel, with the error bars representing the statistical and systematic uncertainties added in quadrature. In Figure 4.26, we plot the J/ψ yields (shown in blue) obtained from the mass fits shown in appendix A and the estimated efficiencies (shown in red) from Monte Carlo simulations. We use a Gaussian with a fixed width plus a background curve to fit the mass spectrum. The width chosen for each energy bin is given by the fits to the Monte Carlo mass spectrum for each energy bin. Because the J/ψ width is so small (92.6 ± 1.7 keV [1]), the width of the peak comes from the resolution of the GlueX detector. The background curve for the first two energy bins is linear ($A+Bx$) and for the last 16 energy bins is of the form $e^{A+Bx+Cx^2}$. This done because of the large difference in shapes for the energy bins near threshold.

We also measured the differential cross section of the reaction $\gamma p \rightarrow J/\psi p$ through the decay $J/\psi \rightarrow \mu^+\mu^-$. Because the flux varies greatly with each E_γ - t bin, shown in Figure 4.27, we weight each event by the measured luminosity in 45 MeV bins. We fit the weighted $M(\mu^+\mu^-)$ distribution

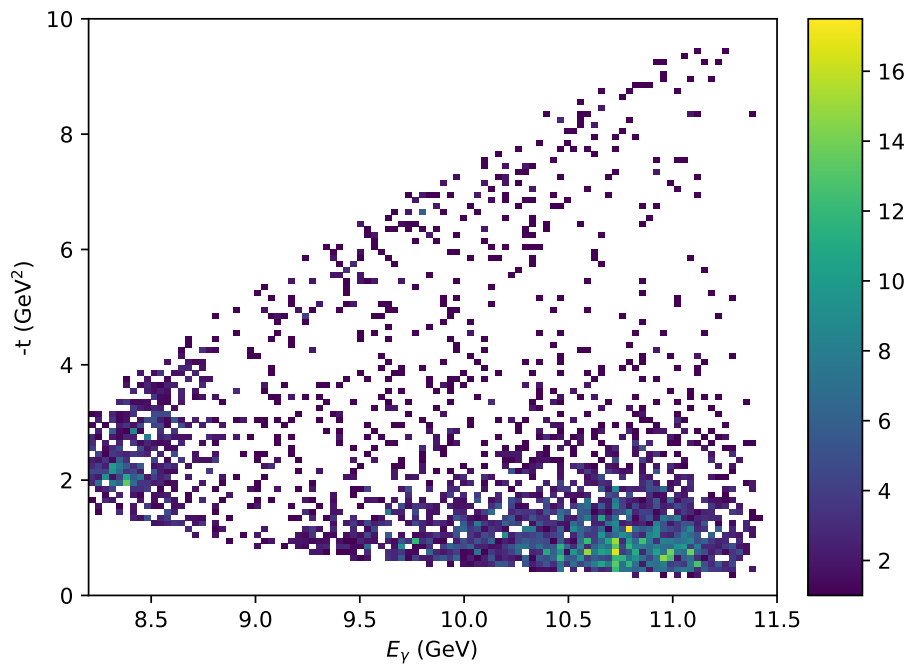


Figure 4.27: The distribution of events data in the E_γ - t plane. A mass selection of $3.05 \text{ GeV} < M(\mu^+\mu^-) < 3.15 \text{ GeV}$ is used for the events in this plot.

to determine the luminosity weighted yield, $N_{wt}^{J/\psi}(E_\gamma, t)$, in bins of E_γ and t . This is a similar process to what was done for the published $J/\psi \rightarrow e^+e^-$ GlueX results [34]. To calculate the differential cross section, we use the equation:

$$\frac{d\sigma(\gamma p \rightarrow J/\psi p)}{dt} = \frac{N_{wt}^{J/\psi}(E_\gamma, t)}{a(E_\gamma, t)\epsilon(E_\gamma, t)Br(J/\psi \rightarrow \mu^+\mu^-)}, \quad (4.4)$$

where $a(E_\gamma, t)$ is the area of the given E_γ - t bin, ϵ is the estimated efficiency of the GlueX detector from Monte Carlo simulations, and $Br(J/\psi \rightarrow \mu^+\mu^-)$ is the branching ratio taken from the PDG [1]. We calculate the area of each bin using Monte Carlo by generating a uniform distribution over the whole rectangular plane shown in Figure 4.27 and determining what fraction is kept within the kinematically available space. The measured differential cross section can be seen in Figure 4.28.

4.6.1 High Mandelstam- t events

By comparing the e^+e^- and $\mu^+\mu^-$ differential cross sections, a clear deviation a low- t seems to occur, with $\mu^+\mu^-$ differential cross section to be lower than e^+e^- differential cross section considering the log scale. As discussed in chapter 1, the region of interest is in the high ξ region, where factorization is more applicable. This equates to the low beam energy and high- t region. Because of this, we chose to look at only high- t ($-t > 1.5 \text{ GeV}^2$) events. The results are shown in Figure 4.29. By making this cut on t , we see a reduction in yields by over half; however, the agreement between the e^+e^- and $\mu^+\mu^-$ total cross sections becomes better, especially in the middle three beam energy bins. This is the final selection made.

4.7 Estimating Systematic Uncertainties

Using the aforementioned selection criteria, including $-t > 1.5 \text{ GeV}^2$, we use the following test to estimate the systematic uncertainties. To do this, we examine three categories of systematic tests: event selection variations, yield systematic tests, and other systematics.

4.7.1 Event Selections

To gauge the stability of our cross section measurement due to variations in event selection, we follow the methodology suggested by R. Barlow [66]. The new values for each variation are then compared to the nominal cross section values by calculating the Barlow criteria

$$\frac{\Delta_B}{\sigma_{\text{Barlow}}} = \frac{x_{\text{nominal}} - x_{\text{variation}}}{\sqrt{|\sigma_{\text{nominal}}^2 - \sigma_{\text{variation}}^2|}} \quad (4.5)$$

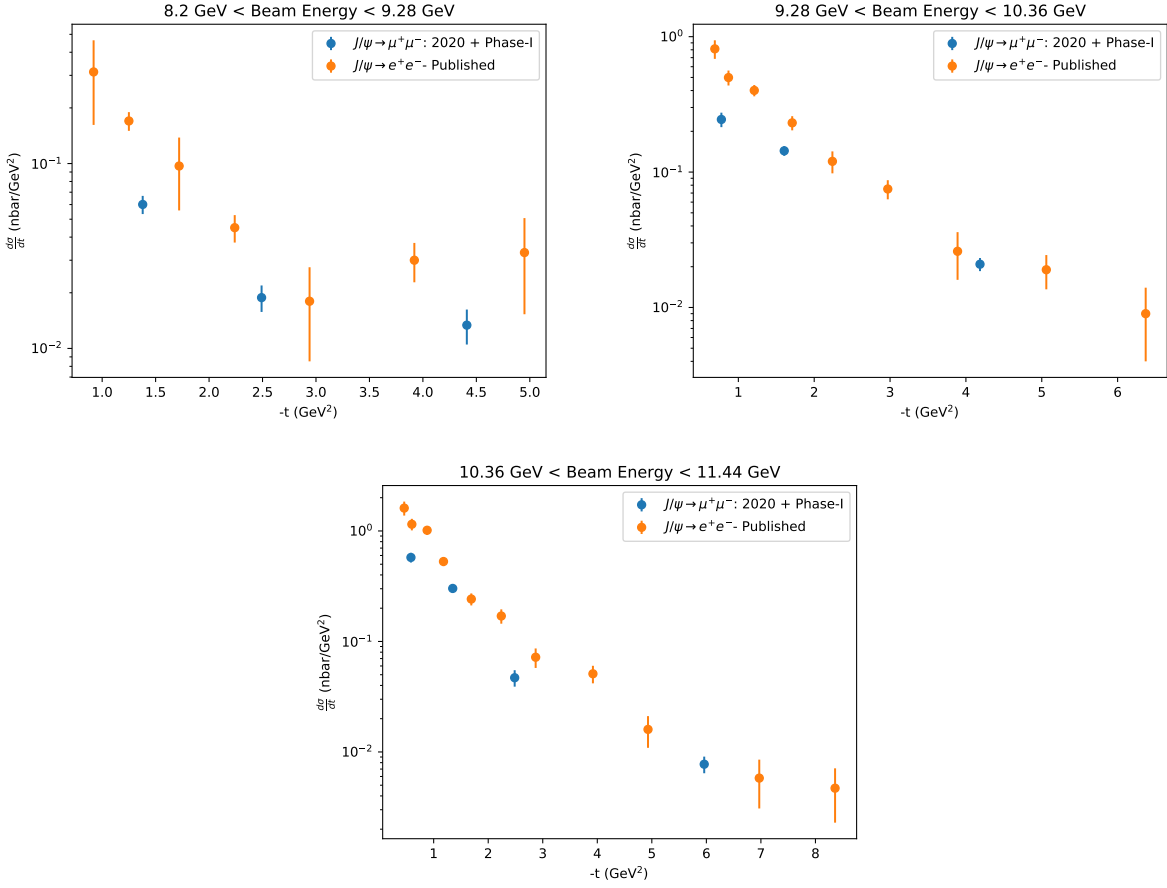


Figure 4.28: Comparison of the differential cross sections for the three energy regions from this work to the measurements of the published $J/\psi \rightarrow e^+e^-$ GlueX results [34]. The error bars for the blue points ($J/\psi \rightarrow \mu^+\mu^-$) only represent statistical uncertainties, while the error bars for the orange points ($J/\psi \rightarrow e^+e^-$) represent both statistical and systematic uncertainties added in quadrature.

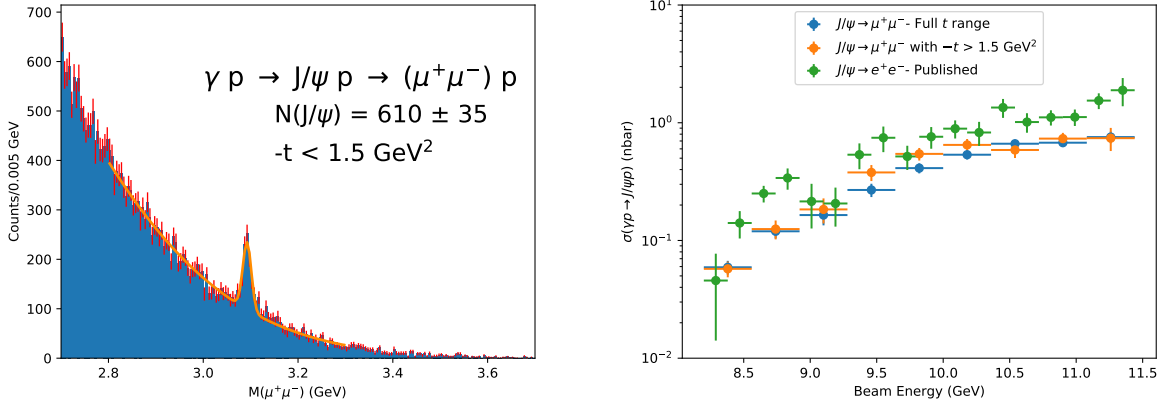


Figure 4.29: (left) The $\mu^+\mu^-$ mass spectra only for events with $-t > 1.5 \text{ GeV}^2$. It is fit with a Gaussian peak and background of the form $e^{A+Bx+Cx^2}$. We get 6105 ± 35 J/ψ events with a mass of $3.0925 \pm 0.0005 \text{ GeV}$ and a width of $0.0089 \pm 0.0007 \text{ GeV}$. (right) The filled blue points show the measured total cross sections obtained from Eq. 4.4 for the full t -range. The error bars represent only the statistical errors. The filled orange points show the measured total cross sections obtained from Eq. 4.4 for $-t > 1.5 \text{ GeV}^2$. The error bars represent only the statistical errors. The filled green points represent the GlueX published [34] cross sections from the $J/\psi \rightarrow e^+e^-$ channel, with the error bars representing the statistical and systematic uncertainties added in quadrature.

where x_i and σ_i are the cross section values and uncertainties for the nominal and varied data sets, and $\sigma_{\text{Barlow}} = \sqrt{|\sigma_{\text{nominal}}^2 - \sigma_{\text{variation}}^2|}$. The Barlow criteria are calculated using uncertainties obtained from MINUIT. Variations that give a $|\Delta_B| < \sigma_{\text{Barlow}}$ are not considered significant. If a variation consistently gives $|\Delta_B| > 4\sigma_{\text{Barlow}}$ then it must be included as a systematic uncertainty. Cases that sit in the middle are evaluated more carefully.

We begin by looking at the χ^2/NDF selection, where the nominal is $\chi^2/\text{NDF} < 5$. We vary the selection from $\chi^2/\text{NDF} < 3$ to $\chi^2/\text{NDF} < 8$ in steps of 1. The variations in the cross section can be seen in the left plot in Figure 4.30, while the Barlow significance for each variation can be seen in the right plot. According to the Barlow test, the χ^2/NDF selection does have some meaningful effect on the cross section measurement. Because of this, we give a bin-by-bin systematic uncertainty for this selection depending on the differences of the central values from the nominal. A list of these systematic uncertainties is given in table 4.5.

We then looked at the Energy/Path Length in BCAL of μ^\pm selection, where the nominal is 12 MeV/cm. We varied the selection from 10 MeV/cm to 16 MeV/cm in steps of 2 MeV/cm. The variations in the cross section can be seen in the left plot in Figure 4.31, while the Barlow significance for each variation can be seen in the right plot. According to the Barlow test, the

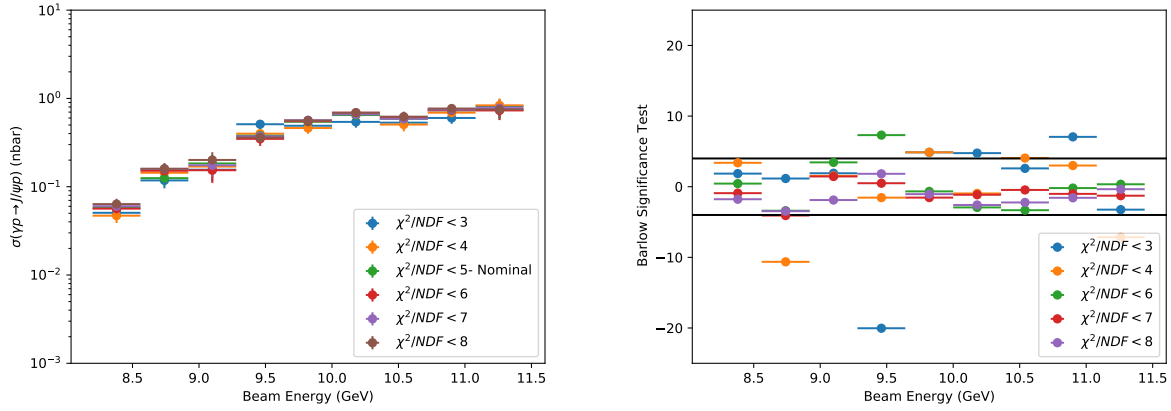


Figure 4.30: (left) Total cross section measurement for variations of the χ^2/NDF selection. We varied the selection from $\chi^2/NDF < 3$ to $\chi^2/NDF < 8$ in steps of 1, where the nominal is $\chi^2/NDF < 5$. (right) The Barlow significance test for each variation from the nominal.

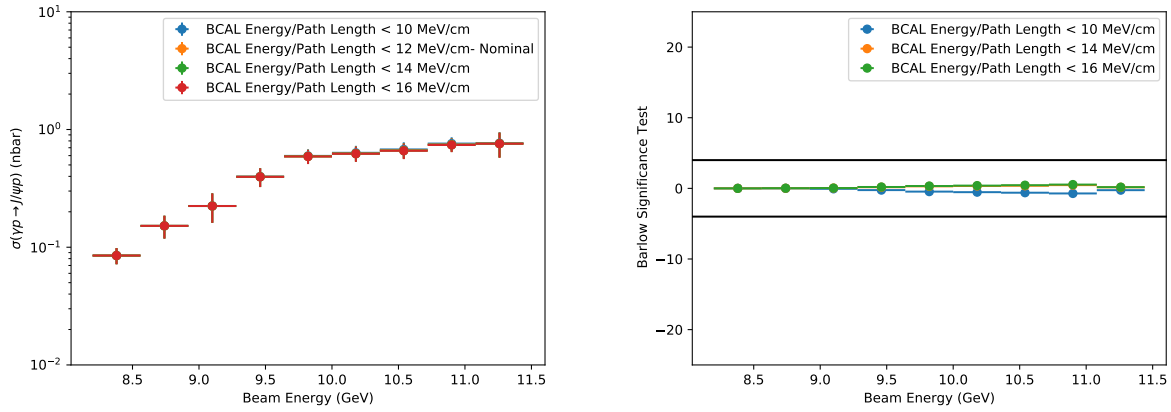


Figure 4.31: (left) Total cross section measurement for variations of the Energy/Path Length in BCAL of μ^\pm selection. We varied the selection from 10 MeV/cm to 16 MeV/cm in steps of 2 MeV/cm, where the nominal is 12 MeV/cm. (right) The Barlow significance test for each variation from the nominal.

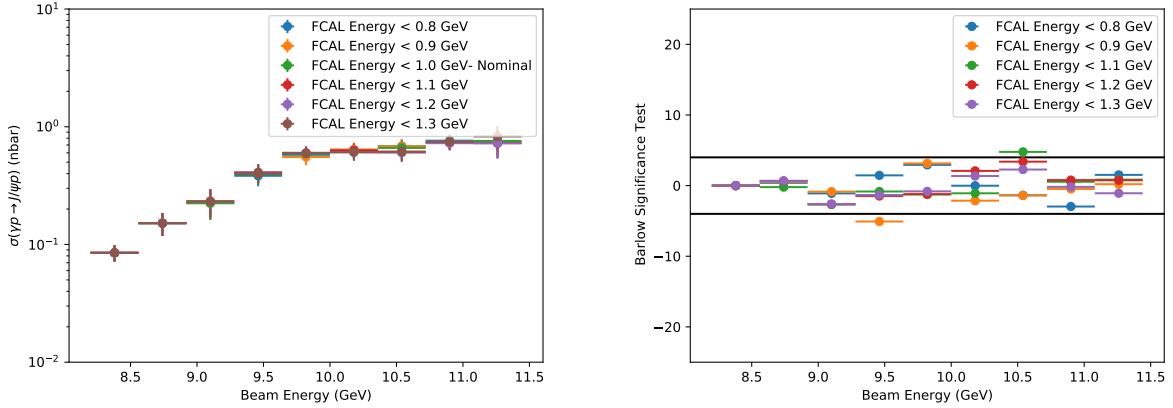


Figure 4.32: (left) Total cross section measurement for variations of the Energy in FCAL of μ^\pm selection. We varied the selection from 0.8 GeV to 1.3 GeV in steps of 0.1 GeV, where the nominal is 1.0 GeV. (right) The Barlow significance test for each variation from the nominal.

Energy/Path Length in BCAL of μ^\pm selection does not have a meaningful effect on the cross section measurement.

We then looked at the Energy in FCAL of μ^\pm selection, where the nominal is 1.0 GeV. We varied the selection from 0.8 GeV to 1.3 GeV in steps of 0.1 GeV. The variations in the cross section can be seen in the left plot in Figure 4.31, while the Barlow significance for each variation can be seen in the right plot. According to the Barlow test, the Energy in FCAL of μ^\pm selection does not have a meaningful effect on the cross section measurement.

We then looked at the 2D $\theta(\mu^\pm)$ selection, where the nominal is $\theta(\mu^\pm) < 12.5^\circ$ and $\theta(\mu^\mp) > 40^\circ$. We varied the lower θ selection from 10.5° to 14.5° in steps of 1° , while we vary the upper θ selection from 30° to 50° in steps of 5° . Since the $\theta(\mu^\pm)$ selection is a 2D selection, we keep one constant and vary the other. The variations in the cross section for the lower θ selection can be seen in the left plot in Figure 4.33, while the Barlow significance for these variations can be seen in the right plot. The variations in the cross section for the upper θ selection can be seen in the left plot in Figure 4.34, while the Barlow significance for these variations can be seen in the right plot. According to the Barlow test, the θ selection does have some meaningful effect on the cross section measurement. Because of this, we give a bin-by-bin systematic uncertainty for this selection depending on the differences of the central values from the nominal. A list of these systematic uncertainties is given in table 4.5.

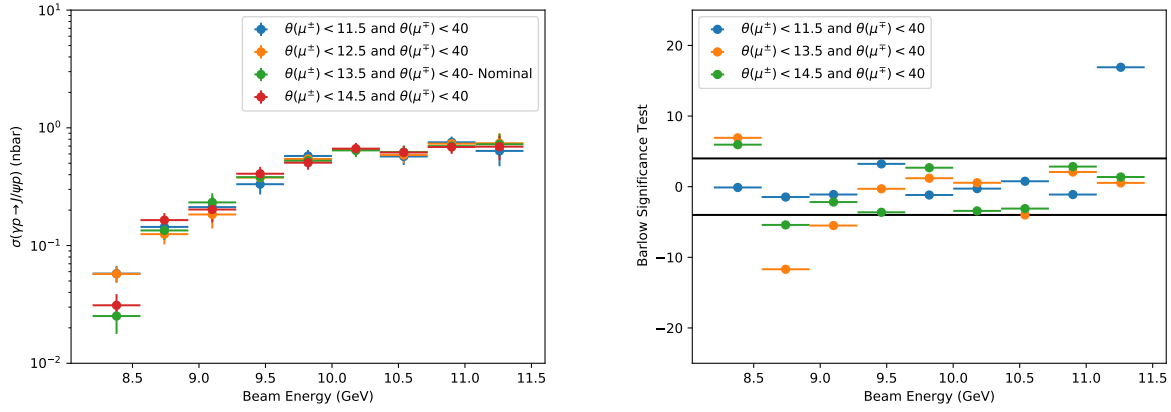


Figure 4.33: (left) Total cross section measurement for variations of the lower $\theta(\mu^\pm)$ selection. Since the $\theta(\mu^\pm)$ selection is a 2D selection, we keep one constant and vary the other. We varied the selection from 10.5° to 14.5° in steps of 1° , where the nominal is 12.5° . The upper $\theta(\mu^\pm)$ selection is kept constant at 40° . (right) The Barlow significance test for each variation from the nominal.

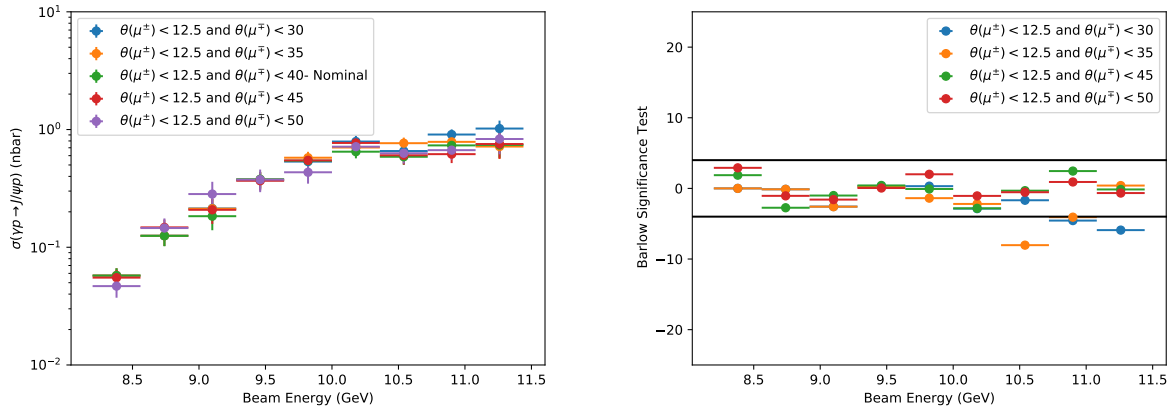


Figure 4.34: (left) Total cross section measurement for variations of the upper $\theta(\mu^\pm)$ selection. Since the $\theta(\mu^\pm)$ selection is a 2D selection, we keep one constant and vary the other. We varied the selection from 30° to 50° in steps of 5° , where the nominal is 40° . The lower $\theta(\mu^\pm)$ selection is kept constant at 40° . (right) The Barlow significance test for each variation from the nominal.

Table 4.5: A list of systematic errors in each energy bin due to the given event selections. From Barlow test, the calorimeter energy selection variations were not significant enough for a systematic uncertainty.

Energy Bin (GeV)	χ^2/NDF Cut	Low θ Cut	High θ Cut
8.20 - 8.56	± 0.010 nb	± 0.032 nb	± 0.011 nb
8.56 - 8.92	± 0.035 nb	± 0.040 nb	± 0.023 nb
8.92 - 9.28	± 0.030 nb	± 0.049 nb	± 0.100 nb
9.28 - 9.64	± 0.132 nb	± 0.046 nb	± 0.011 nb
9.64 - 10.00	± 0.082 nb	± 0.038 nb	± 0.110 nb
10.00 - 10.36	± 0.106 nb	± 0.017 nb	± 0.143 nb
10.36 - 10.72	± 0.081 nb	± 0.035 nb	± 0.179 nb
10.72 - 11.08	± 0.132 nb	± 0.046 nb	± 0.174 nb
11.08 - 11.44	± 0.095 nb	± 0.103 nb	± 0.280 nb

4.7.2 Yield Systematics

An important systematic to study is the methods used for yield extraction. We do this by looking at three systematics of the mass fits: the background function, the fit range, and the fixed width. Besides the nominal background function of $e^{A+Bx+Cx^2}$, we use background functions $A + Bx + Cx^2 + Dx^3$ and $e^{A+Bx+Cx^2+Dx^3}$. Since The results can be seen in the top left plot of Figure 4.35. Besides the nominal fit range of 2.95 GeV - 3.2 GeV, we vary the fit range from 2.8 GeV - 3.35 GeV to 3.0 GeV - 3.15 GeV in steps of 0.05 GeV. The results can be seen in the top right plot in Figure 4.35. We use a fixed width from Monte Carlo to fit the J/ψ mass distribution for the nominal fits. For the variation, we find a scale factor between data and Monte Carlo of the widths for the full beam energy range. We found this by fitting the mass spectrum for the full beam energy in both data and Monte Carlo, using a Gaussian to describe the J/ψ peak. The data width was 1.4 times bigger than Monte Carlo. We then use the width from Monte Carlo for each energy bin multiplied by 1.4. The results can be seen in the bottom plot of Figure 4.35. Since we are not varying the data sample, each variation from the nominal is significant. Because of this, we get a bin-by-bin systematic uncertainty from each of these variation. These systematic errors can be seen in Table 4.6.

4.7.3 Other Systematic Uncertainties

There are three systematic uncertainties that come from studies done by others in the GlueX collaboration. The first is a $\pm 5\%$ uncertainty in the luminosity, a value used in the calculation of

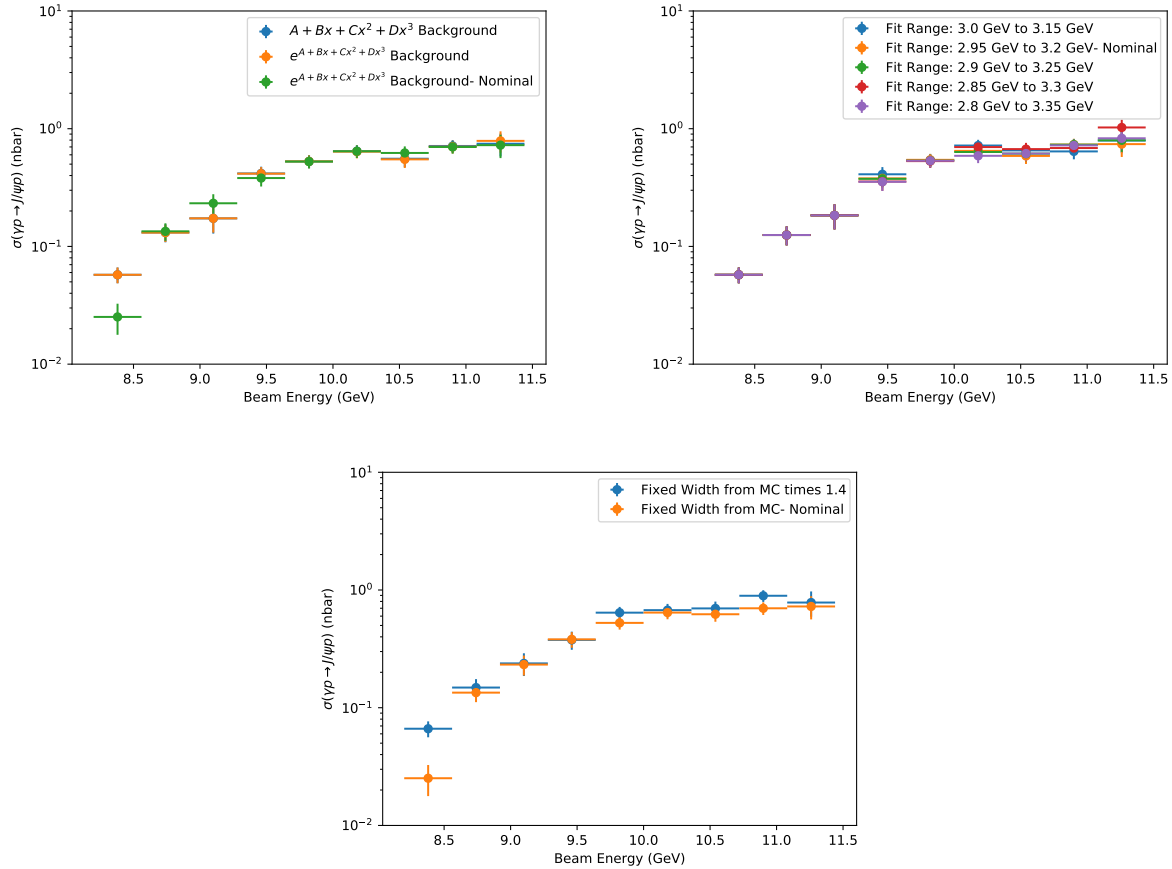


Figure 4.35: (Top left) Total cross section measurement for different background functions. Besides the nominal background function of $e^{A+Bx+Cx^2}$, we use background functions $A + Bx + Cx^2 + Dx^3$ and $e^{A+Bx+Cx^2+Dx^3}$. (Top right) Total cross section measurement for different fit range. Besides the nominal fit range of 2.95 GeV - 3.2 GeV, we vary the fit range from 2.8 GeV - 3.35 GeV to 3.0 GeV - 3.15 GeV in steps of 0.05 GeV. (Bottom) Total cross section measurement for different fixed width. We use a fixed width from Monte Carlo to fit the J/ψ mass distribution for the nominal fits. For the variation, we find a scale factor between data and Monte Carlo of the widths for the full beam energy range. We found the data width was 1.4 times bigger than Monte Carlo. We then use the width from Monte Carlo for each energy bin multiplied by 1.4.

Table 4.6: A list of systematic errors in each energy bin due to yield extraction. Those with "-" had negligible effects on the cross section.

Energy Bin (GeV)	Bkg Function	Fit Range	Fixed Width
8.20 - 8.56	-	-	± 0.009 nb
8.56 - 8.92	± 0.006 nb	-	± 0.023 nb
8.92 - 9.28	± 0.011 nb	-	± 0.054 nb
9.28 - 9.64	± 0.038 nb	± 0.032 nb	± 0.002 nb
9.64 - 10.00	± 0.017 nb	± 0.013 nb	± 0.098 nb
10.00 - 10.36	± 0.010 nb	± 0.071 nb	± 0.026 nb
10.36 - 10.72	± 0.038 nb	± 0.084 nb	± 0.111 nb
10.72 - 11.08	± 0.030 nb	± 0.092 nb	± 0.160 nb
11.08 - 11.44	± 0.049 nb	± 0.285 nb	± 0.043 nb

the cross section. We use the The second is a $\pm 3\%$ uncertainty per track, an estimation of the tracking uncertainty. This is the value determined for the pion, but with the similarities of the muon to the pion, this is a conservative estimate. The last is a $\pm 1\%$ uncertainty due to the loose timing cuts discussed early. Since the timing cuts used for this analysis is the same as the ones used for the e^+e^- analysis, we use the same uncertainty that was determined in that analysis [67]. By adding these in quadrature, we get an overall normalization uncertainty of $\pm 5.92\%$.

4.8 Final Results

Table 4.7: Final total cross section after all event selections, total statistical uncertainty calculated using MINUIT, total systematic uncertainty calculated by adding all systematic uncertainties in quadrature, and total uncertainty by adding statistical and systematic uncertainties in quadrature.

Energy Bin (GeV)	σ (nb)	Stat. Error (nb)	Syst. Error (nb)	Total Error (nb)
8.20 - 8.56	0.057422	0.00877	0.0377	0.0386
8.56 - 8.92	0.124988	0.022831	0.0667	0.0686
8.92 - 9.28	0.183579	0.04407	0.1354	0.1414
9.28 - 9.64	0.378398	0.058717	0.1614	0.1709
9.64 - 10.00	0.54391	0.066502	0.1895	0.1997
10.00 - 10.36	0.648388	0.079301	0.2131	0.2241
10.36 - 10.72	0.587078	0.085313	0.2625	0.2749
10.72 - 11.08	0.733274	0.08725	0.3073	0.3190
11.08 - 11.44	0.739613	0.164476	0.4608	0.4830

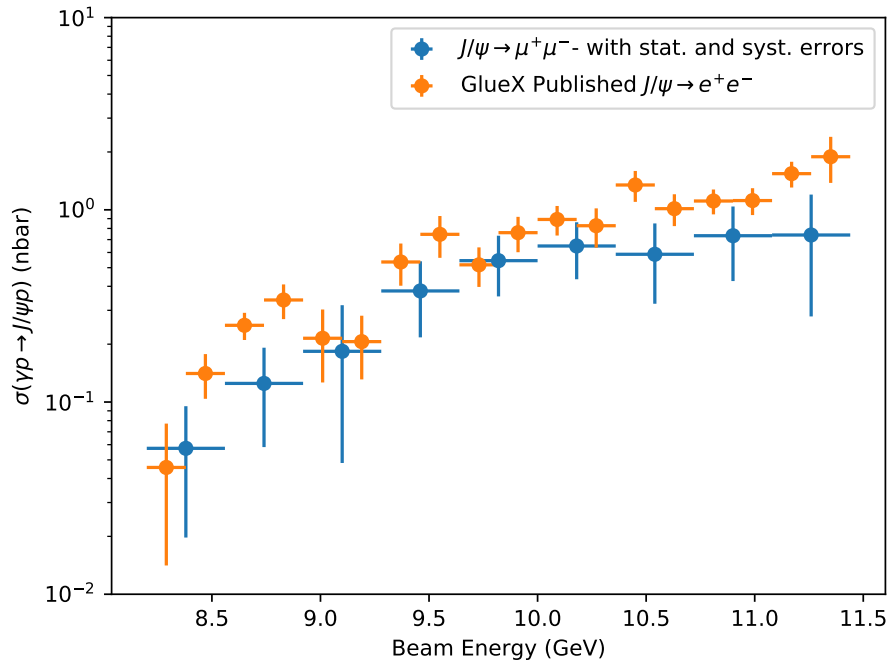


Figure 4.36: The filled blue points show the measured total cross sections obtained from Eq. 4.4 in fine photon energy bins. The error bars represent the statistical errors and systematic errors added in quadrature. The filled orange points represent the GlueX published [34] cross sections from the $J/\psi \rightarrow e^+ e^-$ channel, with the error bars representing the statistical and systematic uncertainties added in quadrature.

After looking at the largest contributions to the systematic uncertainty, we have a final cross section, shown in Figure 4.36, with both systematic and statistical uncertainties added in quadrature. The final cross section and its associated errors are listed in Table ??.

CHAPTER 5

SUMMARY AND CONCLUSION

In summary, this analysis provides a comprehensive measurement of J/ψ photoproduction through the decay channel $J/\psi \rightarrow \mu^+\mu^-$, utilizing the GlueX spectrometer. We report both the total cross section, which includes statistical and systematic uncertainties, and the differential cross section with statistical uncertainties only, for the reaction $\gamma p \rightarrow J/\psi p$. Comparison of these results with the published GlueX measurements, shown in Figure 5.1 demonstrates a general agreement in the shapes of the cross section distributions. We get an average ratio of 0.6 ± 0.52 , which is within 1 with uncertainties. However, we observe that the $J/\psi \rightarrow \mu^+\mu^-$ results tend to be systematically lower than expected. This downward shift is not yet fully understood, but it is noteworthy that the theoretical models are primarily concerned with the shapes of these distributions. Also, there is an overall 20% normalization uncertainty with the $J/\psi \rightarrow e^+e^-$ results, which could be contributing to this systematic difference between the two measurements.

Several key observations can be made from our findings. First, the distinct dip observed in the $J/\psi \rightarrow e^+e^-$ total cross section does not appear in the $J/\psi \rightarrow \mu^+\mu^-$ total cross section. However, due to the relatively large uncertainties in this analysis, we cannot definitively rule out its presence. Second, the $J/\psi \rightarrow \mu^+\mu^-$ differential cross section appears to flatten at low t and high beam energy, a trend that aligns with the $J/\psi \rightarrow e^+e^-$ results. Overall, while the shapes of the distributions align reasonably well, additional work is required to resolve the observed systematic discrepancies.

This work represents the first measurement of muons in the GlueX spectrometer, and further research is needed to fully characterize this new mode of measurement. A preliminary study of the physics triggers used in the GlueX spectrometer has shown that our efficiency is sensitive to the modeling of the trigger thresholds. Since the trigger depends on the total energy deposited in the calorimeters, and considering that our final state includes only three particles—none of which are photons or electrons—the combined energy deposited in the calorimeters is close to the threshold values. This is especially true with events that are triggered by the BCAL only, where all three particles go through the BCAL without depositing in the FCAL. This sensitivity may impact the total cross section measurement, and we hypothesize that it contributes to the downward shift observed. Further investigation is required to better understand and quantify this effect.

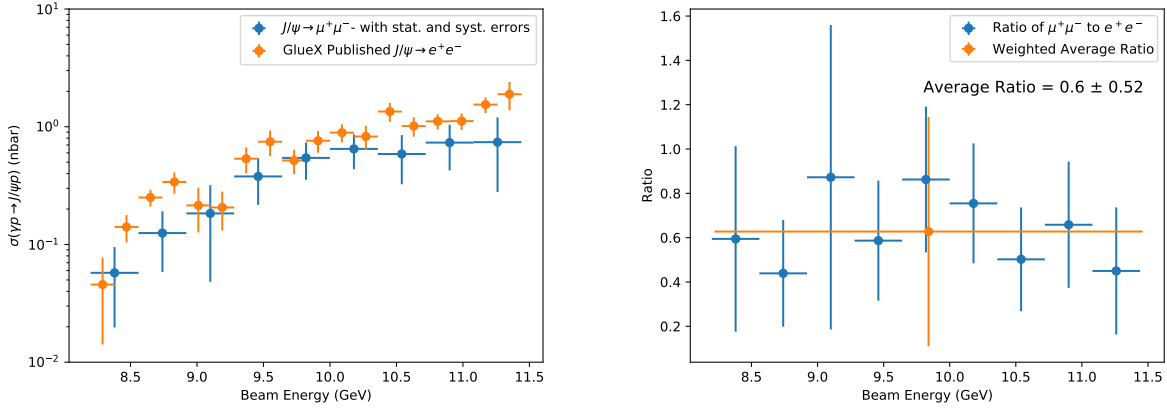


Figure 5.1: (Left) The filled blue points show the measured total cross sections obtained from Eq. 4.4 in fine photon energy bins. The error bars represent the statistical errors and systematic errors added in quadrature. The filled orange points represent the GlueX published [34] cross sections from the $J/\psi \rightarrow e^+e^-$ channel, with the error bars representing the statistical and systematic uncertainties added in quadrature. (Right) A ratio of the measured total cross sections from this analysis and the published $J/\psi \rightarrow e^+e^-$ channel. We get an average ratio of 0.6 ± 0.52 .

Additionally, the systematic uncertainties in this analysis were conservatively estimated, given the novelty of using muon-based measurements in the GlueX spectrometer. To refine our results, additional studies are necessary to better constrain these uncertainties and reduce their impact. Future efforts in this area will aim to achieve a more precise understanding of the systematic effects involved, which could help reduce the uncertainty range and improve the accuracy of this pioneering measurement.

Importantly, GlueX is continuing to collect data and is expected to nearly double the statistics by the end of next year. This substantial increase in data will significantly enhance the statistical precision of our results, enabling more robust conclusions and likely reducing uncertainties in both the total and differential cross sections. With these forthcoming data, we anticipate further insights into the photoproduction dynamics of J/ψ and a deeper understanding of the systematic effects observed in this initial analysis.

APPENDIX A

MASS DISTRIBUTIONS

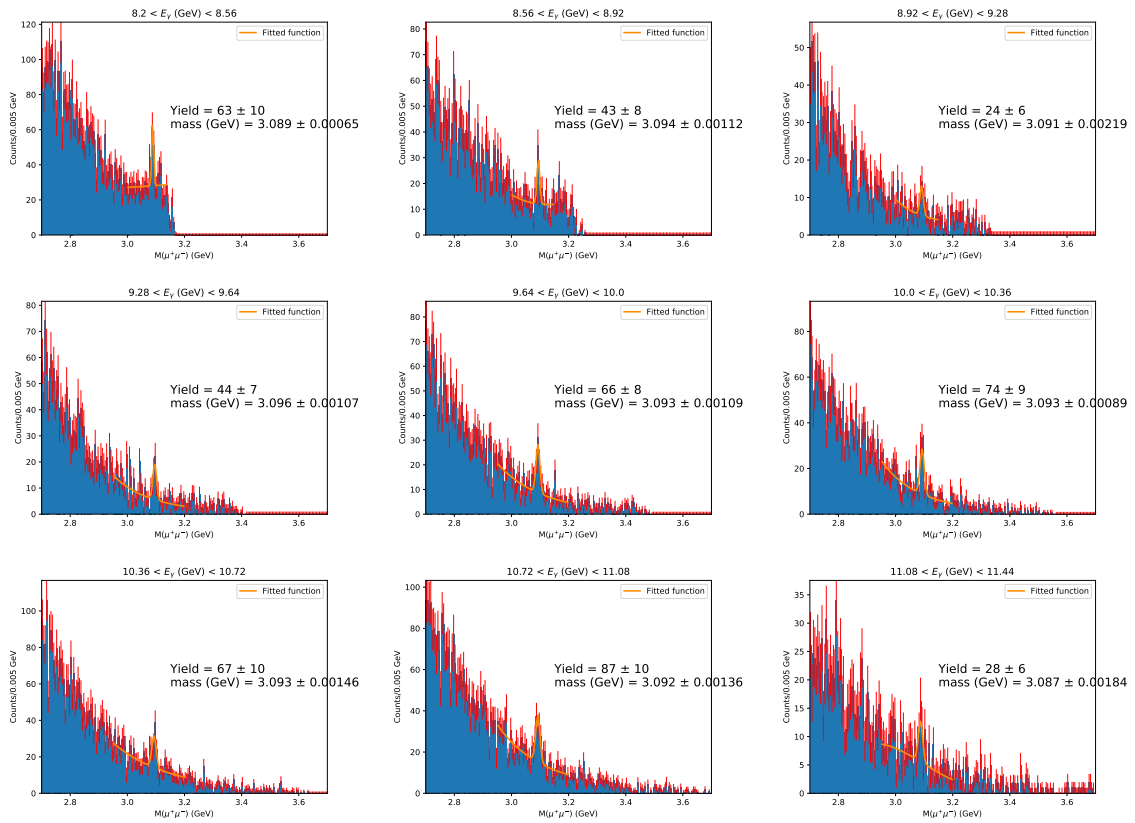


Figure A.1: Mass distributions and fits for final cross section. They are fit with a Gaussian peak and background of the form $e^{A+Bx+Cx^2}$.

REFERENCES

- [1] R. L. Workman *et al.*, “Review of Particle Physics,” *PTEP*, vol. 2022, p. 083C01, 2022.
- [2] C. D. Roberts, “Hadron Physics and QCD: Just the Basic Facts,” *J. Phys. Conf. Ser.*, vol. 630, no. 1, p. 012051, 2015.
- [3] A. Deur, S. J. Brodsky, and G. F. de Teramond, “The QCD Running Coupling,” *Nucl. Phys.*, vol. 90, p. 1, 2016.
- [4] N. Brambilla and A. Vairo, “Quark confinement and the hadron spectrum,” in *13th Annual HUGS AT CEBAF*, pp. 151–220, 5 1999.
- [5] M. Gell-Mann, “A schematic model of baryons and mesons,” *Physics Letters*, vol. 8, no. 3, pp. 214 – 215, 1964.
- [6] G. Zweig, “An SU_3 model for strong interaction symmetry and its breaking,” 1964.
- [7] C. A. Meyer, “Light and exotic mesons,” 2001.
- [8] F. Gross *et al.*, “50 Years of Quantum Chromodynamics,” *Eur. Phys. J. C*, vol. 83, p. 1125, 2023.
- [9] B. Ketzer, B. Grube, and D. Ryabchikov, “Light-Meson Spectroscopy with COMPASS,” *Prog. Part. Nucl. Phys.*, vol. 113, p. 103755, 2020.
- [10] V. Crede and W. Roberts, “Progress towards understanding baryon resonances,” *Reports on Progress in Physics*, vol. 76, p. 076301, June 2013.
- [11] E. Rutherford, “Collision of alpha particles with light atoms. iv. an anomalous effect in nitrogen,” *Philosophical Magazine*, vol. 90, no. sup1, pp. 31–37, 2010.
- [12] J. Chadwick, “Possible existence of a neutron,” *Nature*, vol. 129, no. 3252, pp. 312–312, 1932.
- [13] M. Nowakowski, E. A. Paschos, and J. M. Rodríguez, “All electromagnetic form factors,” *European Journal of Physics*, vol. 26, p. 545–560, Apr. 2005.
- [14] V. D. Burkert, L. Elouadrhiri, F. X. Girod, C. Lorce, P. Schweitzer, and P. E. Shanahan, “Colloquium: Gravitational form factors of the proton,” 2024.
- [15] M. N. Rosenbluth, “High energy elastic scattering of electrons on protons,” *Phys. Rev.*, vol. 79, pp. 615–619, Aug 1950.
- [16] R. W. McAllister and R. Hofstadter, “Elastic scattering of 188-mev electrons from the proton and the alpha particle,” *Phys. Rev.*, vol. 102, pp. 851–856, May 1956.

- [17] W. Xiong *et al.*, “A small proton charge radius from an electron–proton scattering experiment,” *Nature*, vol. 575, no. 7781, pp. 147–150, 2019.
- [18] N. Bezginov, T. Valdez, M. Horbatsch, A. Marsman, A. C. Vutha, and E. A. Hessels, “A measurement of the atomic hydrogen lamb shift and the proton charge radius,” *Science*, vol. 365, no. 6457, pp. 1007–1012, 2019.
- [19] A. Antognini *et al.*, “Proton structure from the measurement of 2s-2p transition frequencies of muonic hydrogen,” *Science*, vol. 339, no. 6118, pp. 417–420, 2013.
- [20] E. Tiesinga, P. J. Mohr, D. B. Newell, and B. N. Taylor, “Codata recommended values of the fundamental physical constants: 2018,” *Rev. Mod. Phys.*, vol. 93, p. 025010, Jun 2021.
- [21] C. Lorcé, P. Schweitzer, and K. Tezgin, “2d energy-momentum tensor distributions of nucleon in a large-quark model from ultrarelativistic to nonrelativistic limit,” *Physical Review D*, vol. 106, July 2022.
- [22] J. C. Collins and A. Freund, “Proof of factorization for deeply virtual compton scattering in qcd,” *Physical Review D*, vol. 59, Feb. 1999.
- [23] C. Alexandrou, S. Bacchio, M. Constantinou, J. Finkenrath, K. Hadjiyiannakou, K. Jansen, G. Koutsou, H. Panagopoulos, and G. Spanoudes, “Complete flavor decomposition of the spin and momentum fraction of the proton using lattice qcd simulations at physical pion mass,” *Physical Review D*, vol. 101, May 2020.
- [24] D. C. Hackett, D. A. Pefkou, and P. E. Shanahan, “Gravitational form factors of the proton from lattice qcd,” *Physical Review Letters*, vol. 132, June 2024.
- [25] C. Alexandrou, K. Cichy, M. Constantinou, K. Hadjiyiannakou, K. Jansen, A. Scapellato, and F. Steffens, “Unpolarized and helicity generalized parton distributions of the proton within lattice qcd,” *Physical Review Letters*, vol. 125, Dec. 2020.
- [26] T. S. H. Lee, S. Sakinah, and Y. Oh, “Models of J/Ψ photo-production reactions on the nucleon,” *Eur. Phys. J. A*, vol. 58, no. 12, p. 252, 2022.
- [27] J. C. Collins, L. Frankfurt, and M. Strikman, “Factorization for hard exclusive electroproduction of mesons in qcd,” *Physical Review D*, vol. 56, p. 2982–3006, Sept. 1997.
- [28] D. Kharzeev, H. Satz, A. Syamtomov, and G. Zinovev, “ J/ψ photoproduction and the gluon structure of the nucleon,” *Nucl. Phys. A*, vol. 661, pp. 568–572, 1999.
- [29] S. J. Brodsky, E. Chudakov, P. Hoyer, and J. M. Laget, “Photoproduction of charm near threshold,” *Phys. Lett. B*, vol. 498, pp. 23–28, 2001.
- [30] U. Camerini, J. G. Learned, R. Prepost, C. M. Spencer, D. E. Wisner, W. W. Ash, R. L. Anderson, D. M. Ritson, D. J. Sherden, and C. K. Sinclair, “Photoproduction of the ψ particles,” *Phys. Rev. Lett.*, vol. 35, pp. 483–486, Aug 1975.

- [31] B. Gittelman, K. M. Hanson, D. Larson, E. Loh, A. Silverman, and G. Theodosiou, “Photoproduction of the $\psi(3100)$ meson at 11 gev,” *Phys. Rev. Lett.*, vol. 35, pp. 1616–1619, Dec 1975.
- [32] D. E. Kharzeev, “Mass radius of the proton,” *Phys. Rev. D*, vol. 104, no. 5, p. 054015, 2021.
- [33] A. Ali *et al.*, “First measurement of near-threshold j/ψ exclusive photoproduction off the proton,” *Phys. Rev. Lett.*, vol. 123, p. 072001, Aug 2019.
- [34] S. Adhikari *et al.*, “Measurement of the J/ψ photoproduction cross section over the full near-threshold kinematic region,” *Phys. Rev. C*, vol. 108, no. 2, p. 025201, 2023.
- [35] R. P. Feynman, “Photon-hadron interactions,” 1973.
- [36] L. Pentchev and E. Chudakov, ““Rosenbluth” separation of the J/ψ near-threshold photoproduction – an access to the gluon Gravitational Form Factors at high t ,” 4 2024.
- [37] Y. Guo, X. Ji, and F. Yuan, “Proton’s gluon GPDs at large skewness and gravitational form factors from near threshold heavy quarkonium photoproduction,” *Phys. Rev. D*, vol. 109, no. 1, p. 014014, 2024.
- [38] Y. Guo, X. Ji, and Y. Liu, “Qcd analysis of near-threshold photon-proton production of heavy quarkonium,” *Physical Review D*, vol. 103, May 2021.
- [39] P. Sun, X.-B. Tong, and F. Yuan, “Perturbative QCD analysis of near threshold heavy quarkonium photoproduction at large momentum transfer,” *Phys. Lett. B*, vol. 822, p. 136655, 2021.
- [40] M.-L. Du, V. Baru, F.-K. Guo, C. Hanhart, U.-G. Meißner, A. Nefediev, and I. Strakovsky, “Deciphering the mechanism of near-threshold j/ψ photoproduction,” *The European Physical Journal C*, vol. 80, nov 2020.
- [41] R. Aaij *et al.*, “Observation of $j/\psi p$ resonances consistent with pentaquark states in $\Lambda_b^0 \rightarrow j/\psi K^- p$ decays,” *Phys. Rev. Lett.*, vol. 115, p. 072001, Aug 2015.
- [42] R. Aaij *et al.*, “Model-independent evidence for $j/\psi p$ contributions to $\Lambda_b^0 \rightarrow j/\psi p K^-$ decays,” *Phys. Rev. Lett.*, vol. 117, p. 082002, Aug 2016.
- [43] R. Aaij *et al.*, “Observation of a narrow pentaquark state, $P_c(4312)^+$, and of the two-peak structure of the $P_c(4450)^+$,” *Phys. Rev. Lett.*, vol. 122, p. 222001, Jun 2019.
- [44] B. Duran *et al.*, “When Color meets Gravity; Near-Threshold Exclusive J/ψ Photoproduction on the Proton,” 7 2022.
- [45] D. Winney *et al.*, “Dynamics in near-threshold J/ψ photoproduction,” *Phys. Rev. D*, vol. 108, no. 5, p. 054018, 2023.

- [46] Q. Wang, X.-H. Liu, and Q. Zhao, “Photoproduction of hidden charm pentaquark states $P_c^+(4380)$ and $P_c^+(4450)$,” *Phys. Rev. D*, vol. 92, p. 034022, Aug 2015.
- [47] V. Kubarovsky and M. B. Voloshin, “Formation of hidden-charm pentaquarks in photon-nucleon collisions,” *Phys. Rev. D*, vol. 92, p. 031502, Aug 2015.
- [48] M. Karliner and J. L. Rosner, “Photoproduction of exotic baryon resonances,” *Physics Letters B*, vol. 752, pp. 329–332, 2016.
- [49] A. N. H. Blin, C. Fernández-Ramírez, A. Jackura, V. Mathieu, V. I. Mokeev, A. Pilloni, and A. P. Szczepaniak, “Studying the $P_c(4450)$ resonance in j/ψ photoproduction off protons,” *Phys. Rev. D*, vol. 94, p. 034002, Aug 2016.
- [50] I. Strakovsky, W. J. Briscoe, E. Chudakov, I. Larin, L. Pentchev, A. Schmidt, and R. L. Workman, “Plausibility of the LHCb $P_c(4312)^+$ in the GlueX $\gamma p \rightarrow J/\psi p$ total cross sections,” *Phys. Rev. C*, vol. 108, no. 1, p. 015202, 2023.
- [51] S. Adhikari *et al.*, “The GLUEX beamline and detector,” *Nucl. Instrum. Meth. A*, vol. 987, p. 164807, 2021.
- [52] A. N. H. Blin, C. Fernández-Ramírez, A. Jackura, V. Mathieu, V. I. Mokeev, A. Pilloni, and A. P. Szczepaniak, “Studying the $P_c(4450)$ resonance in j/ψ photoproduction off protons,” *Phys. Rev. D*, vol. 94, p. 034002, Aug 2016.
- [53] P. Shanahan and W. Detmold, “Gluon gravitational form factors of the nucleon and the pion from lattice qcd,” *Physical Review D*, vol. 99, Jan. 2019.
- [54] K. A. Mamo and I. Zahed, “Diffractive photoproduction of J/ψ and Υ using holographic QCD: gravitational form factors and GPD of gluons in the proton,” *Phys. Rev. D*, vol. 101, no. 8, p. 086003, 2020.
- [55] Y. Hatta, A. Rajan, and D.-L. Yang, “Near threshold J/ψ and Υ photoproduction at JLab and RHIC,” *Phys. Rev. D*, vol. 100, no. 1, p. 014032, 2019.
- [56] M. Dugger, B. Ritchie, N. Sparks, K. Moriya, R. Tucker, R. Lee, B. Thorpe, T. Hodges, F. Barbosa, N. Sandoval, and R. Jones, “Design and construction of a high-energy photon polarimeter,” *Nuclear Instruments and Methods in Physics Research Section A: Accelerators, Spectrometers, Detectors and Associated Equipment*, vol. 867, pp. 115–127, 2017.
- [57] F. Barbosa, C. Hutton, A. Sitnikov, A. Somov, S. Somov, and I. Tolstukhin, “Pair spectrometer hodoscope for hall d at jefferson lab,” *Nuclear Instruments and Methods in Physics Research Section A: Accelerators, Spectrometers, Detectors and Associated Equipment*, vol. 795, pp. 376–380, 2015.

- [58] N. Jarvis, C. Meyer, B. Zihlmann, M. Staib, A. Austregesilo, F. Barbosa, C. Dickover, V. Razmyslovich, S. Taylor, Y. Van Haarlem, G. Visser, and T. Whitlatch, “The central drift chamber for gluex,” *Nuclear Instruments and Methods in Physics Research Section A: Accelerators, Spectrometers, Detectors and Associated Equipment*, vol. 962, p. 163727, May 2020.
- [59] T. Beattie *et al.*, “Construction and performance of the barrel electromagnetic calorimeter for the GlueX experiment,” *Nuclear Instruments and Methods in Physics Research Section A: Accelerators, Spectrometers, Detectors and Associated Equipment*, vol. 896, pp. 24–42, jul 2018.
- [60] R. Barsotti and M. R. Shepherd, “Using machine learning to separate hadronic and electromagnetic interactions in the GlueX forward calorimeter,” *JINST*, vol. 15, no. 05, p. P05021, 2020.
- [61] E. Pooser, F. Barbosa, W. Boeglin, C. Hutton, M. Ito, M. Kamel, P. Khetarpal, A. LLodra, N. Sandoval, S. Taylor, T. Whitlatch, S. Worthington, C. Yero, and B. Zihlmann, “The GlueX start counter detector,” *Nuclear Instruments and Methods in Physics Research Section A: Accelerators, Spectrometers, Detectors and Associated Equipment*, vol. 927, pp. 330–342, may 2019.
- [62] A. Ali, F. Barbosa, J. Bessuille, E. Chudakov, R. Dzhygadlo, C. Fanelli, J. Frye, J. Hardin, A. Hurley, G. Kalicy, J. Kelsey, W. Li, M. Patsyuk, C. Schwarz, J. Schwiening, M. Shepherd, J. Stevens, T. Whitlatch, M. Williams, and Y. Yang, “The GLUEX DIRC program,” *Journal of Instrumentation*, vol. 15, pp. C04054–C04054, apr 2020.
- [63] A. Ali, F. Barbosa, J. Bessuille, E. Chudakov, R. Dzhygadlo, C. Fanelli, J. Frye, J. Hardin, A. Hurley, E. Ihloff, G. Kalicy, J. Kelsey, W. B. Li, M. Patsyuk, J. Schwiening, M. Shepherd, J. R. Stevens, T. Whitlatch, M. Williams, and Y. Yang, “Initial performance of the GlueX DIRC detector,” *Journal of Physics: Conference Series*, vol. 2374, p. 012009, nov 2022.
- [64] I. Adam *et al.*, “The dirc particle identification system for the babar experiment,” *Nuclear Instruments and Methods in Physics Research Section A: Accelerators, Spectrometers, Detectors and Associated Equipment*, vol. 538, no. 1, pp. 281–357, 2005.
- [65] T. Beattie *et al.*, “Construction and performance of the barrel electromagnetic calorimeter for the gluex experiment,” *Nuclear Instruments and Methods in Physics Research Section A: Accelerators, Spectrometers, Detectors and Associated Equipment*, vol. 896, pp. 24–42, 2018.
- [66] R. Barlow, “Systematic errors: facts and fictions,” 2002.
- [67] S. Adhikari *et al.*, “The GLUEX beamline and detector,” *Nucl. Instrum. Meth. A*, vol. 987, p. 164807, 2021.

BIOGRAPHICAL SKETCH

Donavan Ebersole is a native of northern Florida, graduating from Blountstown High School in 2015. He began his studies at Chipola College, then transferred to Troy University, where he graduated with a dual bachelor's degrees in mathematics and physics. Donovan began his PhD at Florida State University in Tallahassee, FL in 2019, where he studied under the tutelage of Dr. Sean Dobbs. Donovan's area of expertise is in particle physics with a focus on hadronic spectroscopy. Donovan's specific area of interest is the decay of the J/ψ particle into a $\mu^+\mu^-$ pair through photoproduction. His work requires analyzing data taken at the GlueX experiment located at Jefferson Labs in Newport News, Virginia. During his graduate studies, Donovan and his wife, Madelynn, became parents to Huxley Ebersole, and they will be welcoming another son in 2025. Upon graduation, Donovan will be a tenured-track professor in the Physical Sciences Department at Snead State Community College in Boaz, AL.